UNIVERSITY OF BERGEN

MASTER THESIS

Aircraft interaction with electric field of thundercloud and observations of hard radiation

Author:
Chris Alexander Skeie

Supervisors:
Nikolai Østgaard
Pavlo Kochkin

A thesis submitted in fulfilment of the requirements for the degree of Master of Science - Space Physics

at the

Birkeland Centre for Space Science

June 1, 2018

UNIVERSITY OF BERGEN

"Thunder is good, thunder is impressive; but it is lightning that does the work."

Mark Twain

UNIVERSITY OF BERGEN

Abstract

Institutt for Fysikk og Teknologi
Birkeland Centre for Space Science

Master of Science - Space Physics

Aircraft interaction with electric field of thundercloud and observations of hard radiation

by Chris Alexander Skeie

The purpose of this thesis is to study the relationship between the different phases of lightning flashes and the production of high-energy emissions, as well as high-energy emissions observed from thunderclouds. The data consists of local electric field-, current- and energy measurements on board an aircraft.

The lightning attachment points on the aircraft, were identified by the local electric field signatures of the positive and negative leader initiations. Showing a preference of attachment points based on aircraft model and/or flight altitude.

Four distinct radiation producing events were identified by the electric fields and x-ray counts measured during the flights.

Single photons in association with the stepping of negative leaders, with photon energies close to 100 keV. A correlation between the changes in local electric field, current and the energy of the observed photons were investigated, but were not found.

Bursts of photons in association with recoils were observed. Recoils are microsecond fast changes in the local electric field, observed during the return strokes, dart leaders and recoil streamers of a lightning flash. The energies of the observed photon bursts are similar to that of the single photons observed during negative leader steps.

Minute long gamma-ray glows from the data set has previously been reported. The findings were used as a basis to search for more gamma-ray glows in the dataset, and a total of 7 new low intensity gamma-ray glow candidates were found. A statistical analysis of the count rates were done for all observed gamma-ray glows to compare the events.

Millisecond long x-ray count rate enhancements were observed on 14.01.2016. The lightning flashes were analysed by examining x-ray count rates and local electric fields. The energy spectrum of some of the observed flashes revealed an enhancement at 511 keV, which is the signature energy for positron annihilation. Two previously observed events were compared to two new findings, showing a very good correlation.

Acknowledgements

I would like to extend my thanks and gratitude to my supervisors Prof. Dr. Nikolai Østgaard and Dr. Pavlo Kochkin for their support and guidance during these two years.

I would also like to thank the team and contributors of the ILDAS project for the data used in this thesis.

A special thanks to my current fellow master student Anders, Hogne, Mats and Ragnar and former master students Astrid, Bjørn, Kristian, Nini and Roger for many helpful discussions and good times.

Finally, I would like to thank my friends and family for their support during these two years. And a special thanks to Heidi Moss and Mats Heigre for the help with proofreading this thesis.

And last, but not least, a huge thank you to my better half Charlotte, for all the support and understanding shown during these two years.

Contents

List of Abbreviations

ADELE	**A**irborne **D**etector for **E**nergetic **L**ightning **E**missions
CDF	**C**ontinuous **D**ata **F**iles
CA	**C**loud to **A**ir
CC	**C**loud to **C**loud
CG	**C**loud to **G**round
GPATS	**G**lobal **P**osition and **T**racking **S**ystems
GLM	**G**eostationary **L**ightning **M**apper
IC	**I**nter or Intra Cloud
ILDAS	**I**n-flight **L**ightning **D**amage **A**ssesment **S**ystem
LIAS	**L**ightning **I**ncident **A**rchive **S**earch
NLR	Dutch **N**ational Aerospace **L**abo**r**atory
REA	**R**unaway **E**lectron **A**valanche
RREA	**R**elativistic **R**unaway **E**lectron **A**valanche
WWLLN	**W**orld **W**ide **L**ightning **L**ocation **N**etwork

Physical Constants

Electric field needed for positive streamer propagation	$E_{cr}^{+} = \sim 5$ kV/m
Electric field needed for positive streamer propagation	$E_{cr}^{-} = \sim 10$ kV/m
Electric field needed for conventional breakdown	$E_k = \sim 32$ kV/m
Electric field needed for thermal runaway	$E_c = \sim 260$ kV/m
Electric field needed to create a relativistic runaway electron	$E_t = \sim 2$kV/m
Mass of electron	$\mathrm{m}_e = 9.10938 \cdot 10^{-31}$ kg
Permeability of vacuum	$\mu_0 = 1.257 \cdot 10^{-6}$ H/m
Permittivity of free space	$\epsilon_0 = 8.85 \cdot 10^{-12}\ C^2 \cdot N^2/m^2$
Planck constant	$\mathrm{h} = \sim 4.136 \cdot 10^{-16}$ eV $\cdot$ s

List of Symbols

a	Aircraft radius	m
E	Electric field	kV/m
E_K	Kinetic energy	J
f	frequency	Hz
F_D	Friction force	eV/cm
H_0	Magnetic field	$\mathrm{A\,m^{-1}}$
I	Current	A
p	momentum	$\mathrm{kg \cdot m/s}$
Q	Charge	C
$S(E)$	Linear stopping power	MeV/mm
t	Time	s
V	Voltage	V
λ	Wavelength	nm
μ	Linear attenuation coefficient	$\mathrm{cm^{-1}}$
ϕ	Ionisation potential	kJ/mol
ρ	Density	$\mathrm{g/cm^3}$

Chapter 1

Introduction

Lighting and the electric field of thunderclouds are associated with high-energy radiation in many ways. Wilson [1924] was the first to link the electric fields of thunderclouds to the production of radiation. Since then, many radiation producing events have been found and linked to the acceleration of particles in the strong electric fields of thunderclouds.

It was believed for a long time that lightning itself did not involve any high-energy processes which could produce energetic radiation. This changed in 2001, when Moore et al. [2001] showed that natural lightning could produce energetic radiation.

Since then, lightning has been shown to generate nanosecond bursts of x-rays in meter-long laboratory discharges [Dwyer et al., 2005b; Kochkin et al., 2012; Kochkin et al., 2015b; Østgaard et al., 2016]. The bursts are suggested to be generated by the electric fields of streamer encounters [Kochkin et al., 2015b]. X-rays associated with the stepping process of negative leaders were first reported by Dwyer et al. [2005a], who also confirmed that the stepped leader is the source of the energetic radiation, and that the large pulses observed were not high energy gamma rays, but bursts of x-rays with energies typically below 150 keV. Dwyer et al. [2005a] collected data from five negative cloud-to-ground lightning flashes over Florida. Figure 1.1 show the correlation of x-ray pulses and electric field measured by Dwyer et al. [2005a]. A 0.25 V pulse in the signal corresponds to 662 keV deposited energy.

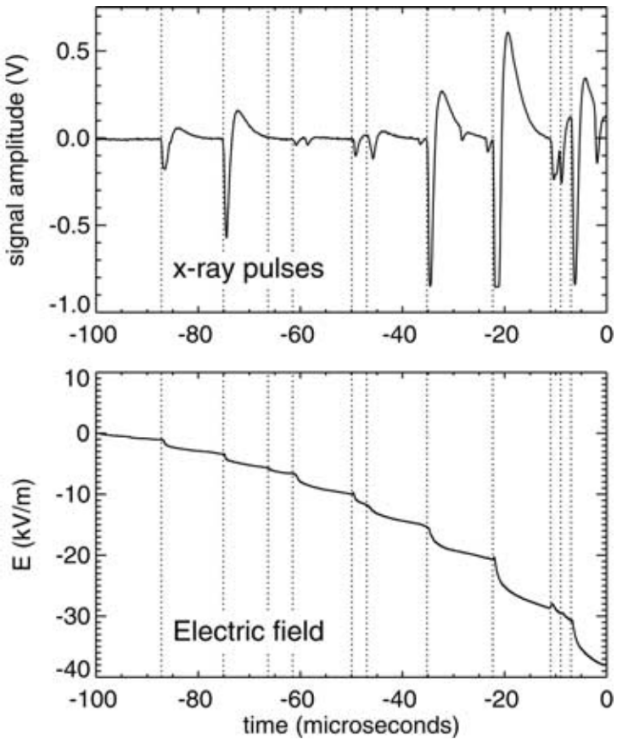

FIGURE 1.1: Top graph shows the measured x-ray pulses which correlate temporally with the observed steps in the electric fields of the bottom graph. Figure from [Dwyer et al., 2005a].

Microsecond long bursts of x-ray and gamma radiation have been observed from both triggered and natural lightning, with energy spectra ranging up to a few hundred keV [Moore et al., 2001; Dwyer et al., 2004; Dwyer, 2004; Dwyer et al., 2005a; Howard et al., 2010]. Dwyer et al. [2004] measured x-ray emissions from dart leaders in rocket-triggered lightning. The radiation observed was measured during the dart leader phase and at the onset of the return stroke of the triggered lightning. The observed energy spectrum of the x-rays extended up to $\sim$ 250 keV, with typical values well below this value. The emission consists of bursts of photons, rather than a continuous emission and was measured to usually last less than $1\mu s$ [Dwyer et al., 2004; Dwyer, 2004].

X-rays are also observed without associated lightning flashes. One example are gamma-ray glows. A gamma-ray glow is a second to minutes long x-ray and gamma emission from thunderclouds. It is most likely generated by charged particles being accelerated in the high electric field region inside the thunderclouds, and can last from seconds to several minutes. The first airborne observations of glows were done by Parks et al. [1981] during the Storm Hazards Program. McCarthry and Parks [1985] were also the first to report the termination of a glow by a lightning flash.

In recent times, the Airborne Detector for Energetic Lightning Emissions (ADELE) recorded 12 gamma ray glows, which lasted from 4 to 112 seconds, while flying over Colorado and Florida. The duration of the glows are most likely due to the aircraft's motion, and should not be counted as an intrinsic attribute of the glows [Kelly et al., 2015]. Some differences in the shape of the count rates has been identified, like the double peaks observed in count rates by Parks et al. [1981] and Kelly et al. [2015],

or the reported sudden terminations caused by lightning flashes [McCarthry and Parks, 1985; Kochkin et al., 2017].

Kochkin et al. [2017] reports observing a gamma-ray glow from an aircraft at 12 km altitude over northern Australia. They observe a distant lightning discharge terminating the glow, simultaneously triggering a discharge from the aircraft. About six minutes later, they observe another glow, that appears to be a double peaked. The two glows observed by Kochkin et al. [2017] are shown in figures 1.2 and 1.3.

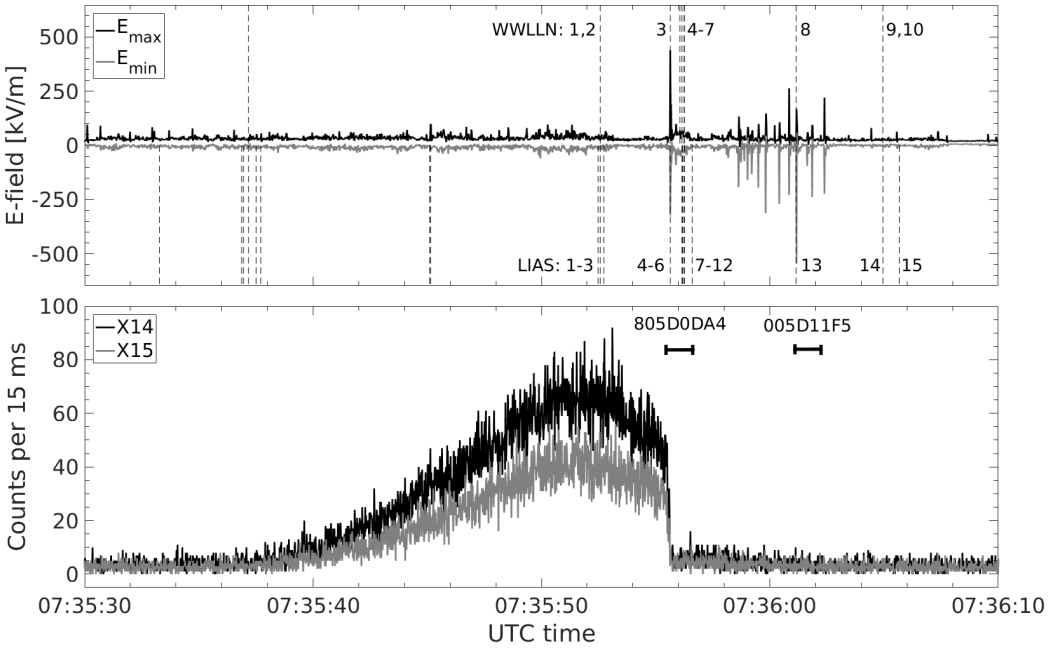

FIGURE 1.2: The top graph shows the local electric field minimum and maximum in 18 ms bins. The dotted lines represent lightning discharges registered by two different lightning location networks. The bottom graph shows the total x-ray counts in 15 ms bins. The glow lasts for $\sim$ 20 seconds, before it gets terminated by a lightning flash. Image from [Kochkin et al., 2017].

Figure 1.2 shows an intense glow observed during the aircraft campaign. This gamma-ray glow is terminated by a lighting flash at about 07:35:56. Figure 1.3 shows a less intense glow observed the same day. Two peaks in count rate can be seen during the glow.

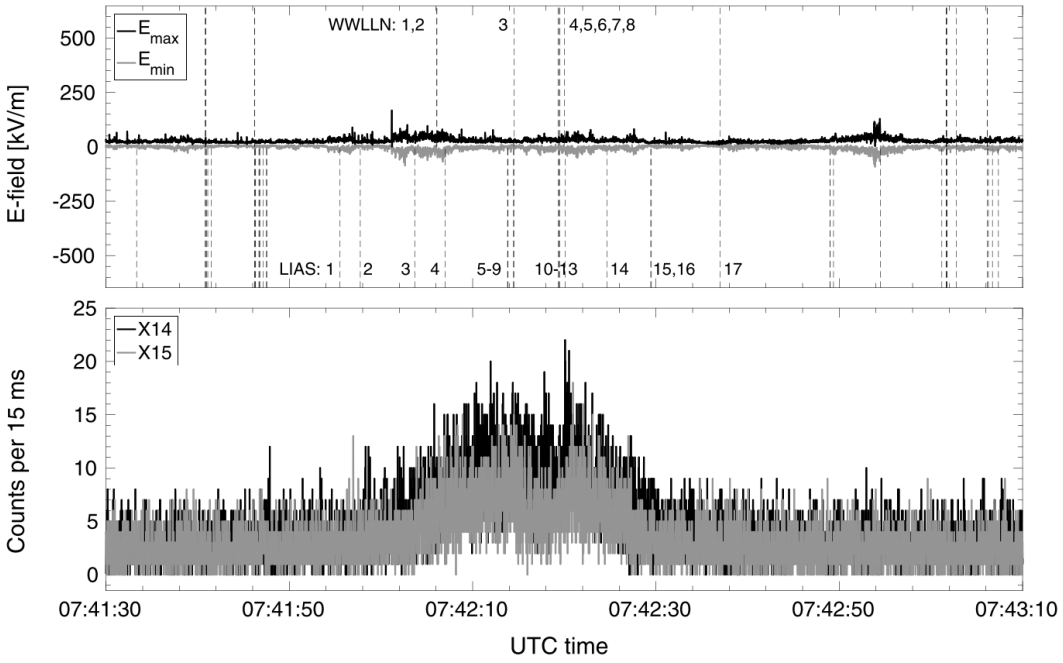

FIGURE 1.3: The top graph shows the local electric field minimum and maximum in 18 ms bins. The dotted lines represent lightning discharges registered by two different lightning location networks. The bottom graph shows the total x-ray counts in 15 ms bins. The glow lasts for $\sim$ 30 seconds and was not terminated early, like the glow in figure 1.2. Image from [Kochkin et al., 2017].

X-ray energies corresponding to positron annihilation have also recently been observed during two separate aircraft campaigns [Dwyer et al., 2015; Kochkin et al., Under review]. Both campaigns found that the energy enhancements were accompanied by electrical activity close to the aircraft. The energy enhancements were found to be associated with negative static discharges from the aircraft [Kochkin et al., Under review]. The author of this thesis is one of the co-authors of [Kochkin et al., Under review].

This thesis will use data gathered from an aircraft, flying into thunderstorms to answer the following question: When during a lighting flash do we observe x-rays, and is the production of x-rays related to changes in the current or local electric fields measured on the aircraft? Are x-rays observed without associated aircraft-initiated lightning flashes?

Chapter 2

Theory

This chapter will present the theoretical background needed for this thesis.

2.1 Thunderclouds

The main source of lightning flashes is the lightning-producing Cumulonimbus cloud type, also called a thundercloud. Lightning-like discharges can also be generated in environments with fine grained particles, such as sandstorms or the ejected materials over volcanoes [Rakov and Uman, 2003]. This section will describe the general charge distribution of thunderclouds, their electrification and the different types of lightning discharges.

2.1.1 Charge distribution in thunderclouds

The motion and distribution of electric charges in thunderclouds are complicated and continuously change with time. Most of the electric charges reside on hydrometeors (see chapter 2.1.2). The charge structure of a thundercloud is often approximated by three vertically stacked charges located over a perfectly conducting ground (see figure 2.1.). This tripole consists of a positive charge near the top of the cloud often referred to as the upper positive, a negative charge of the same magnitude below it referred to as the main negative, and a much smaller positive charge at the bottom referred to as the lower positive [Rakov and Uman, 2003].

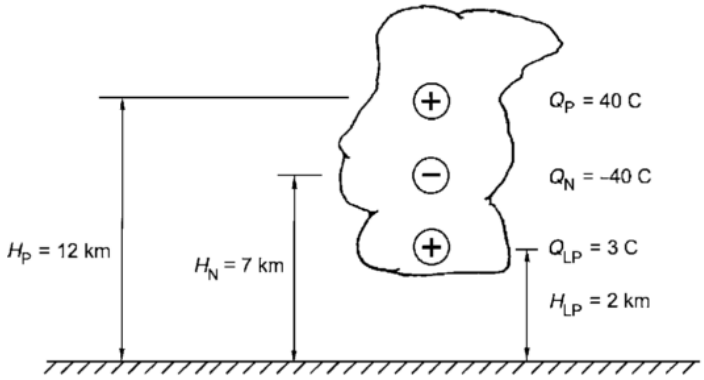

FIGURE 2.1: Illustration of vertically stacked tripole, representing a simple model of the gross charge structure of a thundercloud. At the top is the Upper Positive charge (UP), in the middle is the Main Negative charge (MN) and at the bottom is the Lower Positive charge (LP). Figure from [Rakov and Uman, 2003].

The values given in figure 2.1 are typical values for charge sizes and heights of charge centres found in thunderclouds [Rakov and Uman, 2003].

Method of images

The method of images is a method used to calculate the electric fields observed from point charges. This is done by mirroring three charges of opposite polarity through the conducting surface, and then use the principle of superposition. Figure 2.2 shows the components of the electric field, from calculations with a mirror image point charge and the principle of superposition. The image charge will then compensate for the conducting ground.

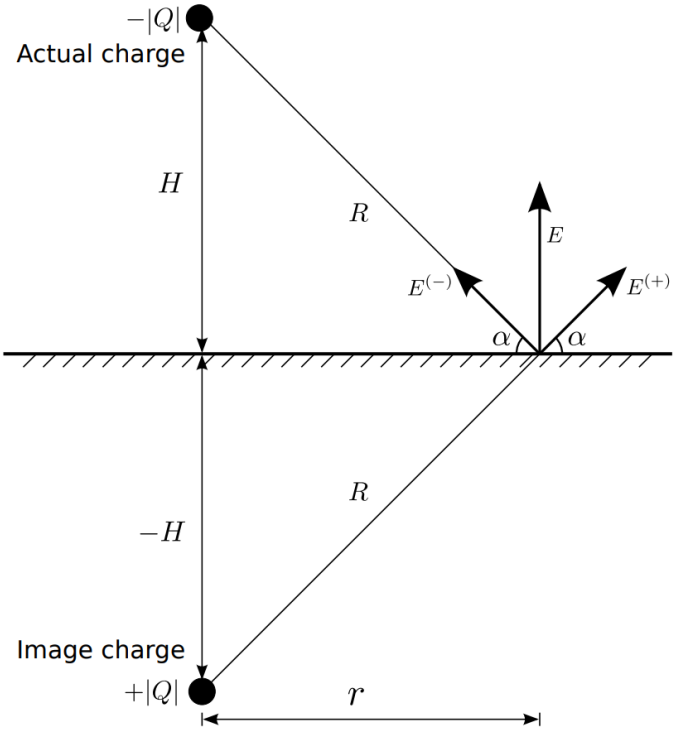

FIGURE 2.2: Illustration of the components of the electric field of a thundercloud, as observed from the ground. The electric field calculations are done using a mirror image of a point charge and the principle of superposition. Here H refers to the altitude of the point charge, r is the horizontal distance between the vertical centre of the charge and the observer, R is $\sqrt{H^2 + r^2}$ and α is the angle between the horizontal line and the radial electric field vectors. Figure from [Rakov and Uman, 2003].

The total electric field will be given as a sum of the contributions from real and mirror charges. The electric field components seen in figure 2.2 are given as:

$$|E^-| = |E^+| = \frac{|Q|}{4\pi\epsilon_0(H^2 + r^2)} \tag{2.1}$$

where $|Q|$ is the charge magnitude and ϵ_0 is the permittivity of free space. The total electric field in the vertical direction is then given as:

$$|E| = 2|E^-|cos(90\,\text{deg} - \alpha) = 2|E^+|cos(90\,\text{deg} - \alpha) \tag{2.2}$$
$$= 2|E^-|sin\alpha \tag{2.3}$$
$$= \frac{|Q|H}{2\pi\epsilon_0(H^2 + r^2)^{3/2}} \tag{2.4}$$
$$= k\frac{sin\alpha}{R^2}, \quad k = \frac{|Q|}{2\pi\epsilon_0}, \quad R^2 = (H^2 + r^2) \tag{2.5}$$

The total electric field from the three stacked charges in figure 2.1 can then be calculated as the sum of the contributions. Figure 2.3 shows the resulting electric field.

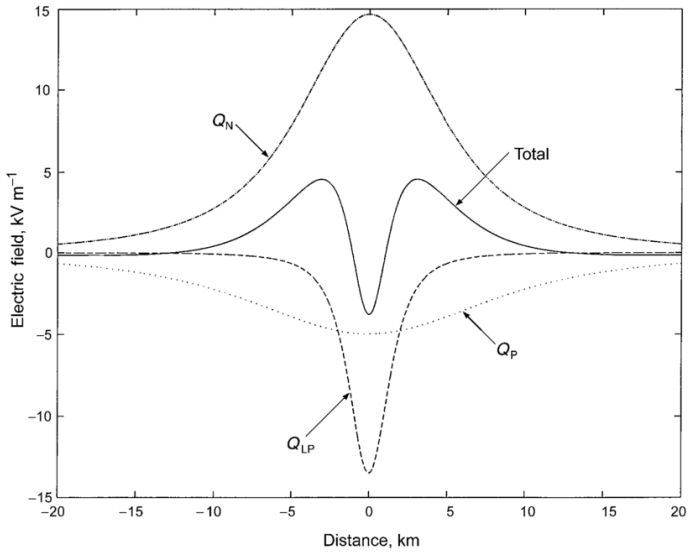

FIGURE 2.3: Electric field of the tripole model, as a function of distance from the tripole. The Total is the sum of all fields, Q_N is the contribution from the negative charge centre, Q_P is the main positive charge centre contribution, and Q_{LP} the contribution of the lower positive charge. Here, an upward electric field is defined as positive. Figure from [Rakov and Uman, 2003].

As seen, the electric field is negative close to and underneath the charge centres. This is caused by the lower positive charge Q_{LP}. As the distance increases, it first turns positive due to the contributions of the main negative charge Q_N, before it slowly decreases back to a negative value again due to the main positive charge.

2.1.2 Charge separation in thunderclouds

There are several mechanisms of cloud electrification proposed over the years. The two most commonly discussed are the Graupel-Ice mechanism and the Convection mechanism. Common to both are a small scale processes that electrifies individual hydrometeors and spatially separate them by polarity.

Hydrometeors are small particles made of ice and/or water droplets. Hydrometeors that fall with a speed equal to or over 0.3 m/s are called precipitation particles, while all other hydrometeors are called cloud particles. Precipitating particles are thought to be generally larger than cloud particles, but there are no defined rules

for determining particle type by size. The hydrometeors are also considered to have very low mobility, which reduces the current leakage between charge centres in the clouds, effectively turning the clouds into good insulators [Rakov and Uman, 2003].

The Graupel-Ice mechanism

The Graupel-Ice mechanism is not dependant on any external sources for electrification. Instead the electrification occurs via collision between Graupels and cloud particles. A Graupel is a type of precipitating particle that forms when snow crystals come in contact with supercooled water droplets. The supercooled water droplet will immediately freeze on the the surface of the snow crystal, making it grow in size [BARC, 2016].

The falling Grauepls attain charge when they collide with ice crystals and water droplets that rise in the updrafts (up to 10 m/s) of the cloud. The temperature of the air decides if the Graupel will gain negative or positive charge. The falling graupels will leave behind positive charge in the upper regions of the cloud, creating the upper positive charge. When the air temperature falls bellow a certain temperature, called the reversal temperature ($-10\,^{\circ}$C to $-20\,^{\circ}$C), the Graupels will leave negative charge, and create the main negative charge. For temperatures over this limit they will again leave positive charge, and create the lower positive charge [Jayaratne and Saunders, 1983; Rakov and Uman, 2003]. This is illustrated in figure 2.4.

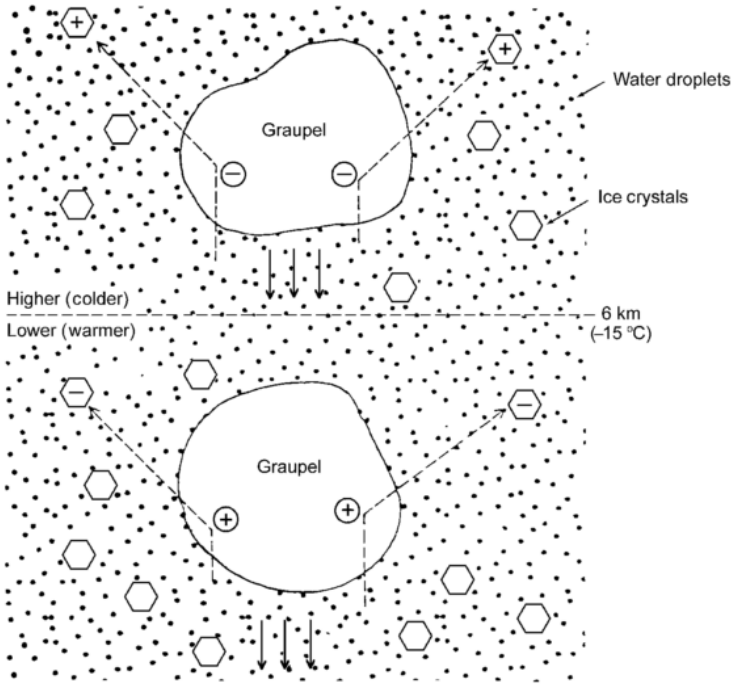

FIGURE 2.4: Illustration of charge accumulation mechanism for Graupel above and below the reversal temperature (dotted line). At the top part the falling Graupel is gaining negative charge by collision, while after the reversal temperature it gains positive charge. Figure from [Rakov and Uman, 2003].

Other factors that are involved in determining the polarity and magnitude of the electric charge attained in collisions are ice crystal sizes, supercooled droplet sizes,

relative velocity of collisions, cloud water content and chemical contaminations. The size of the droplets is thought to affect how many charge sign reversal temperatures there are. For 10 μm droplets there may be more than one, and for sizes under 4 μm there will be four reversal temperatures [Jayaratne, 1998]. Jayaratne [1998] suggested that these reversals could explain the multi-layer cloud charge distributions observed and reported by others.

Convection mechanism

The Convection mechanism uses external sources, such as cosmic rays and fair weather space charges to explain the electric charges deposited in the clouds. Here warm air currents will carry positive fair-weather space charges towards the top of the cloud. Above the cloud, negative electric charges are created by cosmic rays. The negative electric charges are attracted to the positive charges in the boundary of the cloud, and will attach to the cloud particles to create a screening layer. Cooling and convective circulation leads to downwards drafts that will carry the negative charge down the sides of the cloud, and towards the cloud base. This produces positive corona at the Earth's surface, which in turn will generate additional positive charge under the cloud. The process is illustrated in figure 2.5. This mechanism results in a positive cloud-charge dipole. In this mechanism the precipitating particles have no role, and do not contribute to the charges in the cloud.

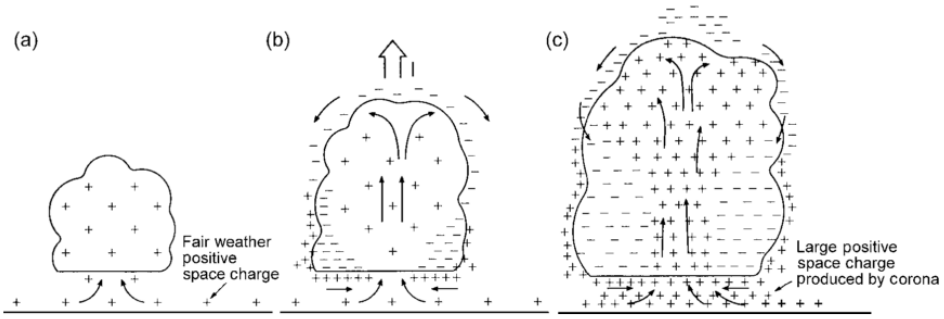

FIGURE 2.5: Illustration of cloud electrification via the Convection mechanism. a) The fair-weather charges are carried into the cloud and upwards by the warm air currents. b) the negative charges from cosmic rays are brought down the sides of the cloud and towards the bottom by downdrafts. c) positive corona at the Earth's surface generate large positive space charges at the bottom of the cloud. Figure from [MacGorman and Rust, 1998].

2.1.3 Lightning types

To describe and understand lightning flashes, it is important to use the a well defined terminology. A lightning flash is the same as a lightning discharge. A lightning strike refers to lightning discharges that involves the ground or other conducting objects, such as balloons or rockets. A lightning stroke or component stroke is a component of cloud to ground discharges [Rakov and Uman, 2003].

Lightning flashes are divided into two main classes: cloud to ground (CG) and cloud discharges. CG lightning are discharges from the cloud and into the ground, while cloud discharges consist of lightning discharges between clouds (Cloud to Cloud),

inside clouds (Intra Cloud lightning) or from a cloud to the air. The majority of lightning flashes are of the Intra cloud type [Rakov and Uman, 2003; Dwyer and Uman, 2014].

The lightning classes are further divided into positive and negative lightning, depending on the direction the electrons move in the lightning channel. The lightning is defined as positive when electrons travel upwards, and positive charge is transferred to the ground. This happens when a positive leader propagates downwards, or a negative leader propagates upwards. A negative lightning is then either a positive leader propagating upwards, or a negative leader propagating downwards.

Cloud to ground

Cloud to ground lightning is divided into four different types as shown in figure 2.6.

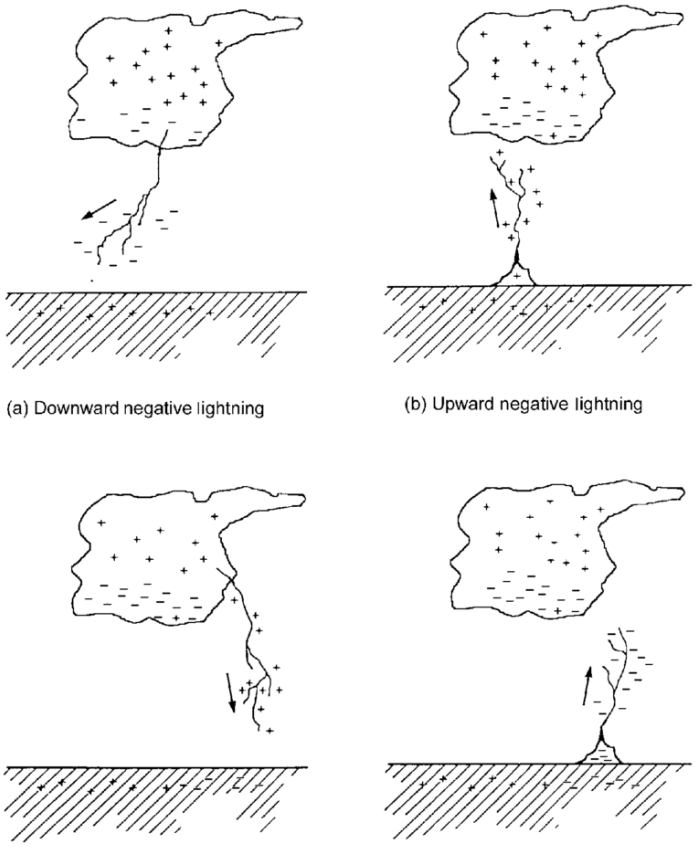

FIGURE 2.6: Illustration of the four classes of CG lightning. Figure from [Rakov and Uman, 2003].

The most common class of the cloud to ground lightning flashes is the Downward negative lightning (figure 2.6 (a)), which accounts for roughly 90% of all CG lightning. Downward positive lightning makes up approximately 10%, while the other two classes make up less than 1% of all CG lightning. Because of these observations upwards travelling lightning flashes are thought to only occur from tall objects, such as telecom towers and skyscrapers, or objects atop mountains [Rakov and Uman, 2003].

Cloud Discharges

As mentioned in chapter 2.1.3, cloud discharges are divided into 3 separate types, intra cloud (IC), cloud to cloud (CC) and cloud to air (CA). Intra cloud is the most common type of lightning discharge, but it is also one of the hardest to study because of the difficulty involved in acquiring visual recordings and getting measurements of the currents and charge transfers inside the cloud [Rakov and Uman, 2003].
Intra cloud lightning usually occur between the main negative charge centre, and the upper positive charge centre of a thundercloud. The intra cloud flash starts with a movement of negative charges from the main negative charge centre and upwards towards the positive charge centre. This creates a positive IC lighting. An alternative is that as the flash travels upwards, it can swap polarity, thus creating a negative IC lightning [Cooray, 2014].

2.2 Streamers and Leaders

This section will outline the physical processes involved during a lightning flash.
For a lightning discharge to happen, the thundercloud charges need to make an electric field of sufficient strength to cause an electrical breakdown of the air. This means that the electric field is sufficient for the ionisation processes to overcome the de-ionisation processes in air, resulting in an increase of free electrons. The electric field strength necessary for electrical breakdown to occur in air is $E_k \sim 32\,\mathrm{kV/cm}$ [Cooray, 2014].

In a strong electric field, a single electron may gain enough energy to free secondary electrons via ionizing collisions with atoms. Under the influence of a strong electric field, these secondary electrons can free more electrons via new ionizing collisions. This event is called an electron avalanche, and is illustrated in figure2.7. As the avalanche continues to grow, the electric field created by the charges at the avalanche head will start to modify the electric field in its vicinity. When the electric field around the avalanche head reaches a critical value the avalanche will be converted into a streamer discharge. This transition takes place when there are $\sim 10^8$ charged particles at the avalanche head [Meek, 1940]. The streamers are divided into positive or negative streamers, based on how they initiate and propagate. This will be discussed in chapter 2.2.1 and 2.2.2

The temperature of the streamer stem will increase due to the streamer currents, and when the temperature reaches a critical value the conductivity of the stem will increase. The streamer will then convert itself to a leader. According to Rakov and Uman, this happens when the conductivity of the streamer reaches values on the order of $10^4\,\mathrm{S/m}$ [Cooray, 2014; Rakov and Uman, 2003]. Leaders are also divided into positive and negative leaders, depending on the how they are initiated and how they propagate. This will be discussed in chapter 2.2.4 and 2.2.5

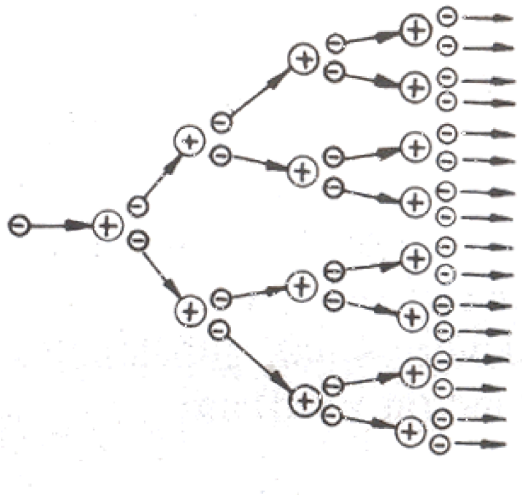

FIGURE 2.7: Illustration of an electron avalanche, where electrons are being freed by ionising collisions. Figure from [NPTEL, 2009].

2.2.1 Positive streamers

The formation and propagation of positive streamers starts with an electron as described above. The electron avalanches will propagate towards the anode where the electrons will be absorbed, leaving behind a net positive space charge close to the anode. This extension of positive charge has effectively reduced the distance between the tip of the streamer and the cathode. The avalanche head is a strong source of energetic photons, due to recombination of positive ions and electrons. These photons can create new avalanches in the vicinity of the positive space charge. If the positive space charge is strong enough, the new electron avalanches will be attracted to it. The electrons from the secondary avalanches will be absorbed, leaving behind a new positive space charge, this time closer to the cathode. This process as illustrated in figure 2.8 repeats itself until a a channel of weakly conductive ion-electron plasma, called a positive streamer spans the gap between the anode and cathode. For the streamer to propagate like described above, an electric field of magnitude $E_{cr}^{+} \sim 5kV/cm$ is needed [Cooray, 2014].

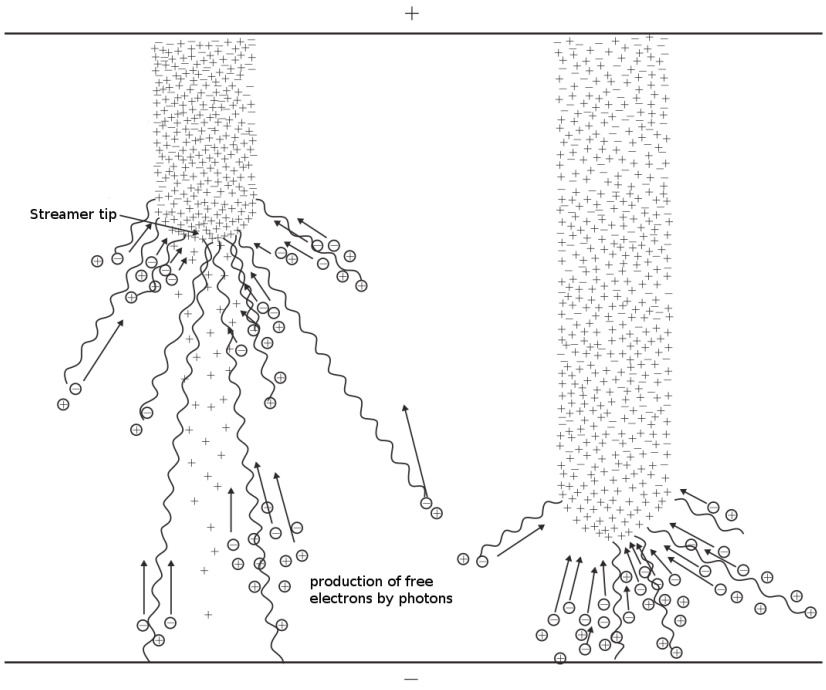

FIGURE 2.8: The positive streamer grows by absorbing electrons attracted to the positive charge at the growing streamer tip. Figure from [Loeb and Meek, 1940].

2.2.2 Negative streamers

Like the positive streamers, the negative streamers also start with an electron avalanche. The main difference between the streamer types is that the negative streamers will propagate from the cathode and towards the anode and that the streamer tip has a net negative charge. As the electron avalanche move towards the anode it will ionise the air, and leave behind a positive space charge which will be attracted towards the cathode. This will cause an electric field enhancement close to the cathode, which will cause the cathode to release electrons. The released electrons and the ions of the positive space charge will neutralize each other and form a conductive channel between the avalanche tip and the cathode, as illustrated in figure 2.9. This process repeats itself until the negative streamer spans the gap between the anode and cathode. The electric field needed in air for the negative streamer to propagate is $E_{cr}^{-} \sim 10kV/cm$ [Cooray, 2014].

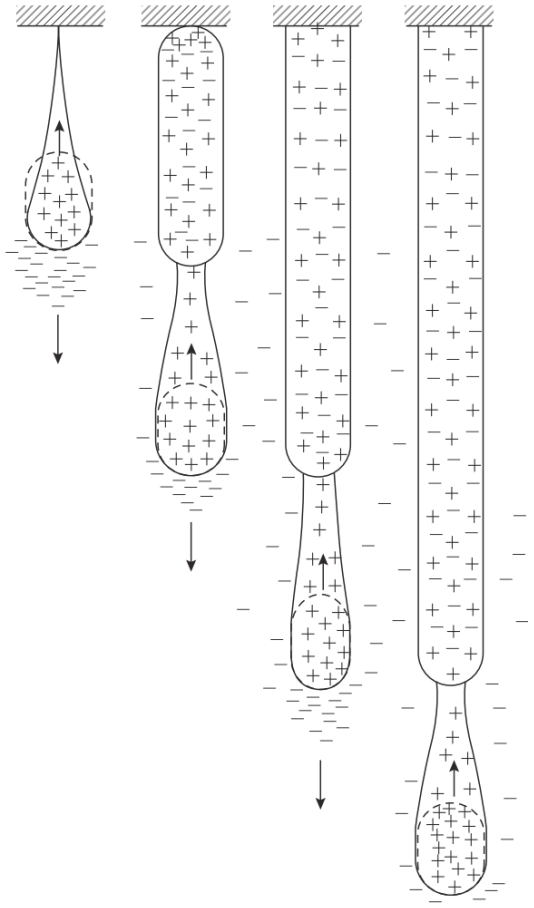

FIGURE 2.9: Illustration of the formation and propagation of a negative leader, as described in section 2.2.2. Figure from [Loeb and Meek, 1940].

2.2.3 Streamer to leader

The main differences between a streamer and a leader is its size and conductivity. Streamers are much smaller, and have lower conductivities than leaders. The formation of a leader can only occur when the ambient electric field is sufficient to sustain an electron avalanche. [Rakov and Uman, 2003]

The following is a summary of the streamer to leader step of a lightning flash, as observed from laboratory long sparks. If enough streamers form around a common stem, the combined current of all the streamers will lead to joule heating of the stem. The high temperature will lead to greater ionisation and electron production in the gas inside the stem, which in turn will make a highly conductive channel, known as a leader. The leader consists of a quasi neutral plasma, with an excess of either positive or negative charge, depending on the leader type. For the leader to stably propagate immediately after its inception, it needs an ambient electric field of ~ 100 kV/m [Cooray, 2014]. After the leader propagates out of the inception region, the potential gradient of the older leader channel will drop to values of the order of 1 kV/m. Due to the leader channels conductivity, a high electric field region will form at the leader tip, which will allow streamers to form and propagate in front of it. The leader will then propagate into the newly made streamer region and make it part of the leader [Bazelyan and Raizer, 2000].

2.2.4 Positive leaders

A positive leader will propagate in a similar manner as positive streamers. It starts when the positive streamers have made a positive leader stem, and the positive leader initiates and propagates out of the inception area. The positive charges in the positive leader head will enhance the electric field in front of the leader head, which will support streamer initiation and propagation. The positive leader will then propagate by absorbing more electrons from avalanches, resulting in a steady growth toward the negative space charge, as illustrated in figure 2.10 [Cooray, 2014; Rakov and Uman, 2003; Bazelyan and Raizer, 2000].

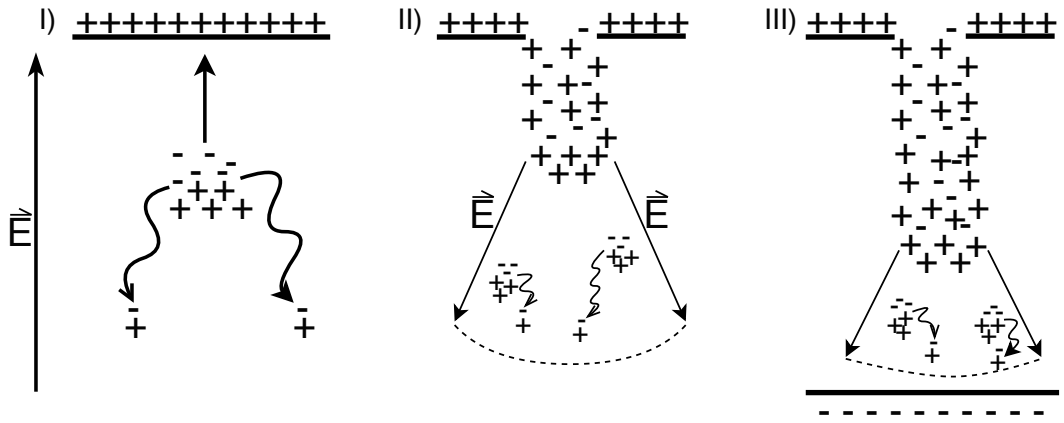

FIGURE 2.10: Formation and propagation of a positive leader. 1) An electron avalanche propagates towards a positive space charge region and creates the positive leader stem. 2) The positive leader extends as more and more electrons are absorbed. The high electric field at the positive leader head will support streamer initiation and propagation. 3) The positive leader propagates toward the negative charge region by absorbing electrons from electron avalanches.

2.2.5 Negative leaders

The formation and propagation of negative leaders are more complicated and less understood than that of positive leaders. Studies of negative leaders have shown that they propagate when electron avalanches are initiated and propagate towards the positive space charge (ie. away from the negative leader tip). The low mobility positive charges will be left behind, making a positive point charge close to the cathode. This positive space charge will attract electrons to it, creating what is called a space stem. This is the start of bidirectional leader, where the positive side of the space charge will have a positive streamer zone growing towards the cathode, and the negative side of the space charge will support negative streamer propagation towards the anode, as illustrated in figure 2.11. The negative part of the bidirectional leader will grow slowly away from the main negative leader, while the positive part will grow much faster, due to the increased electric field between the positive part and the main negative space charge. When the two streamer zones from the positive part of the bidirectional leader and main negative leader reach each other, the leader will make a step and extend to include the bidirectional leader. During the negative leader step the leader head will function as an ionizing wave [Kochkin et al., 2016], creating many new ions as it passes through the new "channel". This process is then

repeated until the negative leader reaches the anode or ground [Loeb, 1966; Cooray, 2014; Bazelyan and Raizer, 2000].

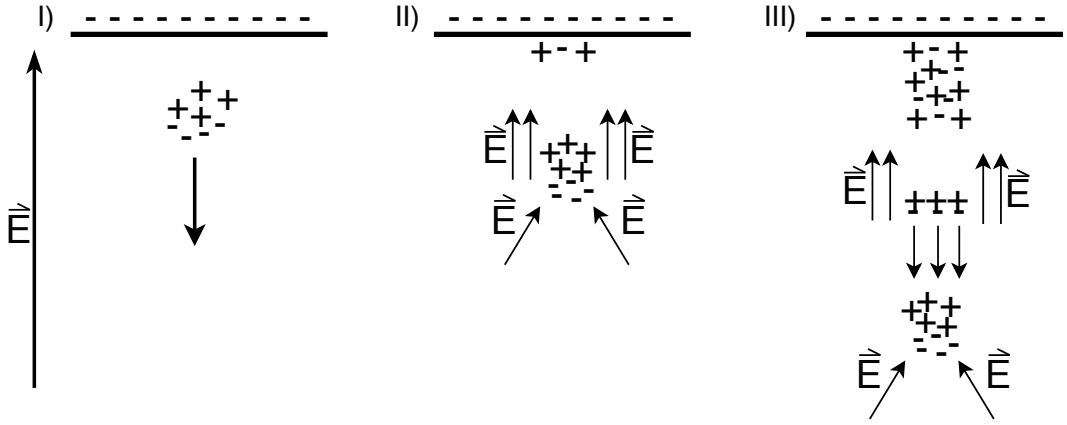

FIGURE 2.11: The formation and propagation of a negative leader. 1) The propagation of the negative leader starts when electron avalanches initiates and propagates away from the leader head, leaving behind low mobility positive charges. 2) The low mobility positive charges create a space stem. The space stem will intensify the electric field on both ends, resulting in electric fields sufficient to support streamers on both ends. 3) The electric field between the positive charges of the stem and the cathode reaches a critical value, and the leader makes a step and extends to include the space stem.

2.3 Acceleration of particles

2.3.1 Relativistic Runaway Electrons

The process by which electrons in strong electric fields gain large amounts of energy, enough to "run away" is called the runaway electron mechanism. This happens when the electric field is strong enough to make up for the energy lost by electrons due to collisions, which will let the electrons keep gaining energy and run away. This energy gain is limited by inelastic collisions with air molecules and bremsstrahlung. Figure 2.12 shows the frictional force (F_D) that the electrons will experience as they keep gaining energy. The dotted lines represent electric fields of different strengths needed to accelerate electrons. If the electric fields are larger than the friction force, the electrons can continue to gain energy and run away. The minimum electric field needed to create a runaway electron is called the break even field, which has a theoretical value of $E_t \sim 2$ kV/cm [Moss et al., 2006].

Electrons will lose or gain energy if the force from the electric field and the friction force are not equal. The electrons will gain energy if the electric field is dominating, and lose energy if the friction force is dominating. The electrons will then gain or lose energy until the two forces are equal again. As seen in figure 2.12 electrons starting from rest in an electric field will accelerate until the force of the electric field matches the friction force. To run away the electrons need to be accelerated by an electric field of atleast 32 kV/cm, this happens for electrons with energies from ~ 9 keV and up, this is shown in figure 2.12 as the vertical red line. An initial seed population is needed for the runaway mechanism to start. There are two main theories

on how these seed electrons are created.

In the seed electron theory the initial seed population is gained from cosmic rays, creating an energetic electron. This electron is then able to run away, and create new energetic electrons provided that the electric field is of sufficient strength. A newer alternative theory, is that the electric fields in front of streamer tips can have very large values for a short time, due to overlapping of streamer zones etc. This field can be large enough to accelerate electrons from rest to runaway energies. The electric field needed for this is called the thermal runaway electric field (E_c) and is roughly 260 kV/cm. Such a strong electric field will only exist very locally in overlapping electric fields in front of streamer tips. This mechanism is described in chapter 2.3.2 [Moss et al., 2006].

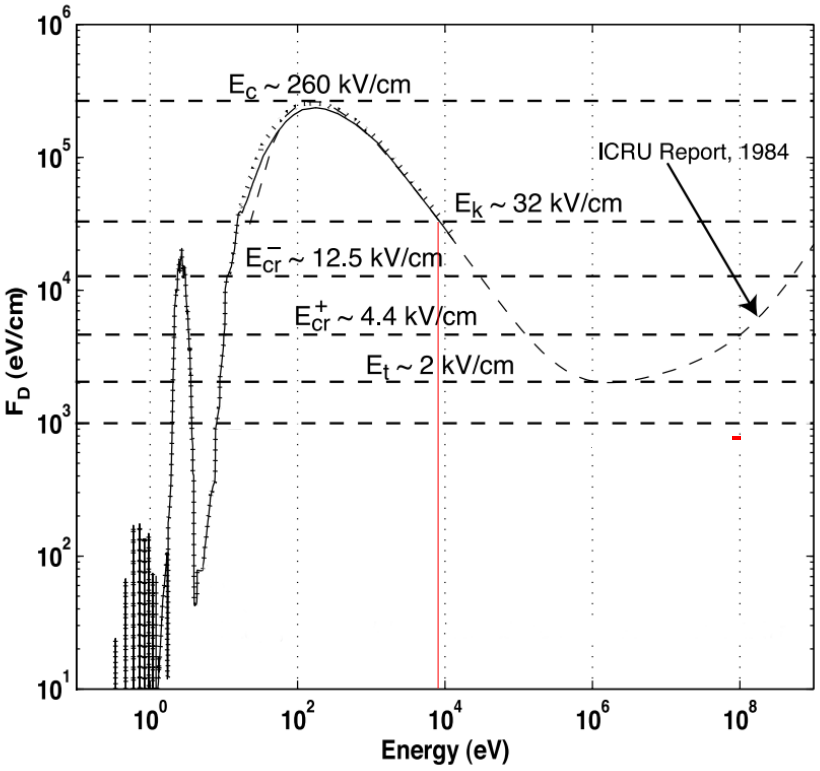

Thermal Runaway:	$E_c \sim 260$ kV/cm	Positive Streamer:	$E_{cr}^+ \sim 4.4$ kV/cm
Conventional:	$E_k \sim 32$ kV/cm	Relativistic Runaway:	$E_t \sim 2$ kV/cm
Negative Streamer:	$E_{cr}^- \sim 12.5$ kV/cm	Leader:	$E_l \sim 1$ kV/cm

FIGURE 2.12: Friction force experienced by electrons as a function of their energy. The dashed lines represent different electric fields. The red line shows the energy a photon would need to start running away. Figure adapted from [Moss et al., 2006]

2.3.2 Cold Runaway / Thermal Runaway

Cold runaway or thermal runaway as it is sometimes called, is a mechanism for producing relativistic runaway electrons. Low energy electrons can be accelerated by overlapping high electric fields, in front of the streamer heads. If the electric field exceed a critical value E_C in figure 2.12, the thermal electrons can runaway. Negative streamers have been found to emit runaway electrons with energies up to $\sim$ 100 keV,

which could be further accelerated by the potential energy of the electric fields at the negative leader tip [Celestin and Pasko, 2011] or in a large ambient electric field.

2.4 Energetic particles

2.4.1 Electron interactions with air

Electrons can interact with air in many different ways. The two interactions important for this thesis are ionisation and bremsstrahlung.

Ionisation

In an electric field, electrons will gain energy, which can be transferred to molecules in inelastic collisions. The minimum energy needed to create a free electron and ionise a molecule is called the ionisation energy. If the electrons energy is above this limit, it will ionise the molecule in such a collision, and free an electron from the molecule. This process is referred to as an electron ionisation, and is shown in equation 2.6 [IUPAC, 1997].

$$XY + e^- \rightarrow XY^+ + e^- + e^- \tag{2.6}$$

If the electron in the collision has a lower energy than this, only part of its energy will be transferred to the molecule. The molecule will use the absorbed energy to move one of its electrons to a higher energy orbital, as seen in equation 2.7.

$$XY + e^- \rightarrow XY^* + e^- \tag{2.7}$$

The excited molecule is not stable, and further electron collisions could ionise the molecule, which could free the loosely bound electron. If this does not happen, given a short time the electron will move back to its lower energy orbital and emit a photon with the equivalent energy to the electrons orbital energy difference.

$$XY^* \rightarrow XY + \gamma \tag{2.8}$$

Bremsstrahlung

Bremsstrahlung is the mechanism by which electrons are retarded in a Coulomb field of an atomic or molecular nucleus and as a result emit radiation (shown in figure 2.13). According to Maxwell's theory, the energy loss from this retardation is at a rate proportional to the square of the acceleration [Cember and Johnson, 2009]. The acceleration loss is again dependent on the size of the nucleus and how close to the nucleus the electron is passing. Since the electrons can decelerate at various rates, the resulting photons have a continuous energy spectrum up to the electrons total energy. The energy spectrum of the photons are however heavily skewed towards the lower end since most electrons are decelerated in a series of collisions rather than in one or two large collisions [Cember and Johnson, 2009].

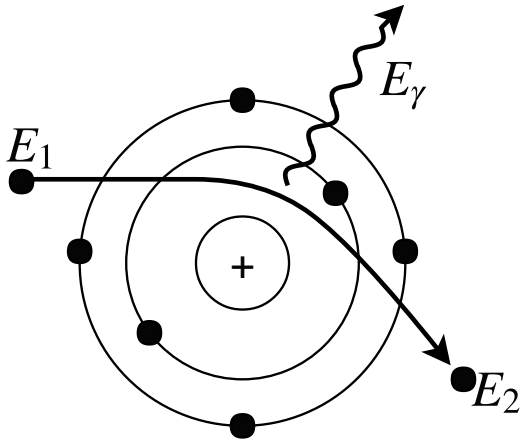

FIGURE 2.13: Bremsstrahlung of an electron in the Coulomb field of an atomic nucleus.

Electron range in air

Unlike photons, electrons and other charged particles are subject to the coulomb forces of other charged particles in a medium. The energy of the electrons will be attenuated in interactions with matter and/or coulomb fields, some of which are mentioned above. The loss of energy E per unit length of medium is called the *linear stopping power* of the medium. It is given as:

$$S(E) = -\frac{dE}{dx}[N]or[MeV/mm] \tag{2.9}$$

The mean stopping range can then be found by integrating the expression, giving:

$$\Delta x = \int_0^{E_0} \frac{1}{S(E)} dE \tag{2.10}$$

Figure 2.14 shows the range of electrons in air.

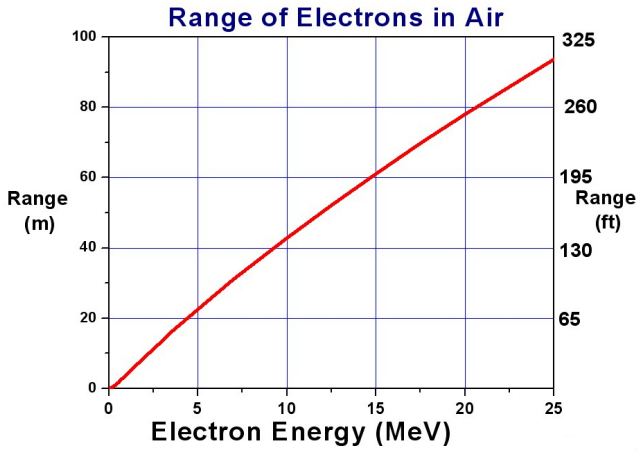

FIGURE 2.14: The range of electrons in air. Figure from [Berger et al., 2017], plotted by Berger and Selzer.

As seen, electrons with energies under 1 MeV do not go very far in air, before being fully attenuated.

2.4.2 Photon Interactions with air

Photons are uncharged radiation without mass, that moves with the speed of light. Unlike charged particles, photons are electrically neutral and can only interact indirectly with matter. There are three main interaction processes of photons with matter. The interaction depends on the photons energy and the absorbing matter. Figure 2.15 shows the dominant processes for photon interaction with matter as a function of photon energy and atomic number [Cember and Johnson, 2009].

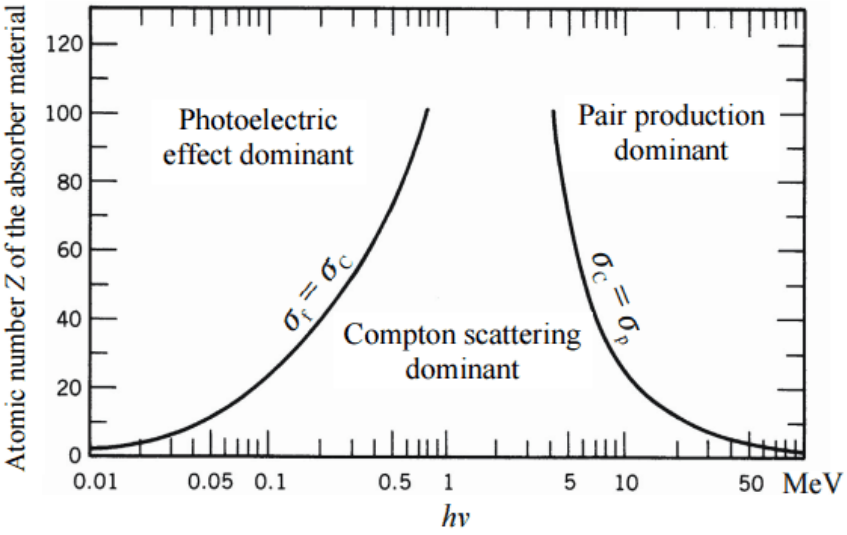

FIGURE 2.15: The dominant mechanisms of photon - matter interactions. Figure from [Thorsteinsen, 1995].

The interactions of photons with air is shown in figure 2.16. As seen here, the photoelectric effect will dominate at energies lower than $\sim$ 60 keV, Compton scattering dominates from $\sim$ 60 keV to $\sim$ 17 MeV and above this energy, pair production dominates. The red line in figure 2.16 shows the total absorption of energy in air. As seen, photons with energies below 60 keV are heavily absorbed in air.

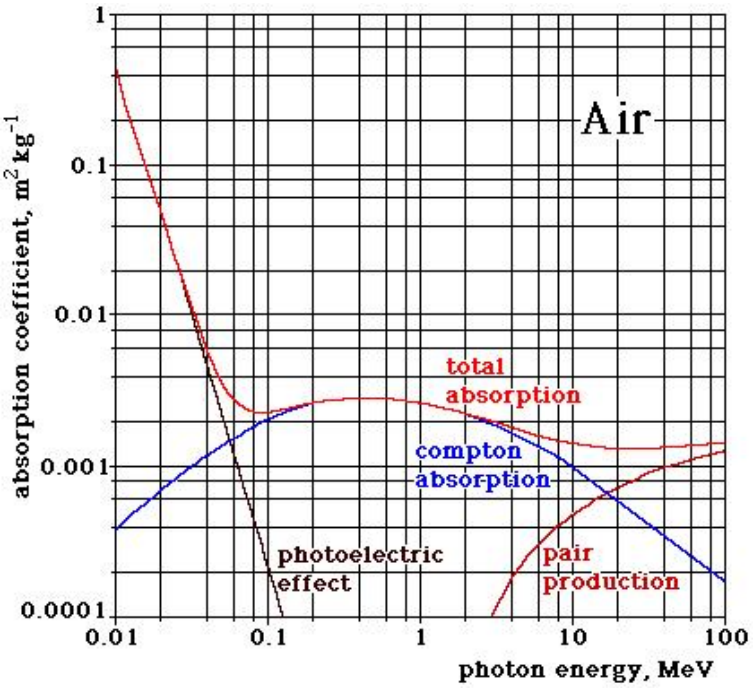

FIGURE 2.16: The dominating mechanisms of photon interactions with air. Figure from [UCL-Lecture-Notes, 2009].

Photoelectric effect

In the photoelectric effect the photon is fully absorbed by a bound electron of an atom/molecule. This will liberate and accelerate the electron, and ionise the atom/molecule. The kinetic energy of the free electron is given by equation:

$$E_K = hf - \phi \tag{2.11}$$

Where E_K is the kinetic energy of the electron after being liberated, hf is the energy of the incoming photon and ϕ is the ionisation potential, most commonly referred to as the work function. The ionisation potential is the energy needed to free an electron from the atom/molecule and ionise it.

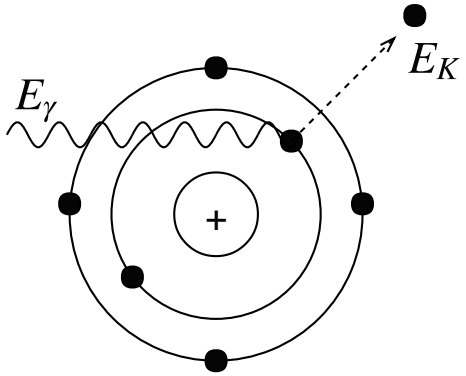

FIGURE 2.17: Illustration of the photoelectric effect, where we see an incoming photon freeing an electron from the K-shell of an atom.

The excess energy of the atom/molecule will be emitted from the atom/molecule as an X-ray photon with a wavelength characteristic for that atom/molecule, or if

the ejected electron is from an inner shell, the energy might be spent by moving an electron from one of the outer shells to the now vacant spot [Beiser, 2004]. This will release more energy from the atom/molecule, which in turn can free a new electron. This emission of secondary electrons is called the Auger effect.

Compton scattering

At photon energies of $\approx$ 60 keV to 20 MeV, the dominant interaction in air is the Compton scattering. Here the photon will collide and be partially absorbed by an outer orbital electron of an atom/molecule. The collision will lead to the loss of some of the photons energy, and will scatter it at an angle from its original path. The relation to the shift in wavelength and scatter angle is given as:

$$\lambda' - \lambda = \Delta\lambda = \frac{h}{m_e c_0}(1 - cos\theta) \tag{2.12}$$

Where λ and λ' are the photon wavelengths before and after collision, θ is the scattering angle, and the fraction is a constant called the Compton wavelength of the electron, which is approximately $2.43 * 10^{-12}$ m or $\sim$ 5.1 keV [Beiser, 2004].

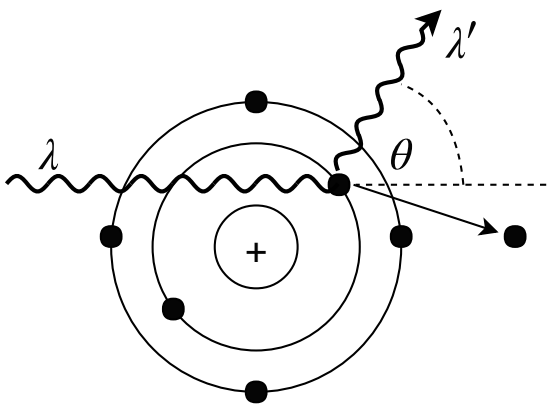

FIGURE 2.18: Compton scattering: Scattering of a photon on the outer orbital electron of an atom/molecule.

The shift in wavelength of the photon is then dependent only on the scattering angle. The largest change is when the photon backscatters, which makes the wavelength change equal to two Compton wavelengths [Beiser, 2004]. Using relativistic energy - momentum relationship and assuming the electron was at rest before the collision, the energy of the electron after the scattering is given as:

$$E_{e'} = \sqrt{(p_{e'}c)^2 + (m_e c^2)^2} = hf + m_e c^2 - hf' = E_\gamma + E_e - E_{\gamma'} \tag{2.13}$$

Where $p_{e'}$ is the electrons momentum, m_e is the rest mass of the electron and f and f' the frequency of the photon before and after scattering.

Pair Production

For high energy photons the dominant interaction is pair production. Pair production is a mechanism by which electromagnetic energy is converted into matter, by

a photon materializing into an electron and a positron (anti particle to electrons) in the Coulomb field of a nucleus.

$$\gamma \rightarrow e^- + e^+ \tag{2.14}$$

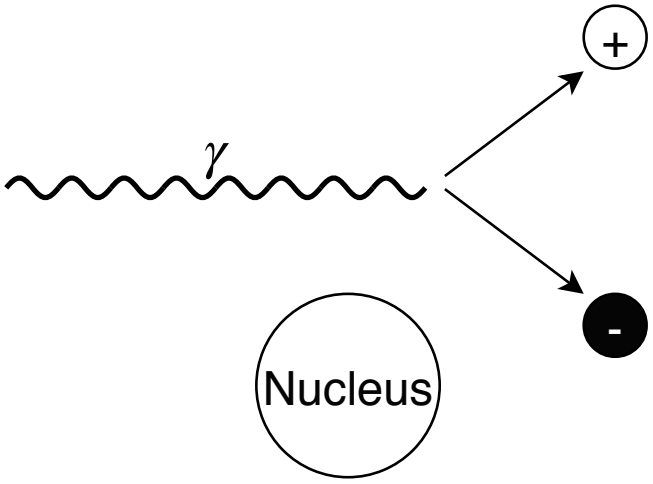

FIGURE 2.19: Pair production where a photon materializes into an electron-positron pair in the presence of a Coulomb field.

The energy of the photon must be higher than the rest mass energies of the electron positron pair i.e. $E_\gamma > 1.022 MeV$. This conversion of electromagnetic energy to matter does not violate the conservation principles, as the sum of charges from the positron (q = +e) and electron (q = -e) is zero. The total energy of the electron and positron also equals the photon's energy. Pair production has to happen in the presence of a nucleus, which will absorb some of the photon's momentum and thereby satisfy the conservation of momentum principle. The mass of the nucleus is massive compared to the electron and positron, so it will only absorb a negligible fraction of the photon's energy [Beiser, 2004].
The reverse of pair production is called electron-positron annihilation. This happens when a electron and a positron are attracted to each other and collide. Both particles will annihilate and the lost mass will become electromagnetic energy in the form of two photons. Two photons or more photons must be created to satisfy the conservation of energy and linear momentum. In most cases two photons are created, with energies equal to the rest energy of the electron/positron (0.511 MeV) [Beiser, 2004]. This energy is well over the threshold needed to run away. The positrons will runaway in opposite directions of the electrons.

$$e^- + e^+ \rightarrow \gamma + \gamma \tag{2.15}$$

2.5 Attenuation of photons.

When x- and gamma rays propagate through matter, the intensity of ray will be attenuated, due to the processes explained in chapter 2.4.2. The intensity I of an x- or gamma ray after going through a medium is given as:

$$I = I_0 e^{\mu x} \tag{2.16}$$

Where I_0 is the intensity before attenuation, x is the thickness of the absorbing medium and μ is the linear attenuation coefficient. The linear attenuation coefficient is dependent on the energy of the photons and the absorbing material. The fraction of energy lost is then given as:

$$-\frac{dI}{I} = \mu dx \tag{2.17}$$

The mass attenuation coefficient (μ/ρ) for 100 keV photons in dry air close to sea level is given as 0.154 cm^2/g [Hubell and Seltzer, 2004]. The density of air close to sea level is $1.225 \cdot 10^{-3} g/cm^3$. This gives the following approximate of linear attenuation coefficient:

$$\frac{\mu}{\rho} = 0.154 cm^2/g \rightarrow \mu = 1.8865 \cdot 10^{-4} cm^{-1} \tag{2.18}$$

For a photon to lose 99% of its intensity, it would have to travel:

$$x = \frac{ln(I_0/I)}{\mu} = \frac{ln100}{1.8865 \cdot 10^{-4} cm^{-1}} \approx 244m \tag{2.19}$$

Figure 2.16 shows the relationship between photon energies and attenuation.

2.6 Lightning interaction with aircraft

Lightning strikes to aircraft can be separated into two categories. Flashes initiated by the aircraft itself or discharges in progress, intercepted by aircraft. The majority of lightning strikes to aircraft are not intercepted, but initiated by the aircraft itself [Uman and Rakov, 2003]. The most probable region for aircraft initiated flashes are within the cloud [Fisher et al., 1977], in the area where the temperature reach freezing levels (0 °C). The vast majority of aircraft initiated lightning is also associated with precipitation particles, which can cause static charging of the aircraft [Uman and Rakov, 2003].

2.6.1 Aircraft-initiated lightning (Type 1)

The start of an aircraft initiated lightning discharge happens when the conductive aircraft flies into a sufficiently high ambient electric field. In the presence of an ambient electric field, the aircraft will become polarized, and the local electric field on the aircraft and its vicinity will be amplified at the extremities aligned with the ambient electric field. [Fisher et al., 1977; Morgan et al., 2012]. The most intense amplification will be observed at the sharper parts of the aircraft, like the nose, tail and wing tips. This is due to the compression of equipotential lines around the aircraft. An electrostatic model of this can be seen in figure 2.20. Here we see that the electric field around the sharp parts are intensified, up to ten times the ambient electric field value.

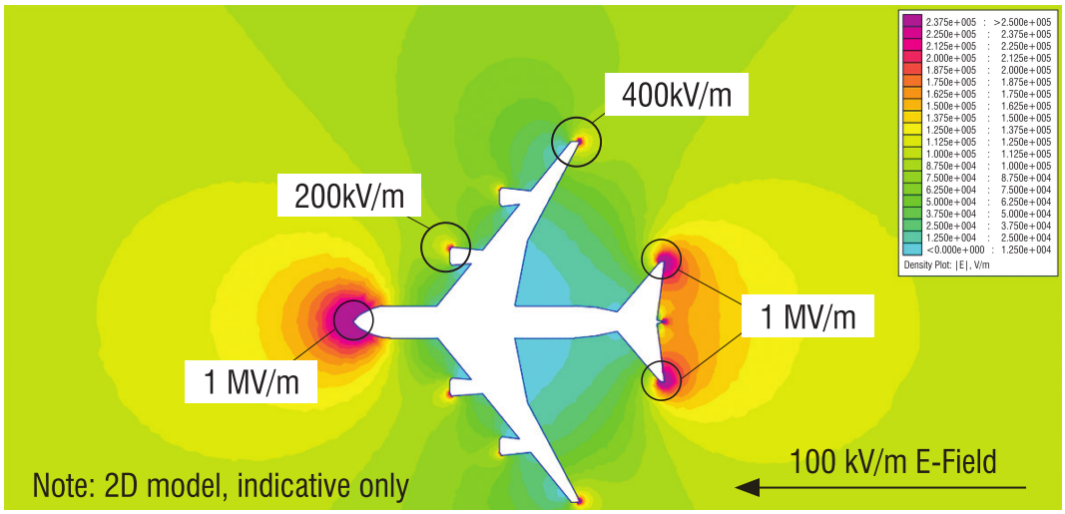

FIGURE 2.20: Electrostatic model of an aircraft in a 100 kV/m ambient electric field. As seen the amplification of the local electric field around the sharper edges of the aircraft are large, reaching up to 10 times the ambient electric field value. Figure from [Morgan et al., 2012]

This intensification of the local electric field can lead to the initiation of a lightning discharge [Fisher et al., 1977]. The mechanism describing lightning initiation for a conducting object not attached to the Earth is referred to as the bidirectional leader theory [Kasemir, 1983]. This bidirectional leader is similar to the stem observed during negative leader propagation (chapter 2.2.5). The basis for this theory is that positive and negative leaders are like two ends of a "tree" that will extend towards charge regions of opposite polarity [Kasemir, 1960; Montanyà et al., 2014]. The bidirectional leader will initiate with a positive leader, but in some cases a negative corona discharge will precede the positive leader initiation. The leaders will extend from the aircraft and connect with oppositely charged regions in thunderclouds, resulting in an aircraft triggered lightning flash [Morgan et al., 2012].

Positive bidirectional leader initiation

Positive leaders will most often occur first in the bidirectional leader development, since the positive streamers initiate and propagate in lower electric fields than negative streamers. The process can be divided into different phases.

First the positive leader will initiate and propagate in the direction of the ambient electric field. The positive leader will attract negative charge, making the nose of the aircraft less positive. This results in an increase in the measured local electric field towards the detector [Uman and Rakov, 2003] as seen in phase A of figure 2.24.

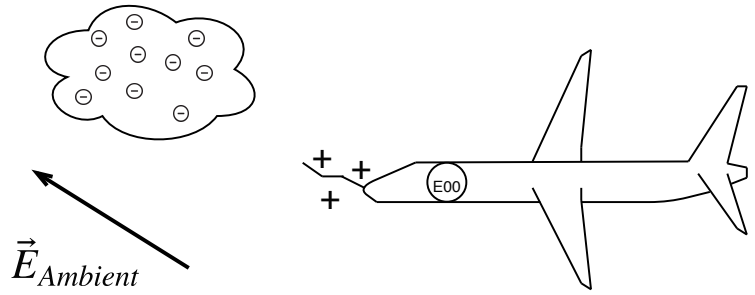

FIGURE 2.21: Phase 1: The positive leader is initiated, and in the same direction as the ambient electric field.

Phase 2 starts a few milliseconds later when a negative leader initiates from a different extremity of the aircraft, and propagate in the opposite direction of the ambient electric field. The negative leader will step (see chapter 2.2.5), which will give characteristic steps in the measured local electric field (shown in figure 5.3). The negative leader will transport electrons away from the aircraft faster than the positive leader will attract negative charge, resulting in the measured local electric field pointing away from the detector during this time, as seen in phase B of figure 2.24.

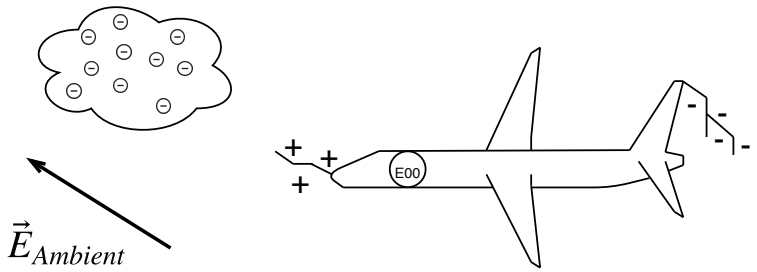

FIGURE 2.22: Phase 2: Initiation and propagation of the negative leader from a different extremity of the aircraft.

Phase 3 is defined as when the positive leader starts to gain speed and starts branching. This increases the positive leaders ability to remove charge from the aircraft, and the measured local electric field will once again point towards the sensor [Uman and Rakov, 2003] as seen in phase C in figure 2.24.

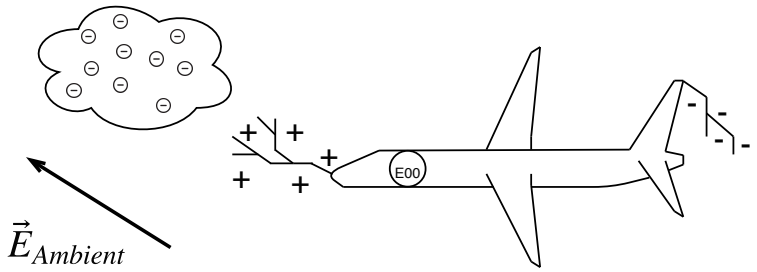

FIGURE 2.23: Phase 3: The positive leader gains speed and starts to branch.

The bidirectional leaders may then connect to oppositely charged regions in thunderclouds and trigger a lightning flash, with the aircraft itself as a part of the lightning channel [Morgan et al., 2012].

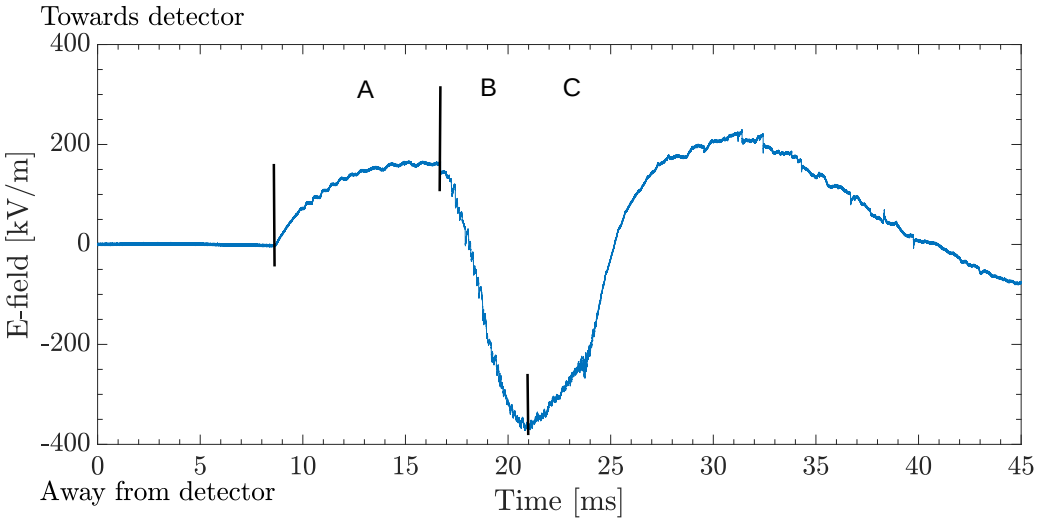

FIGURE 2.24: Local electric field during a bidirectional leader initiation and propagation. A positive increase on the graph symbolises an increasing negative local electric field. Phase A is where the positive leader is launched; phase B is where the negative leader is launched; phase C is where the positive leader gains speed and starts to branch.

Positive bidirectional leader preceded by negative corona

A less understood version of bidirectional leader initiation involves negative coronal discharge. Here, a negative corona occurs before the initiation of the positive leader (figure 2.25). For the negative corona to start, the aircraft has to be pre-charged. As seen in figure 2.28 the local electric field before the negative corona is at zero. This suggests that the charging of the aircraft happened slowly over time, which is why the detectors do not register the change in the local electric field. The negative corona will remove electrons from the aircraft, making the local electric field point away from the detector, as seen in phase A of figure 2.28.

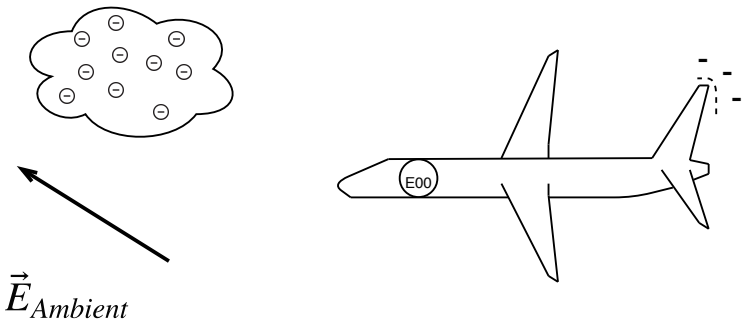

FIGURE 2.25: A negative corona occurs at an extremity.

The positive leader is then launched from a different extremity, and will propagate in the direction of the ambient electric field. This will attract negative charge to the aircraft, making the measured local electric field point towards the sensor [Mazur, 1989] as seen in phase B of figure 2.28.

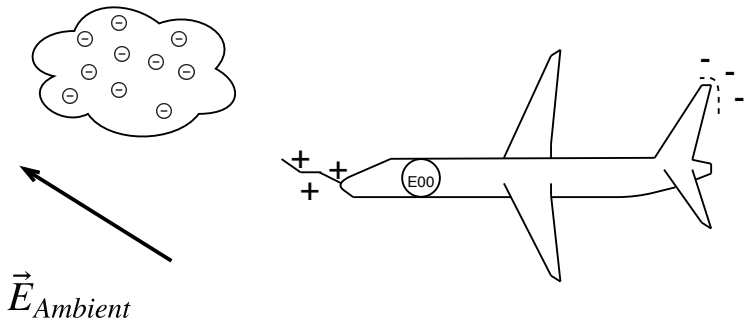

FIGURE 2.26: The positive leader initiates and propagates along the direction of the ambient electric field.

A few milliseconds later the negative corona will evolve into a negative leader, this third phase is hard to see only from the electric field, as it is defined by pulses in the current [Mazur, 1989]. The negative leader will propagate in a step-like manner in the opposite direction of the ambient electric field, removing negative charge from the aircraft, again turning the measured electric field more positive [Mazur, 1989].

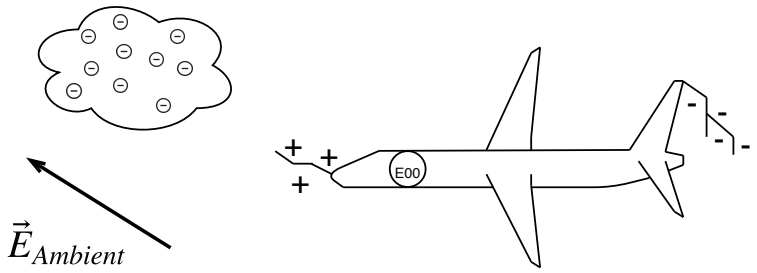

FIGURE 2.27: The negative leader initiates and propagates in the opposite direction of the ambient electric field.

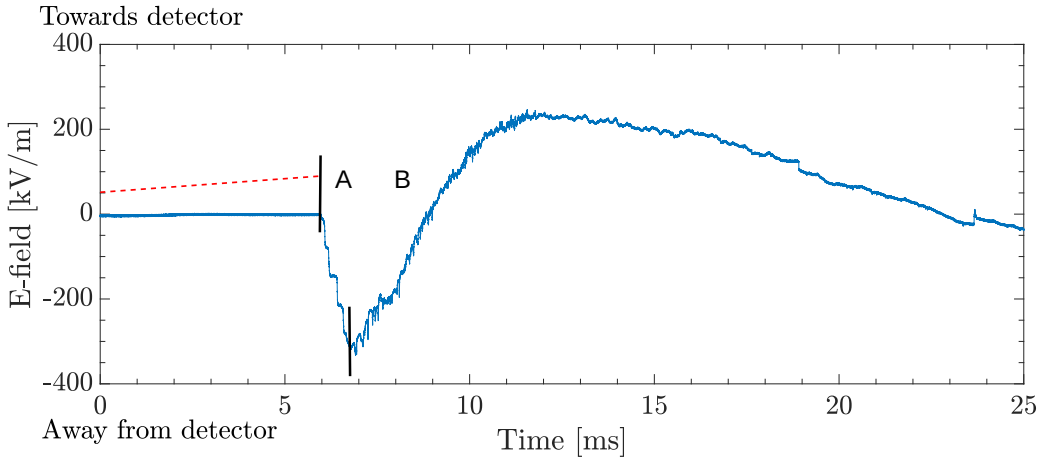

FIGURE 2.28: Local electric field during a bidirectional leader initiation and propagation with preceding negative corona. In Phase A the negative corona starts, and in Phase B the positive leader initiates. The red line before phase A symbolise the slow charging of the aircraft, needed to initiate negative corona. It is not clear where the negative leader starts.

2.6.2 Aircraft-intercepted lightning (Type 2)

The aircraft can also intercept lightning discharges already in progress. This happens less often than aircraft-initiated discharges, with only about one in ten strikes being intercepted, rather than initiated [Morgan et al., 2012]. Aircraft intercepted lightning occurs when the aircraft gets polarised due to the electric field of an approaching leader. This will increase the local electric field like for aircraft initiated lightning, and the aircraft can initiate a bidirectional leader that will be attracted to the propagating leader from the cloud. Most of the aircraft intercepted lightning are of the cloud to ground type [Morgan et al., 2012].

Chapter 3

Instruments and Data

The In-flight Lightning Strike Damage Assessment System (ILDAS) is an EU funded project to make a system for determining the attachment points, measure lightning current waveforms and assess possible structural damage to aircraft, after a lightning strike. ILDAS is a collaboration of twelve companies from five European countries, including the Dutch National Aerospace Laboratory (NLR), Airbus, Eindhoven University of Technology and others. The sensors were developed by Eindhoven University of Technology, the measurement electronics were developed by the NLR, who were also the project coordinators. The instruments were mounted on an Airbus A350 and later an A340, that was performing icing tests [NLR, 2009; Deursen et al., 2012]. Icing tests take place at the 0 °C temperature height, which is where one expects to find the main negative charge centre in thunder clouds (see chapter 2.1).

3.1 Campaigns

To this day the project has had 3 major aircraft campaigns, with a fourth in the planning stage.

Campaign	Location	Days	Altitudes	Lightning detections
2014	Southern Europe	6	4 - 5 km	61
2015	Southern Europe	3	4 - 5 km	85
2016	Northern Australia	6	9- 11 km	48

TABLE 3.1: Overview of ILDAS campaigns, with location, campaign days and registered flashes.

3.1.1 2014 and 2015

The 2014 and 2015 campaigns were based in Toulouse (France) and the flights took place mostly over southern Europe and the adjacent regions, using an Airbus A350 test aircraft, with a hull made of mostly carbon fibre reinforced plastics (53 %). The campaign lasted for six days from April to early May in 2014 and 3 days late in may 2015. During these campaigns ILDAS registered and collected data from 61 and 85 aircraft-triggered discharges. A single aircraft-intercepted lightning flash was also observed during the 2014 campaign.

Typical flight altitude for icing tests over southern Europe was 4 - 5 km, figure 3.1 shows the flight path and altitude from one day of the 2015 campaign, where data on 73 aircraft-triggered discharges were gathered.

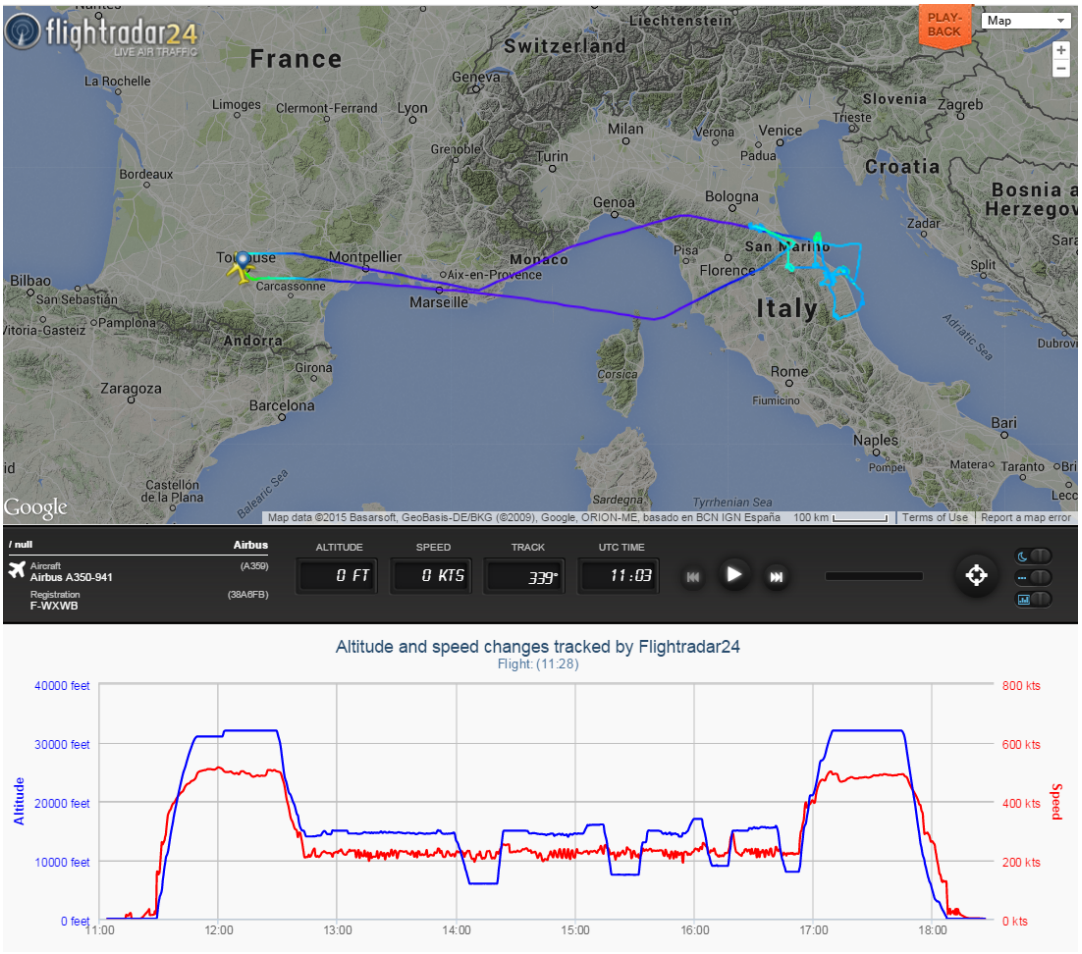

FIGURE 3.1: Flight path, velocity and altitude for the ILDAS flight on 24/05/2015. Image from [FlightRadar24, 2015].

3.1.2 2016

The 2016 campaign were based in Darwin (Australia) and took place over the Northern Territory in Australia, using an Airbus A340 test aircraft, with a hull made of mostly aluminium. The campaign consisted of four flights in January and two in February. During this time data of 48 aircraft-triggered discharges were registered and collected. Typical flight altitudes over Australia was 9 - 11 km. Figure 3.2 shows the flight path, velocity and altitude of the ILDAS flight for one of the days of the campaign.

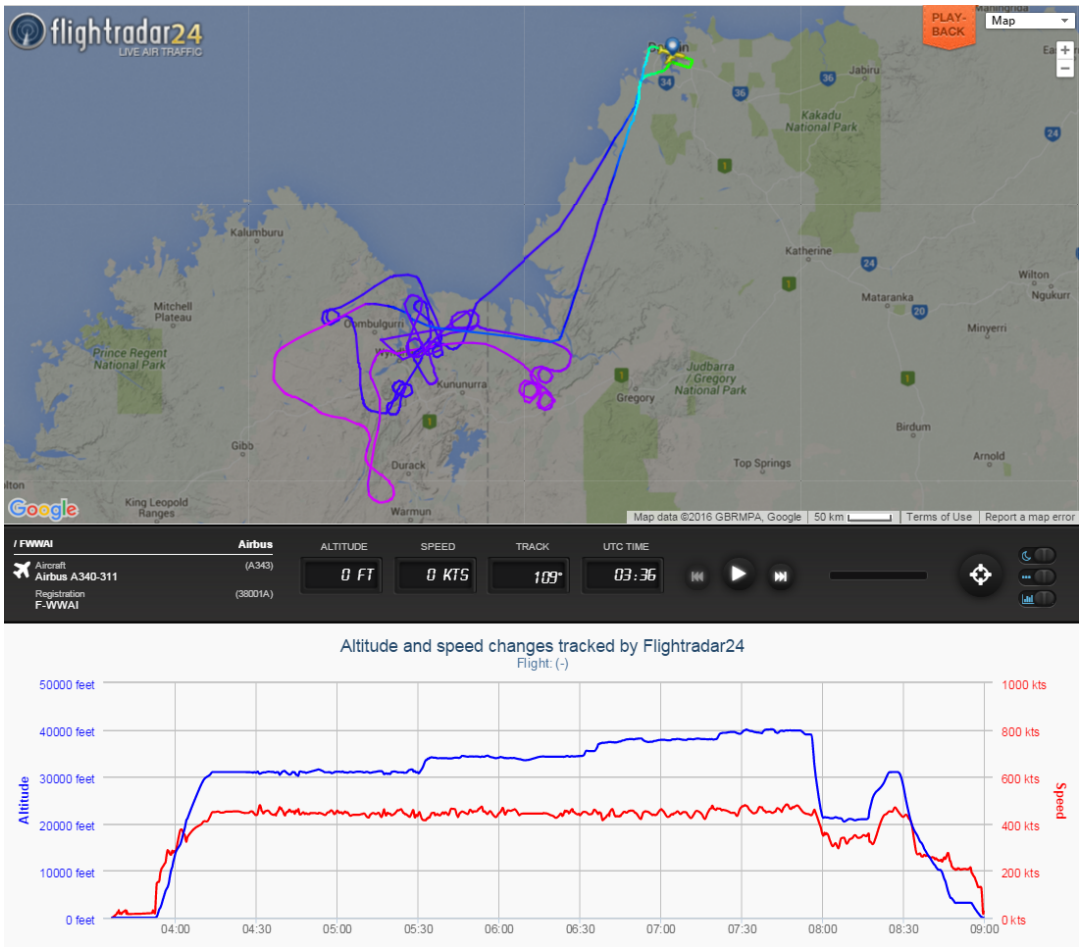

FIGURE 3.2: Flight path, velocity and altitude for the ILDAS flight on 15/01/2016. Image from [FlightRadar24, 2015].

3.2 Equipment

ILDAS is composed of eight magnetic field sensors, one electric field sensor and two x-ray detectors mounted on an aircraft. The distribution of the instruments are shown in figure 3.3. The distribution and amount of instruments of ILDAS has changed many times. The instrument distribution during the 2014-2016 campaigns were set up to minimise the amount of detectors on the aircraft, while still having full current coverage.

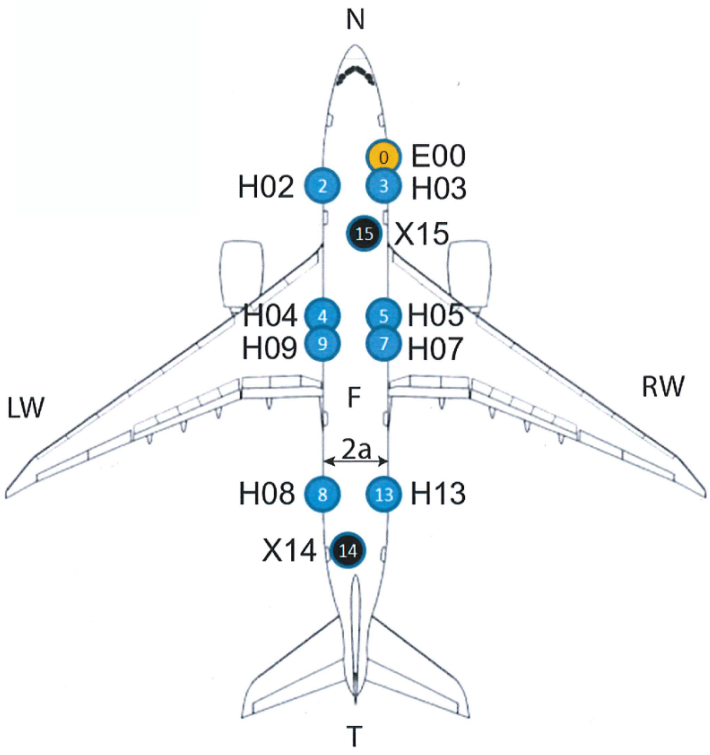

FIGURE 3.3: Instrument distribution on the aircraft. The Sensors named H are all H-field sensors, E the on board electric field sensor and X the X-ray sensors. Picture from [Kochkin et al., 2015a]

All the instruments on ILDAS have been through a verification process where the instruments were calibrated and the system's measurment and data handling performance were measured and confirmed [Zwemmer et al., 2009]. This was done both with a simulated lightning test in a laboratory on a rig with all the instruments, then with ground tests on an Airbus A320 aircraft fitted with the ILDAS instruments.

3.2.1 E-field Sensor

The E-field sensor's main purpose is to trigger data recording during lightning flashes. The sensor consists of a capacitive probe which is attached to a window on the aircraft [Kochkin et al., 2015a]. The sensor is mounted near the edge of the window, to enhance the local electric field over the near homogeneous field on the fuselage. The fuselage is a long conducting tube, so the electric field will always be perpendicular to the aircraft fuselage. The E-field sensor is a differential detector, where the signal is integrated over time, to reflect the actual changes to electric field. The zero value is therefore an electric field of unknown magnitude, which is approximately the value of the ambient electric field.

The polarity of the sensor is chosen in such a manner that a positive signal corresponds to electric field lines pointing towards the detector[Kochkin et al., 2015a], and a negative signal correspond to electric field lines pointing away from the detector. The characteristics of the sensor is listed in table 3.2.

	E-field sensor
Sampling Rate	83.3 MS s^{-1}
Sampling Time	12 ns
Dynamic Range	96 dB over 10 Hz - 500 kHz
Time span (trigger mode)	1.2 s

TABLE 3.2: Characteristics for the E-field sensor.

3.2.2 H-field Sensors

The H-field sensors are used to find the current passing through the hull of the aircraft. The H-field sensors are also differential detector, where the signal is integrated over time. This means we can not measure constant currents through the aircraft.
For a simplified model of the aircraft without windows, the aircraft can be viewed as a conducting tube of radius a. Assuming the lightning current I going from nose to tail is homogeneously distributed over the circumference of the aircraft, the magnetic field inside the fuselage will be zero. The outer fuselage will have a magnetic field corresponding to:

$$H_0 = I/2\pi a \tag{3.1}$$

which will be orthogonal but equal in magnitude to the sheet current density vector K_0 [Kochkin et al., 2015a]. The windows will modify the homogeneous current and magnetic field distribution (shown in figure 3.4) and act as a H-sensor. The voltage V is then measured by a coaxial cable connected to the inner and outer side of the fuselage.

The sensitivity of the sensor can be expressed as an effective flux-capturing area A, which is of the same order as the window's surface.

$$V = \mu_0 A \partial H_0 / \partial t \tag{3.2}$$

Where V is the voltage, μ_0 is the vacuum permeability constant and A is the order of the actual window surface. The measured and theoretical values are within 5% of each other.

The sensor is built in such a manner that the horizontal wire makes the sensor respond to the horizontal component of the current density K_0, and the vertical wire to the vertical component, but with a different sensitivity because of the elliptic shape of the window.

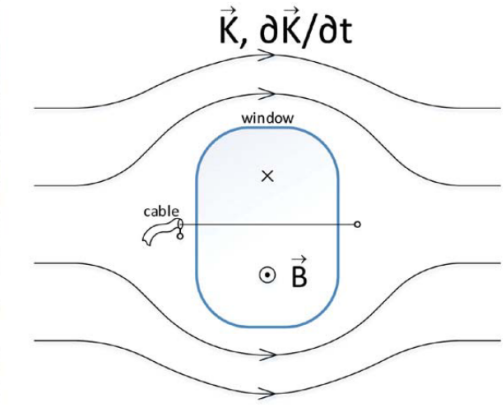

FIGURE 3.4: Illustration of the window sensor, with current density K through the aircraft fuselage and magnetic field penetration. Picture from [Kochkin et al., 2015a]

With an aircraft radius a of approximately three meters, the conversion of H-field to net homogeneous fuselage current

$$I = 2\pi a H_0 \tag{3.3}$$

results in 20 A per 1 Am^{-1} [Kochkin et al., 2015a]. The specifications for the instrument can be seen in table 3.3.

	H-field sensor
Sampling Rate	83.3 MS s^{-1}
Sampling Time	12 ns
Dynamic Range	96 dB over 100 Hz - 50 MHz
Time span (trigger mode)	1.2 s

TABLE 3.3: Characteristics for the H-field sensors.

ILDAS continuously monitors each signal from the H- and E- field detectors in separate sensor assembly electronics, which are synced to within one sample at 5 ms intervals [Kochkin et al., 2015a].

3.2.3 X-ray Detectors

The two separate X-ray detectors consist of $LaBr_3$(Ce) scintillators, with 38 mm diameter and 38 mm long crystals. The light is amplified by a Hamamatsu 10-stage photomultiplier, with dynode voltage dividers to enhance the maximum pulse frequency accepted [Kochkin et al., 2015a]. Because of the fuselage of the aircraft, the protective box and the scintillator housing, all x-rays with energies lower than 30 keV will be absorbed. The instrument characteristics are listed in table 3.4.

	X-ray energy sensor
Sampling Rate	100 MS s^{-1}
Sampling Time	10 ns
Time span (trigger mode)	1 s

TABLE 3.4: Characteristics for the X-ray sensors.

The X-ray detector is not used as a trigger because of the cosmic rays that cause a continuous background of high-energy radiation and charged particles. Three special software counters are used to obtain information on x-ray activity outside the 1 second triggered time span. These counters group up and determine the number of 10 ns sample periods where the x-ray signals exceed three pre-set levels over 15 ms consecutive periods [Kochkin et al., 2015a]. The x-ray detectors were calibrated after campaigns using the internal $LaBr_3$ radioactivity [Kochkin et al., 2017].

3.2.4 Data files

All the data recorded during the flight is stored in continuous data files (CDF). The time span and sampling times for all the instrument are listed in tables 3.2 through 3.4. Each instrument produces its own continuous data file with time and electric field, current or energy recordings.

The recorded data is continuously stored in a 1.2 second ring buffer memory. When a lightning strike occurs, the buffer will be automatically stopped, and data from 0.2 seconds before the trigger and 1 second after the trigger will be kept. In theory, if two lightning strikes occur in quick succession the data of the second flash will be stored at a secondary buffer. When the buffers are full, they will store all the data in 192 MB files per sensor [Zwemmer et al., 2009]. The data for each sensor consists of time and electric field, magnetic field or energy measurements. The polarity of the electric field sensor is set so that positive increases in value correspond to an electric field pointing towards the detector, while negative values correspond to an electric field pointing away from the aircraft.

In 2016 the CDF algorithm changed from counting the number of samples below certain voltage levels to operating as a spectrometer where it counts and stores the number of x-ray pulses per 15 ms in six individual energy channels for each detector [Kochkin et al., 2017]. Table 3.5 shows the x-ray energy channels for the two x-ray sensors.

	Ch. 1 [MeV]	Ch. 2 [MeV]	Ch. 3 [MeV]	Ch. 4 [MeV]	Ch. 5 [MeV]	Ch. 6 [MeV]
X14	0.06 - 0.17	0.17 - 0.29	0.29 - 0.40	0.40 - 5.70	5.70 - 17.10	$>$ 17.10
X15	0.10 - 0.21	0.21 - 0.31	0.31 - 0.42	0.42 - 10.40	10.40 - 20.80	$>$ 20.80

TABLE 3.5: X-ray energy channels used by the 2016 CDF algorithm.

Noise

All the detectors experience a small amount of electrical noise. The noise observed during analysis for the instruments are shown in table 3.6.

Instrument	Noise Span
E-field	~ 3 kV/m
H-field	~ 1.5 A/m
X14	~ 20 keV
X15	~ 80 keV

TABLE 3.6: Noise span of the different instruments. Note that all the H-field instruments share the same noise level.

The signal-to-noise ratio of the electric field instruments is negligible, as the measurements are often of fast changing, strong electric fields. The signal-to-noise ratio in the current measurements are more severe. The two different X-ray detectors have different noise levels. The X14 detector has a noise span of 20 keV, while the X15 detector has a span of 80 keV. This can make it hard to distinguish relative low energy photons from noise. X15 was not operational during the 2014 campaign. Figures of the noise levels of each instrument can be seen in appendix A.

3.3 Lightning location data

The data of the lightning locations on 15.01.2016 were collected from the Lightning Incident Archive Search (LIAS), which is a lighting location network in Australia. The data file included date, time, longitude, latitude, amplitude and distance measurements of flashes observed in proximity to an area around -16.5702 latitude, 127.48919 longitude (north in the Western Australia territory).

Chapter 4

Methodology

This chapter will be used to outline the methods needed to answer the thesis question: When during a lighting flash do we observe x-rays, and is the production of x-rays related to changes in the current or local electric fields measured on the aircraft? Are x-rays observed without associated aircraft-initiated lightning flashes?
The data used in this thesis is gathered from the ILDAS instruments on board an aircraft. The data consist of measurements on local electric field, current and x-ray energy.

4.1 ILDAS Data

Pavlo Kochkin's application to read the continuous data files was used, before exporting the needed data to Root TTrees and later MATLAB files. Python, MATLAB and CERN Root was used as tools to view, sort, analyse and create the representations of the data presented in this thesis.

All local electric fields,current and x-ray energy measurements in this paper are presented without smoothing of the measurements. In the few cases where smoothing of data is applied, the reader will be made aware.

4.1.1 Defining lightning initiation classes

Electric field and current measurements from aircraft initiated lightning flashes were studied to determine the attachment points of the bidirectional leaders. This was done by using data from the aircraft-initiated lighting strikes. The first step was to identify the start of the positive and negative leaders by manually examining the local electric fields, and finding the signature rises and steep drops in the local electric fields, as shown in figures 2.24 and 2.28. The positive and negative leader initiation locations were found by analysing the polarities and amplitudes of the measured currents in the aircraft, at the time of negative leader initiation (see chapter 2.6.1). A similar method, using the current polarities and amplitudes were used by Zwemmer et. al. [2009] to find the attachment points of lighting leaders to aircraft.

The aircraft fuselage can be viewed as a long uniform tube for the purposes of calculating the current flow. Therefore the two current measurements at the nose (H02 and H03), body (H09 and H07) and tail (H08 and H13) were averaged, to make a general overview of the current flow at each section along the tube. The wing sensors were not added together. The resulting 5 measurements were then used to make a plot of the currents flowing through the aircraft. The plots for each lightning flash were then compared to each other and categorised based on similarities in current direction and amplitudes. All current measurements were done right after the

launch of the negative leaders. As shown in figure 4.1, there are no usable current measurements before the launch of the negative leader. This is probably because the current is constant or rising too slowly for the detector to measure it, during the positive leader initiation. The two small current pulses seen during the positive leader initiation are though to be caused by negative corona discharges.

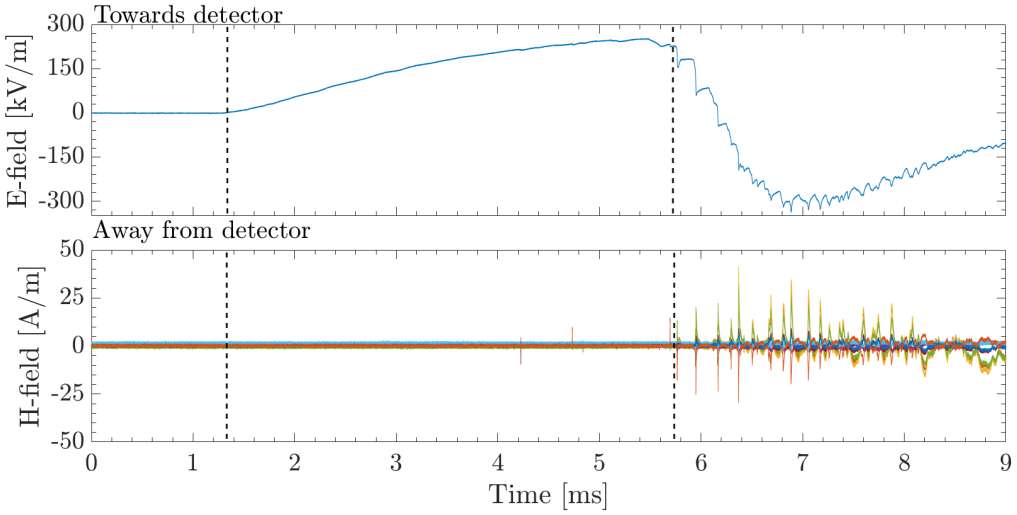

FIGURE 4.1: Local electric field and current measurements observed during the initiation of positive and negative leader initiations, in flash 304AE7E5 on 24.04.2014. The dashed lines marks the start of the positive and negative leaders.

After finding the current classes, the maximum, minimum and average values for each class were found. Error-bars were added to the average values, using the standard deviation of the whole class for each location. The attachment points for the classes were then determined from the current measurements, as there are no cameras on the aircraft that could confirm the attachment locations. The attachment point of the negative leader is thought to be where the majority of electrons exit the aircraft, i.e. where the largest current enters the aircraft. The positive leader's attachment point is thought to be where the majority of electrons enter the aircraft, i.e. where the largest current exits the aircraft. The results from this study can be found in chapter 5.2.

4.1.2 Methods used for analysis of nanosecond pulses of x-rays

The nanosecond long pulses of energy observed during the stepping of negative leaders were found by plotting and viewing the data from the time window between the negative leader launching, and the positive leader gaining speed and starting to branch (phase B in figure 2.24). The stepping of the negative leader can be identified as drops in the electric field over a few micro seconds. During this time window the local electric field, current and x-ray measurements were plotted for each observed leader step (see chapter 5.3.1). All energy measurements were compared to the background, before the data for every individual step containing such an energy pulse were saved to individual data files, for easier comparison.

The local electric field changes in magnitudes and time were then compared to the photon energies measured. The current was also compared to both the changes in the local electric field and the measured energies. The energies of the photons were plotted in 15 keV bin size, to best differentiate the measured energies. The results are presented in chapter 5.3.1.

4.1.3 Methods used for analysis of microsecond long bursts of x-rays

Microsecond long bursts of x-rays were found during recoil events in the lightning flash. The recoils, like the negative leader steps, shows microsecond fast changes in the local electric field. Recoils are observed during the return strokes and dart leaders of a lighting flash. The recoils were then examined for time correlating x-ray bursts. Local electric field change, change duration, currents, photon burst energies and photon burst durations were determined for each recoil event correlating with observed radiation. The data was saved to individual files just as for the nanosecond pulses of x-rays.

The local electric field changes in magnitude and time, as well as the current amplitudes were compared to the photon's energies and burst durations. The minimum number of photons in each burst and all the photon energies are presented in chapter 5.3.2. The minimum photon counts were found by counting the amount of pulses observed during the burst. The x-ray detectors have a sampling time of 10 ns, meaning photons arriving simultaneously can not be distinguished. All counts of photons in bursts should be taken as approximates, due to the limitations of the measurements. The average single pulse energies and average burst energies were determined for the different burst counts.

Figure 4.2 shows a burst of atleast 5 photons, observed during flash 203C8647 on 24.04.2014. Five pulses are observed, where pulse 1 and 2 are 60 ns apart, and pulse 3 and 4 are 50 ns apart. The red lines symbolise the defined start time and end time of the burst. The duration of the burst is approximately 0.77 μs.

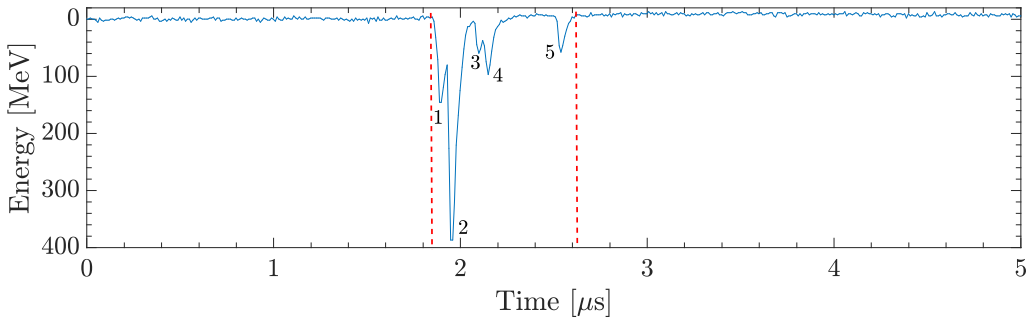

FIGURE 4.2: X-ray counts during a burst of atleast 5 photons. Observed during flash 203C8647 on 24.04.2014. The red lines symbolise the defined start and end of the burst.

It is possible that some of the observed photon pulses are in fact multiple photons with lower energies. There is no way of distinguishing multiple photons arriving simultaneously, but if there is a small time gap between the arrivals, a widening of the energy pulse will occur. One event showing such a widening is shown in figure 5.19 in chapter 5.3.2.

4.1.4 Yearly Background

There is no easy way of isolating the cosmic background during the observations. A yearly average background count was found by averaging the observed background counts with energies over 100 keV for each year. This energy limit was chosen so that most of the cosmic background would be included. Table 4.1 shows the average yearly background counts, with the corresponding standard deviation as a source of error.

Year	Average background counts [s^{-1}]	Flight altitude
2014	37 ± 6	4 - 5 km
2015	45 ± 7	4 - 5 km
2016	79 ± 9	9 - 11 km

TABLE 4.1: Average yearly background counts per second, with energies over 100 keV and corresponding errors.

The yearly background count averages were then used to find the chance of mistaking a measured count for a cosmic background count. Table 4.2 shows the chance of observing a background count in a given duration.

Time window	2014 [%]	2015 [%]	2016 [%]
2 ns	$7.4 \cdot 10^{-6}$	$9.0 \cdot 10^{-6}$	$1.58 \cdot 10^{-5}$
1 μs	0.0037	0.0045	0.0079
10 μs	0.037	0.045	0.079
100 μs	0.37	0.45	0.79

TABLE 4.2: The chances of background counts to be observed in a given time window for each year of the ILDAS campaign.

As seen, there is a very small chance of a background count to be wrongfully detected as a measured count in association with a given event. This is mostly due to the small time scales of the radiation producing events. In reality the chances are even smaller, as all measured counts over 100 keV are not cosmic background.

4.1.5 Methods used for analysing gamma ray glows

The updated CDF algorithm was used to find count rate increases for the different days of the aircraft campaigns over Australia. These count rate increases were then analysed, to find if the observations showed significant count rates over background. The duration of each count rate increase was determined, before the gathering the measured counts in 15 ms bins for the same duration. These measurements were then used to decide the average counts per second. Average background counts per second was then found by measuring the counts over the same duration as the observed peak, at approximately 1 minute before the count rate increases were observed. Figure 4.3 shows measurements of x-ray counts binned to 15 ms, with black dotted lines symbolising the duration of background and count rate increase used to find average counts per second. The average count values were then used to decide the significance of the observations.

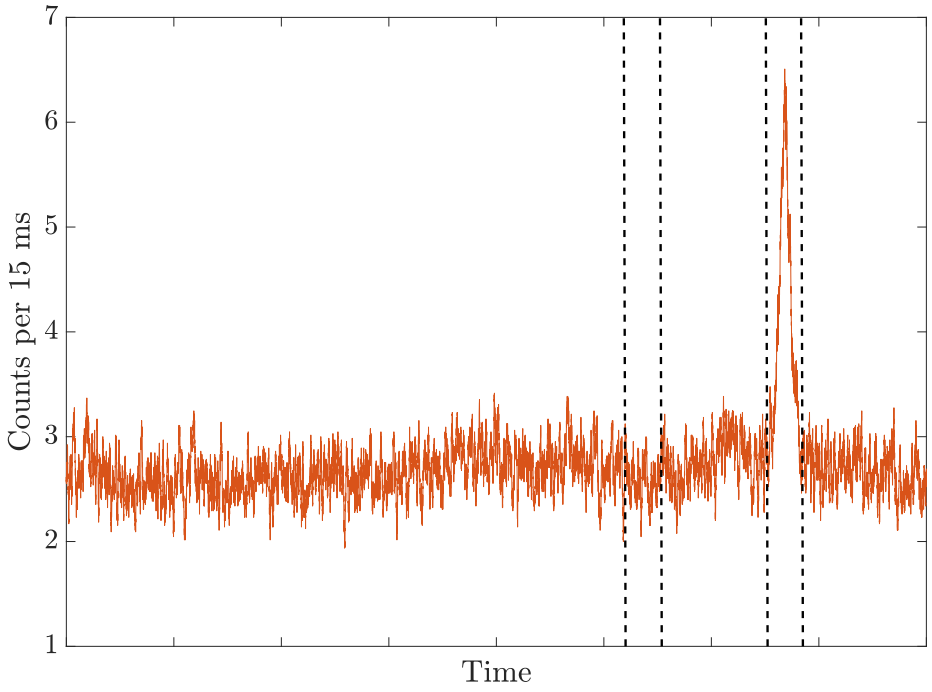

FIGURE 4.3: X-ray counts binned to 15 ms. The dotted black lines symbolise the background area, and the glow area used in calculations of background.

The lighting activity around the glow terminating flash was determined by plotting the flash counts for a given time and distance interval from the glow terminating flash. One of the plots can be seen in figure 5.23 in chapter 5.3.3.

4.1.6 Methods used for analysis of positron annihilation signatures

The first step in analysing the positron annihilation signatures was to find the total energy counts registered for each individual aircraft-triggered lightning flash on 14.01.2016. This was done by locating all peaks over 80 keV during one second of lightning flash data (always from -0.2 s to 0.8 s in the x-ray data sets) for both X14 and X15. 80 keV was used as the lower cut off value to reduce noise.

The new CDF algorithm was then used to plot the local electric field and x-ray counts for the duration outside of the trigger time. The measurements were used to find a correlation between count rate increases and pulses in the local electric fields. The CDF algorithm plots the minimum and maximum values in 18 ms bins, and the x-ray counts in 15 ms bins. These were used to find correlation between count rate increase and pulses in the local electric fields. The background subtracted counts for each trigger was then found, by measuring background in a similar manner as for the glows, but without 15 ms binning of the x-ray counts. The energy spectra of the lightning flashes were then plotted, with measured energies over 80 keV from both x-ray detectors.

Chapter 5

Results and discussion

This chapter will present the results related to the thesis question. The chapter will start by giving an example of the measured currents and local electric fields observed during the initiation of an aircraft-initiated lighting flash in section 5.1. Similarities in the measured current amplitudes and polarities during leader initiations will be investigated in section 5.2.

Observations of nanosecond long pulses and microsecond long bursts of x-rays associated with aircraft-triggered lightning flashes will be reported in sections 5.3.1 and 5.3.2. A correlation between the observed energies and the changes in local electric field and current magnitudes will be investigated.

Observations of gamma-ray glows will be reported in section 5.3.3, and an analysis of events showing positron annihilation signatures will be presented in section 5.3.4.

5.1 Example of bidirectional leader initiation on aircraft

The first step of analysing and grouping the lightning leader initiations was to get an understanding of the local electric field and the associated current measurements. As seen in chapter 2.6.1 the bidirectional leader initiation can be divided into three phases based on the local electric field measurements. A total overview of the three phases can be seen in figure 5.1, which shows the local electric field of lightning flash 3051B4BA observed on 02.05.2014.

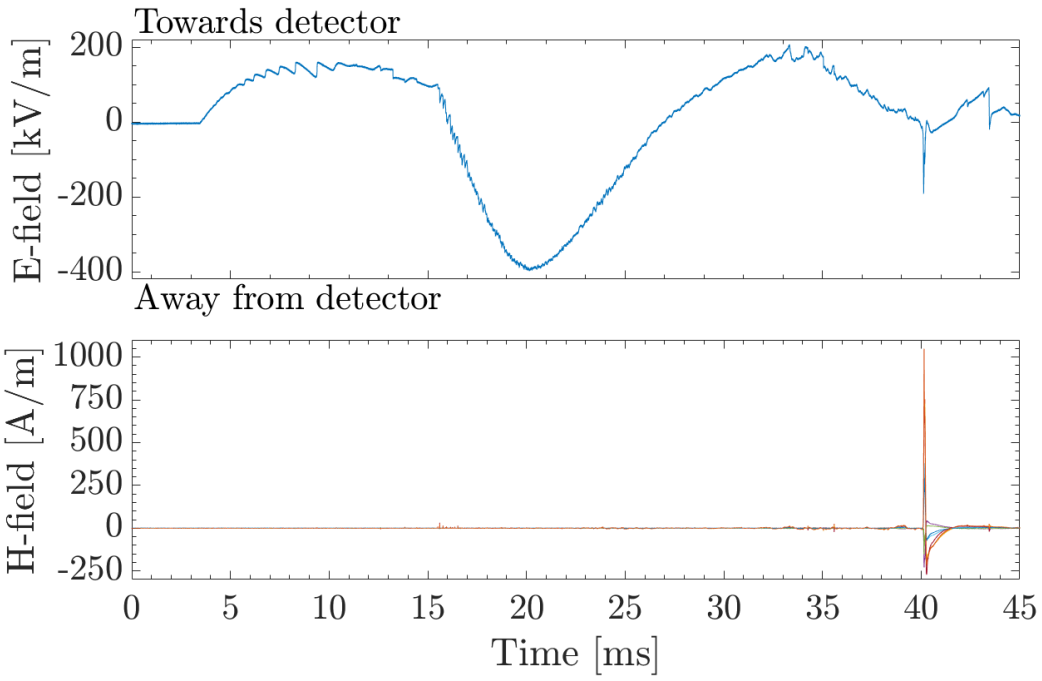

FIGURE 5.1: Overview of the three phases of an aircraft-triggered lightning. The top graph shows the measured local electric field, the bottom graph is the magnetic field (used to find current).

The positive leader initiation, called phase A (from $\sim$ 4 ms to $\sim$ 15 ms) can be seen in figure 5.2. Here the positive leader is launched and the local electric field will point towards the detector. Few current fluctuations are observed during this period, except the pulses corresponding to the small and sudden changes in the measured local electric field, most likely caused by negative corona discharges. These negative corona discharges form at the sharp extremities of the aircraft, as the aircraft gets polarised in the presence of the positive leader.

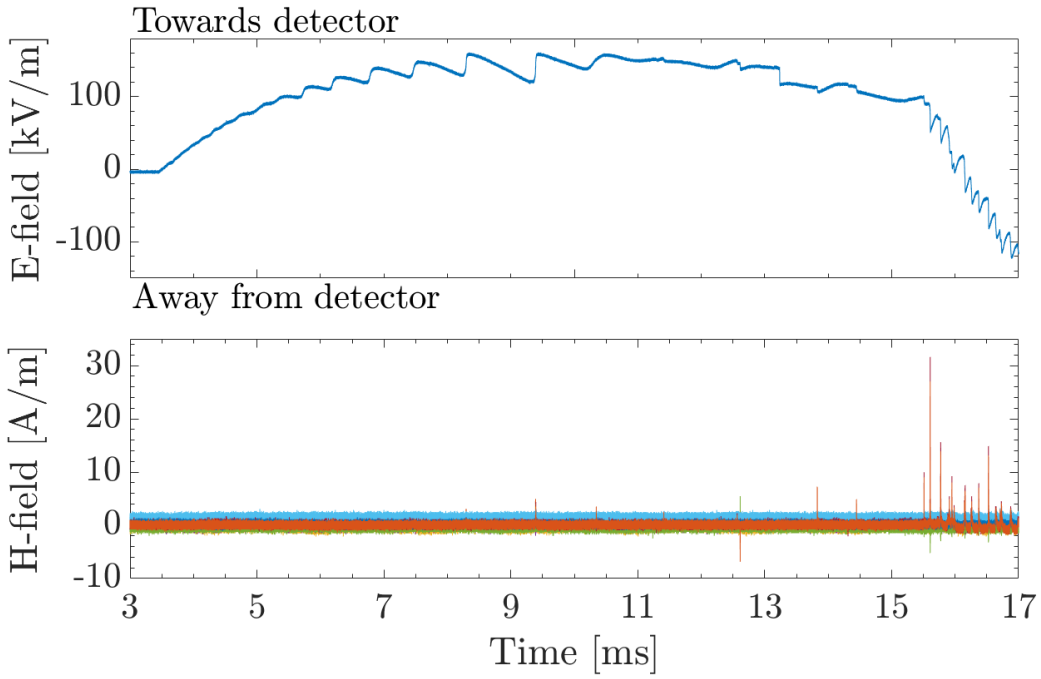

FIGURE 5.2: Local electric field and current during Phase A: The Positive leader initiation and propagation.

Phase B (from $\sim$ 15 ms to $\sim$ 21 ms) is defined as when the negative leader initiates and the local electric field points away from the detector, can be seen in figure 5.3. As seen, thehe negative leader steps are associated with pulses in the current measurements.

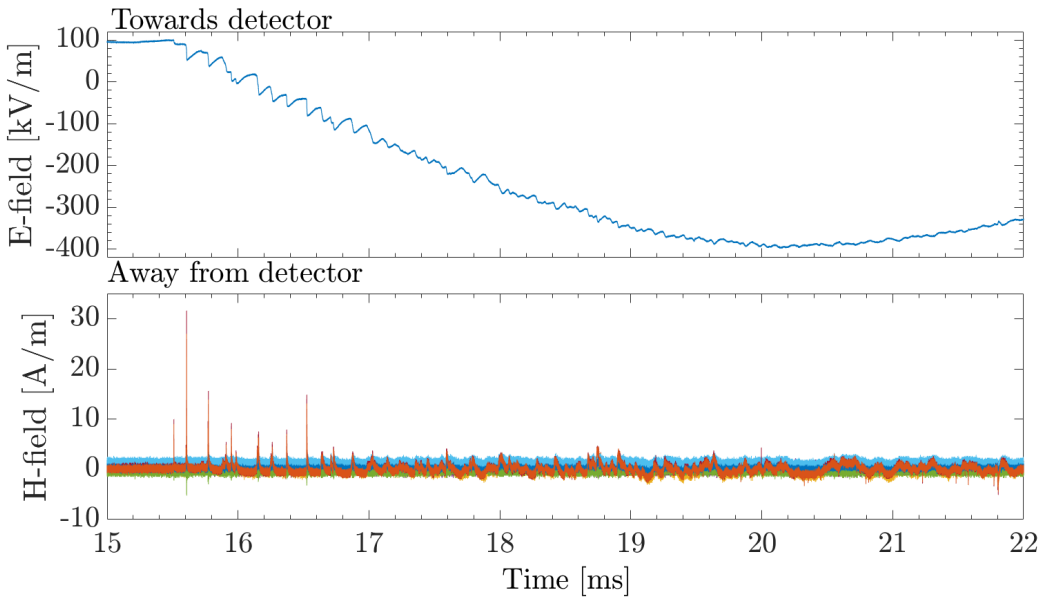

FIGURE 5.3: Local electric field and current during Phase B: The Negative leader initiation and propagation.

During phase C (from $\sim$ 21 ms to $\sim$ 33 ms) the positive leader gains speed and

starts branching. This makes the local electric field point towards the detector again, before the electric field stabilizes. During this period sharp drops in the local electric field are seen, which are closely associated with large pulses in the current.

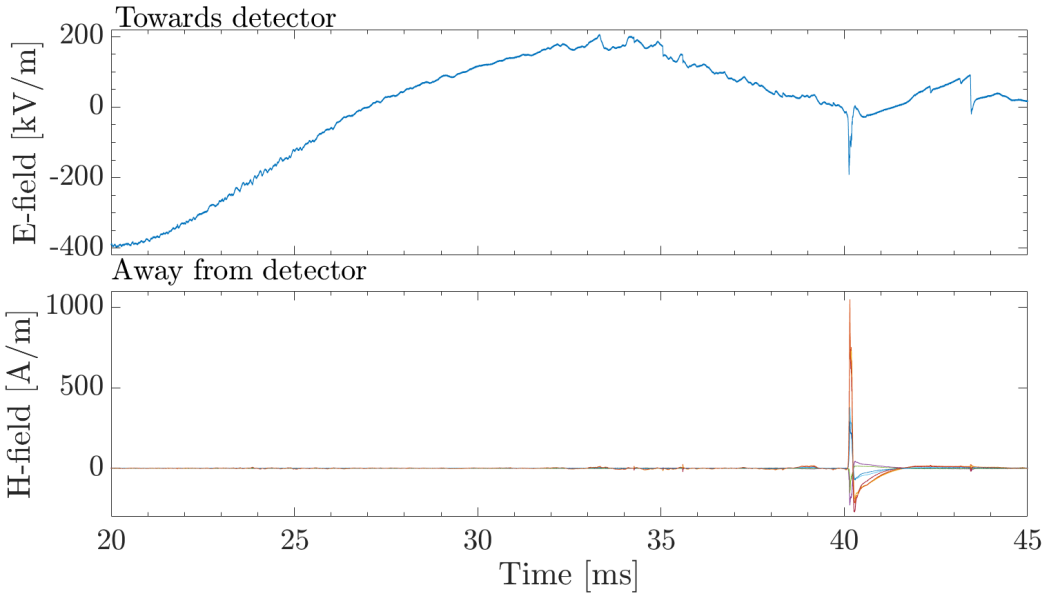

FIGURE 5.4: Local electric field and current measurements of phase C: Where the positive leader gains speed and starts branching.

5.2 Categorization of bidirectional leader initiations

The current going through the aircraft during the bidirectional leader initiation was analysed by comparing current magnitudes and polarities. The initiations are categorized so that positive H-field values represent where the current exits the aircraft, and negative values where current enters the aircraft. The only exception to this is the body, where positive values represent currents flowing towards the nose, and negative values represent current flowing towards the tail. The classes were named after the main entry points of the current. The initiation location of negative leaders is where the current enters the aircraft, while the initiation location of the positive leaders is where the current exits the aircraft. Due to limitations of the ILDAS, the amount of incoming current is not equal to the outgoing current. The current measurements should not be treated as absolute values, but as indications of the magnitude differences in the observed currents.

5.2.1 Results for positive bidirectional leader initiations

From the analysis of the bidirectional leaders starting with positive leaders, six different current patterns were found. All lighting flashes correlating to one of these patterns were grouped together in classes. These classes are illustrated with a plot of the average current vectors for the class and a plot of the maximum, average and minimum measured magnetic fields for each class. The conversion from current sheet density to current is described in chapter 3.2.2. The individual lightning flashes belonging to the classes can be found in appendix B.1.

Nose

In the Nose class the current enters through the nose and exits through the tail, with some current also coming in from the right wing.

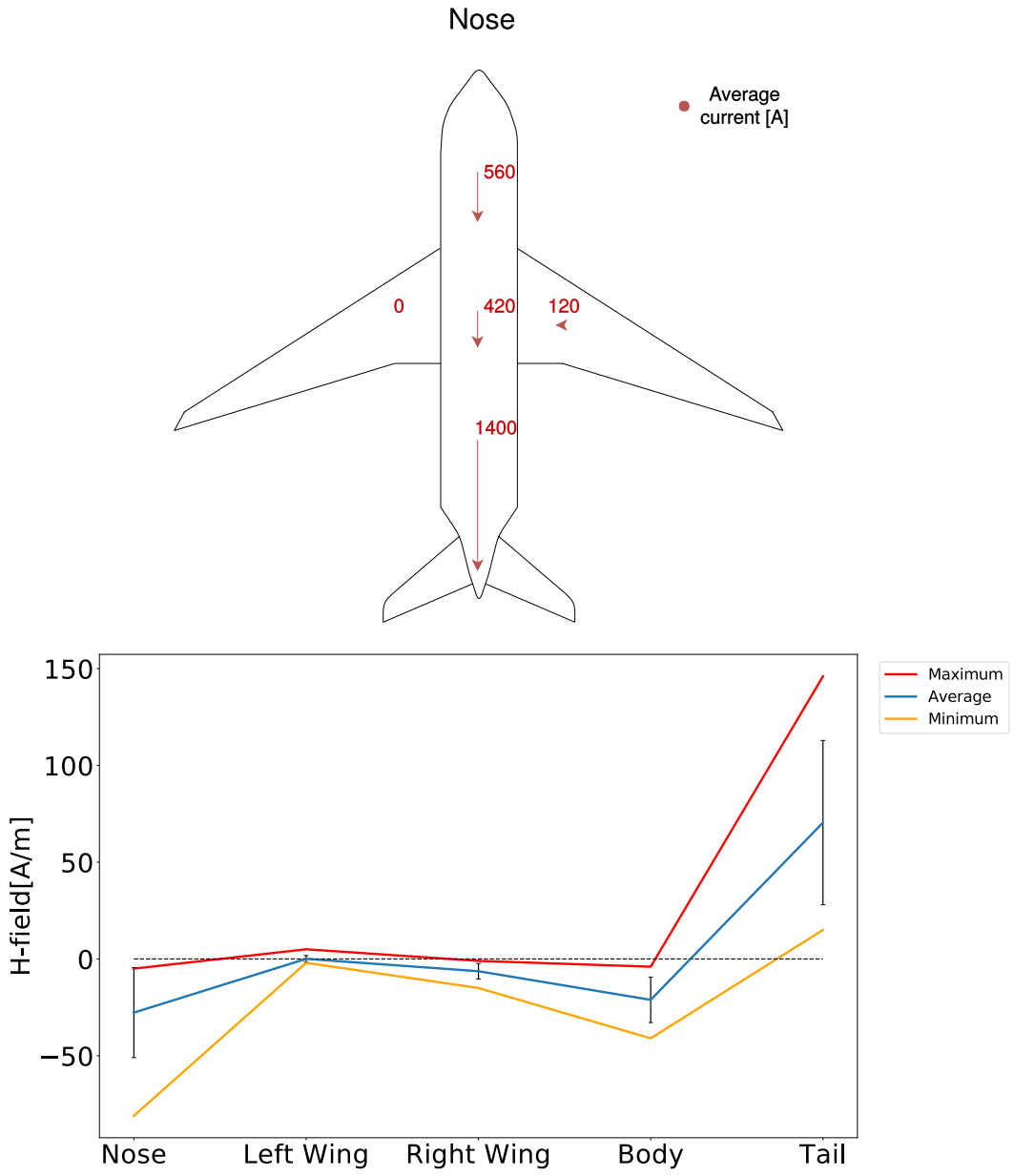

FIGURE 5.5: Nose: positive leader initiation from the tail, negative leader from the nose.

Nose + Tail

In the Nose + Tail classes the current enter the aircraft at the nose and tail, and exits at the right wing.

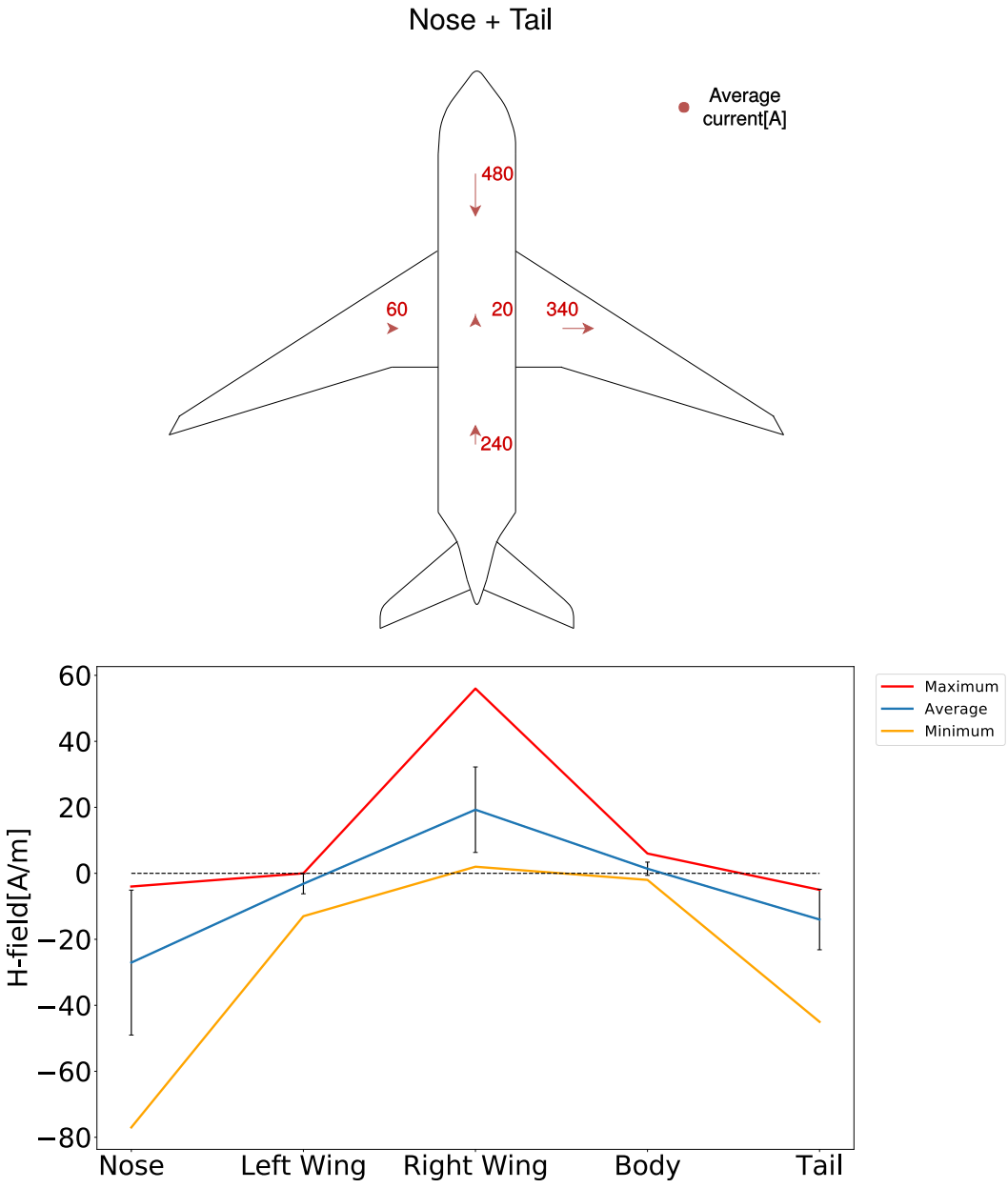

FIGURE 5.6: Nose + Tail: the maximum, minimum and average values measured for the class with error bars added to the average.

Tail + Nose

In the Tail + Nose class the current enters the aircraft at the tail, nose and right wing, and exits through the left wing.

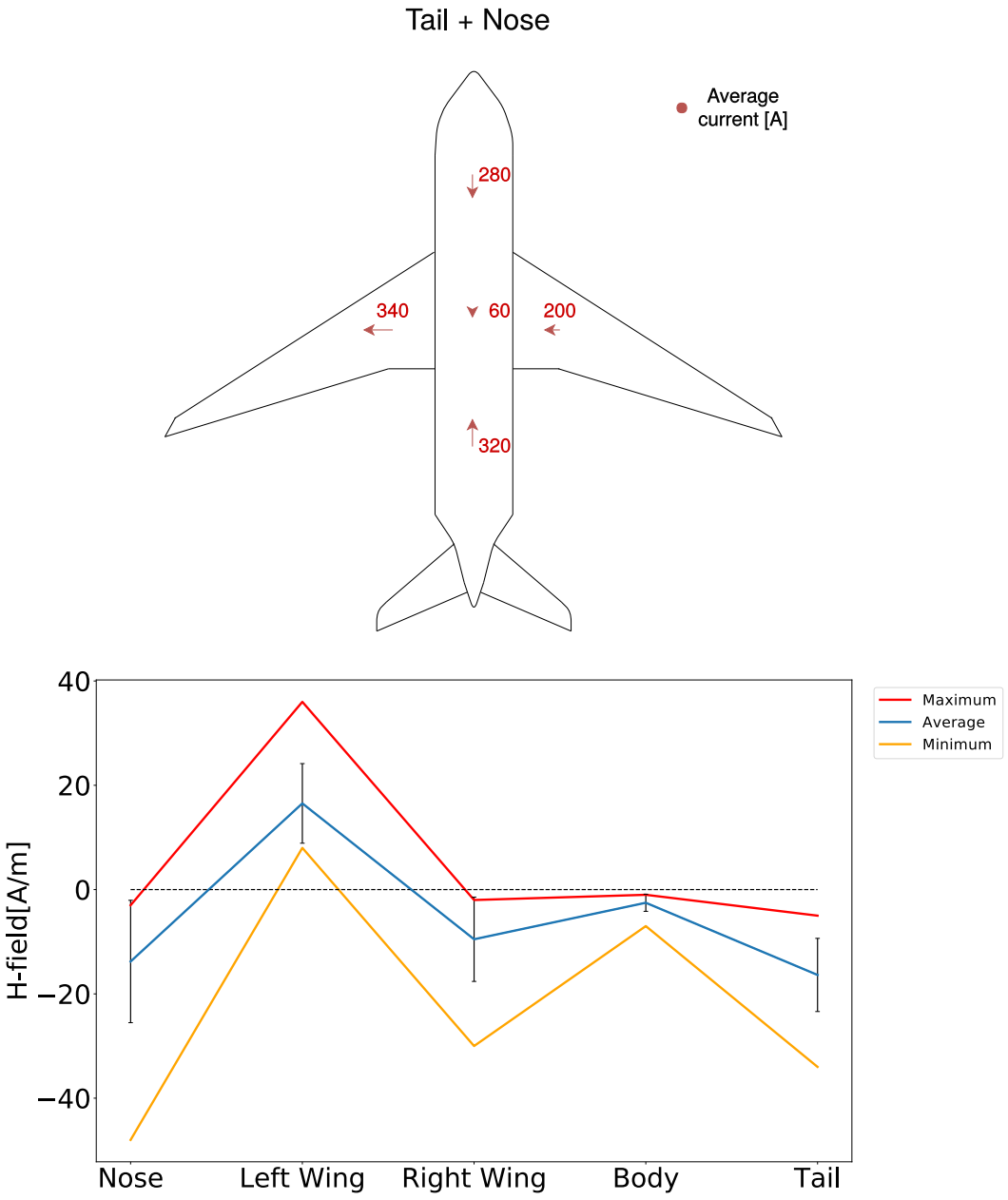

FIGURE 5.7: Tail + Nose: the maximum, minimum and average values measured for the class with error bars added to the average.

Tail + L.wing + Nose

In this class most of the current enters the aircraft at the tail, but also from the left wing and the nose. The current exits at the right wing.

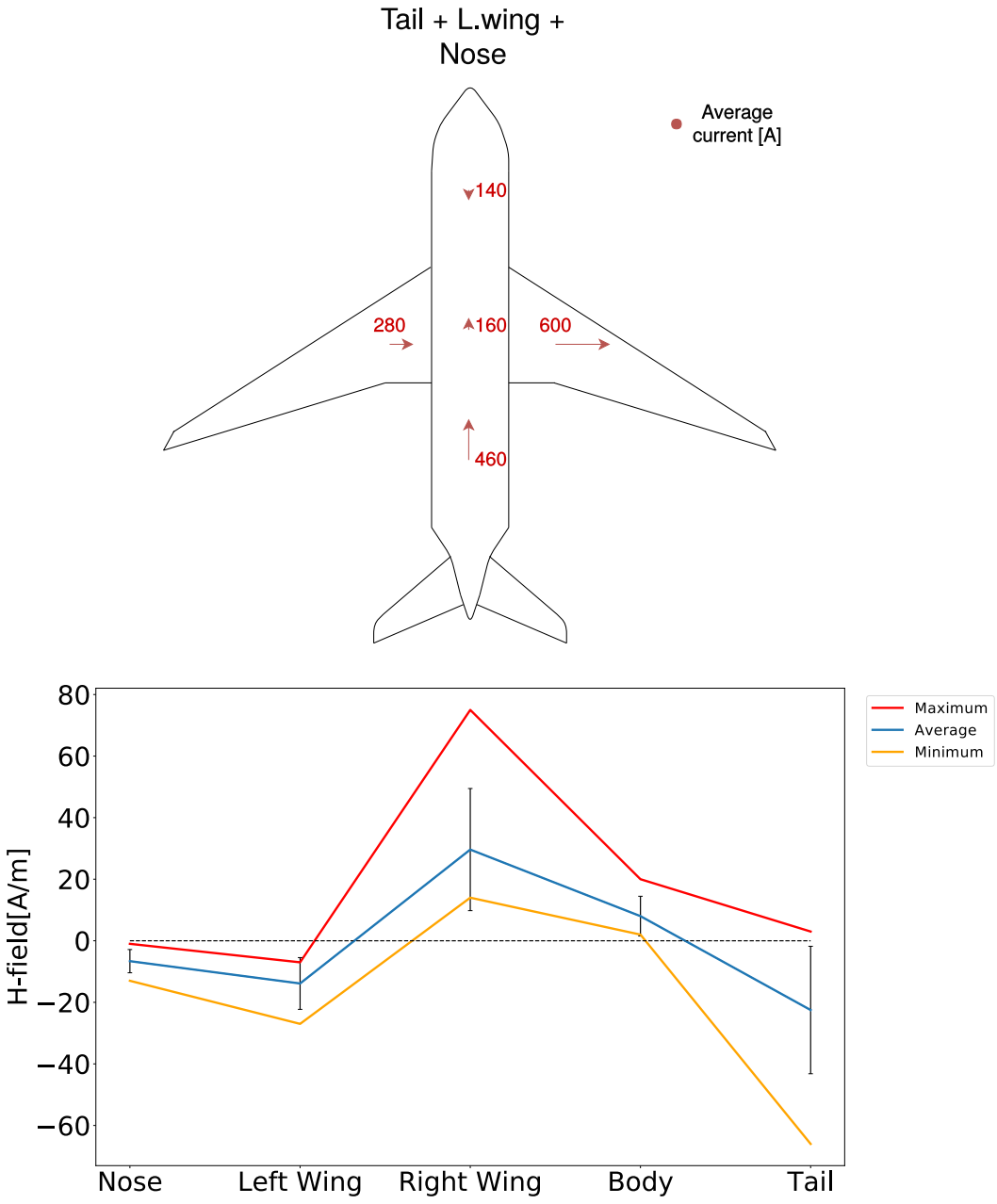

FIGURE 5.8: Tail + Left Wing + Nose: the maximum, minimum and average values measured for the class with error bars added to the average.

Tail + L.wing

For the Tail + Left wing class, the current enters the aircraft at the tail and the left wing, and exits at the right wing and nose.

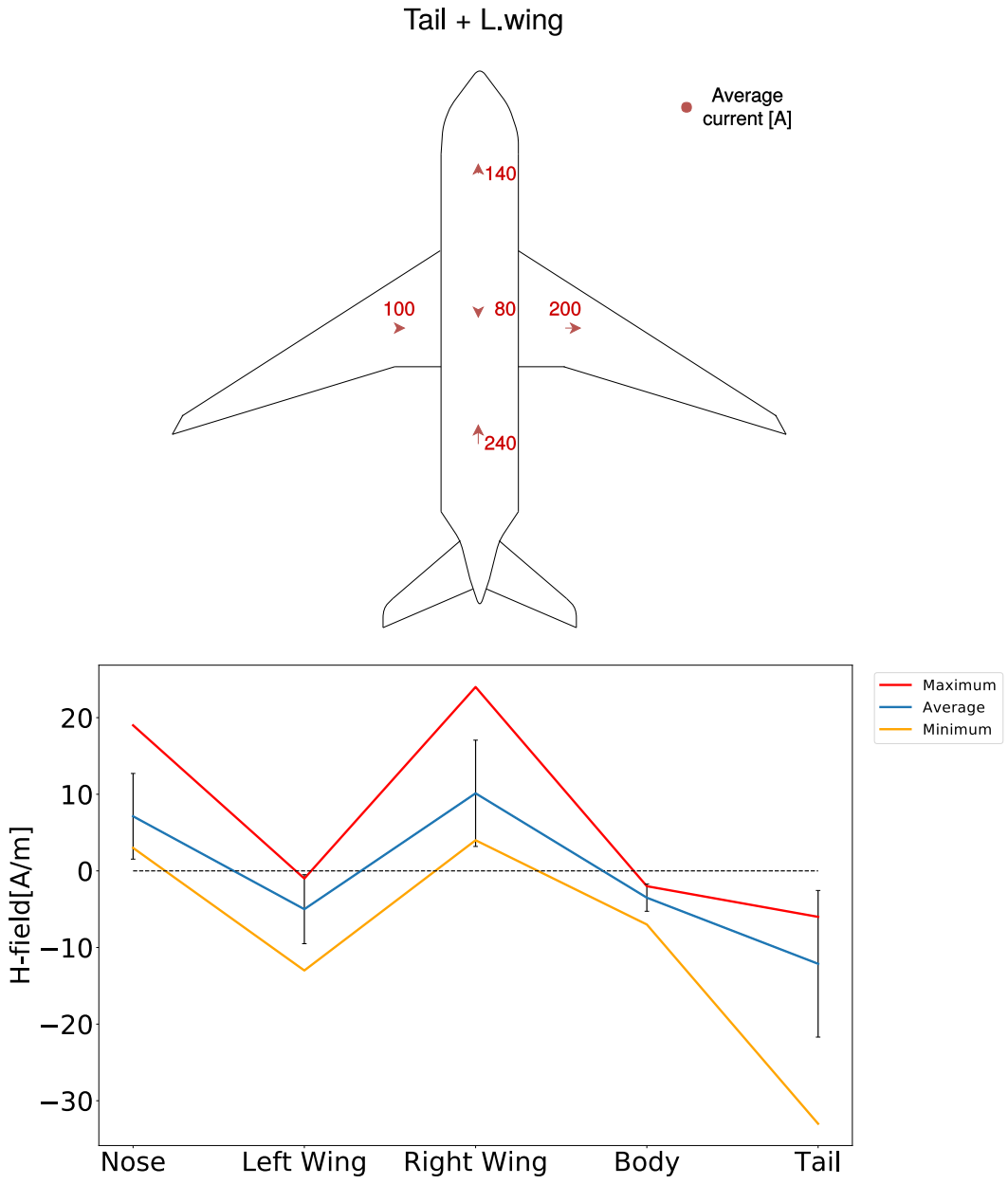

FIGURE 5.9: Tail + Left Wing: the maximum, minimum and average values measured for the class with error bars added to the average.

Tail + R.wing

For the Tail + Right Wing class the current enters the aircraft mainly at the tail, but also from the right wing. The current exits the aircraft at the left wing and nose.

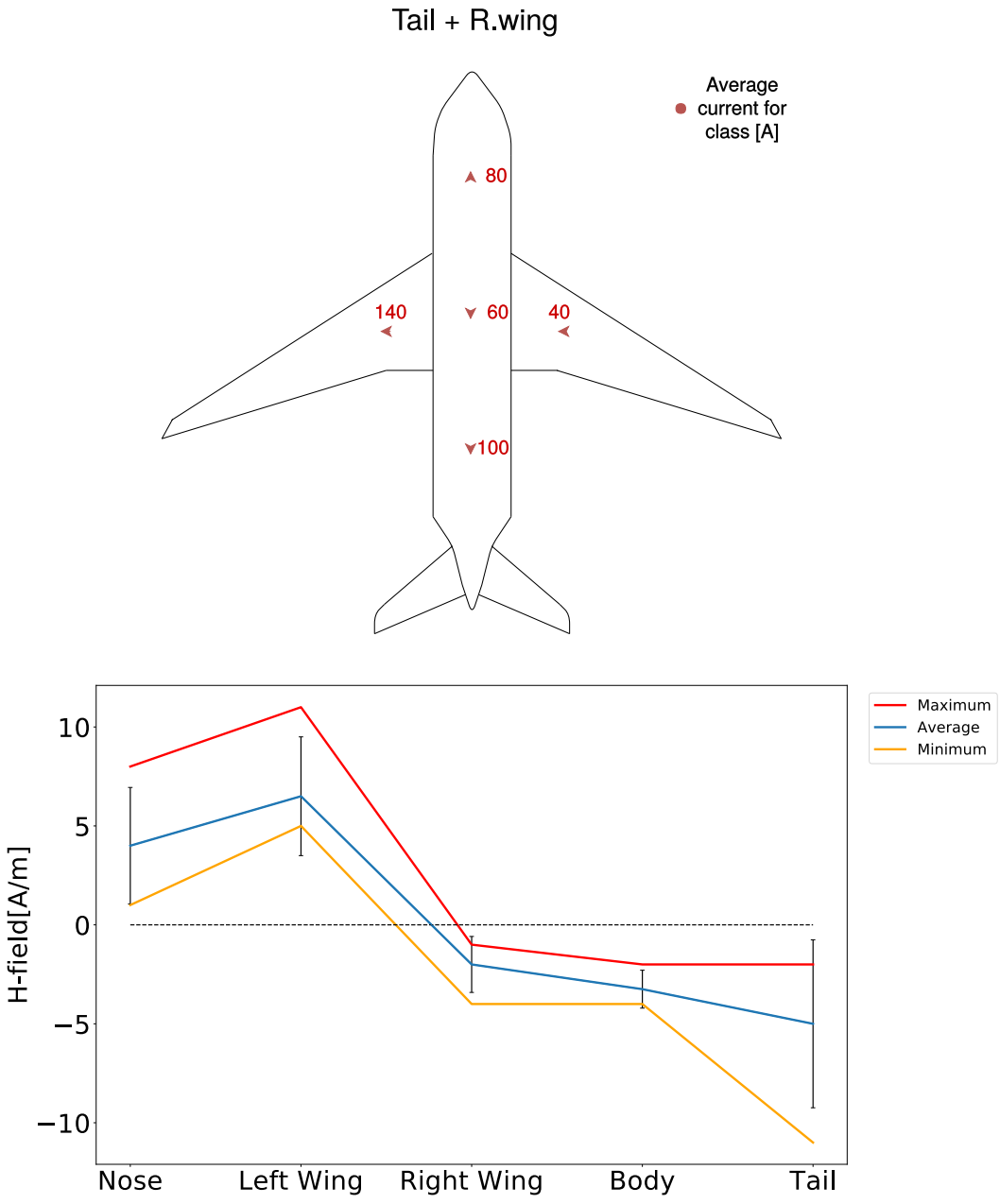

FIGURE 5.10: Tail + Right Wing: the maximum, minimum and average values measured for the class with error bars added to the average.

Table 5.1 shows the distribution of initiations for the six classes.

Category	Initiations	%
Nose	18	24.0
Nose + Tail	18	24.0
Tail + Nose	19	25.3
Tail + L.wing	8	10.6
Tail + L.wing + Nose	8	10.6
Tail + R.wing	4	5.3
	75	

TABLE 5.1: Initiations per class. The first location is the main current entry point, the second name the second largest entry point etc.

87 % of the flashes belong to this initiation type, where the currents are entering from the tail of the aircraft. A possible reason why none of the observed events have currents entering mainly from the wings might be the static discharges mounted at the tips of the wings. These dischargers dump charge out of the aircraft as corona discharges, at certain intervals, making it harder to accumulate charge in those areas. Another reason is that in most cases the aircraft is flying towards or away from the thunderclouds, which polarises the nose and tail areas.

5.2.2 Results for bidirectional leaders preceded by negative corona

Two classes were found from analysis of the bidirectional leaders preceded by negative corona. These classes are illustrated with a plot of the average current vectors for the class and a plot of the maximum, average and minimum measured magnetic fields for each class.

Tail

The Tail class has the current entering the aircraft at the tail and wings, and exiting at the nose. This is the only real scenario found, where a negative corona precedes the initiation of the positive leader in an aircraft-triggered lightning flash.

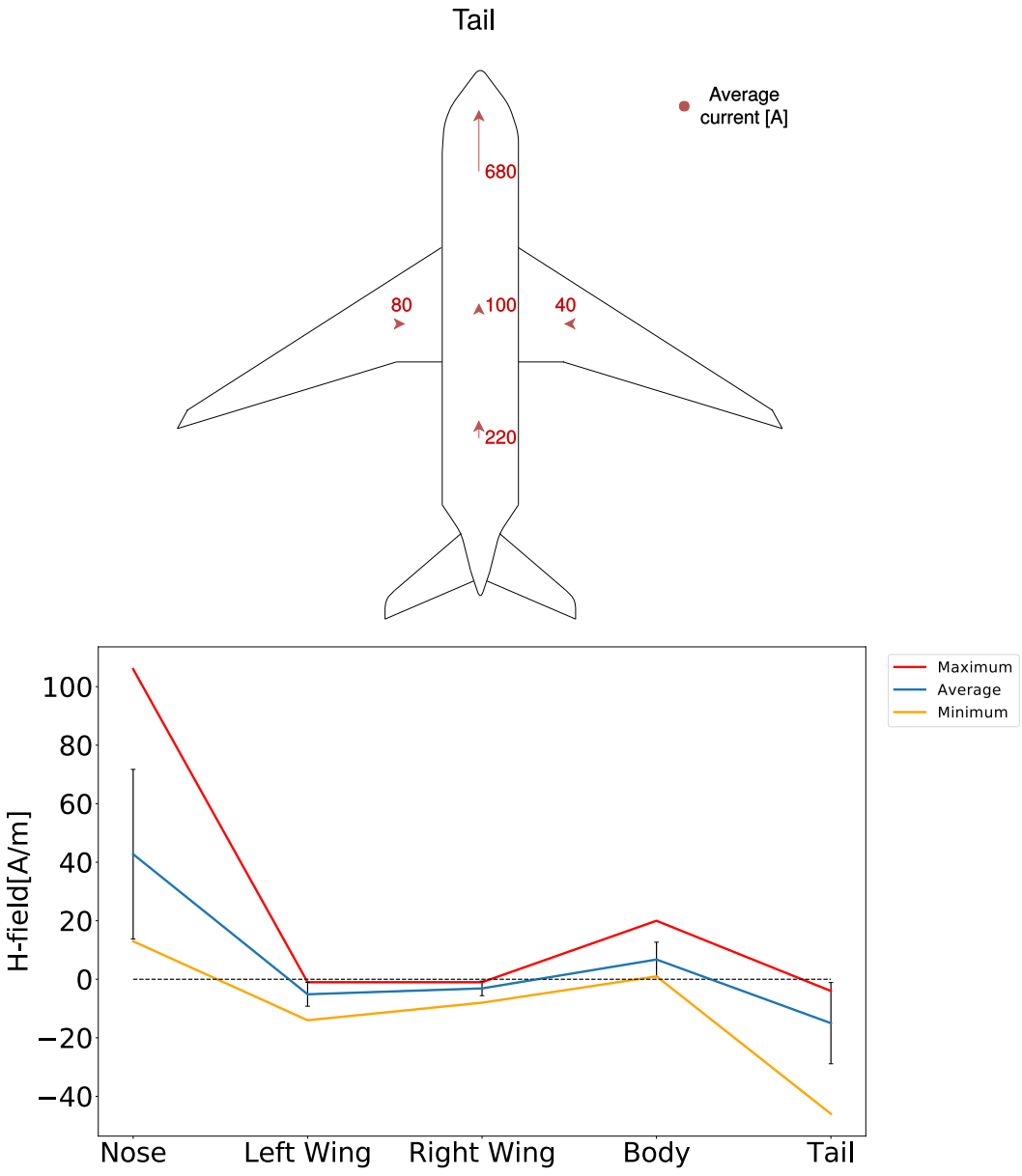

FIGURE 5.11: Tail: the maximum, minimum and average values measured for the class with error bars added to the average.

Static discharges

The Static discharges class has current entering at all extremities, i.e. electrons are exiting at all aircraft extremities. These discharges are thought to never evolve into a lightning flash, and are probably caused by the static discharges on the aircraft.

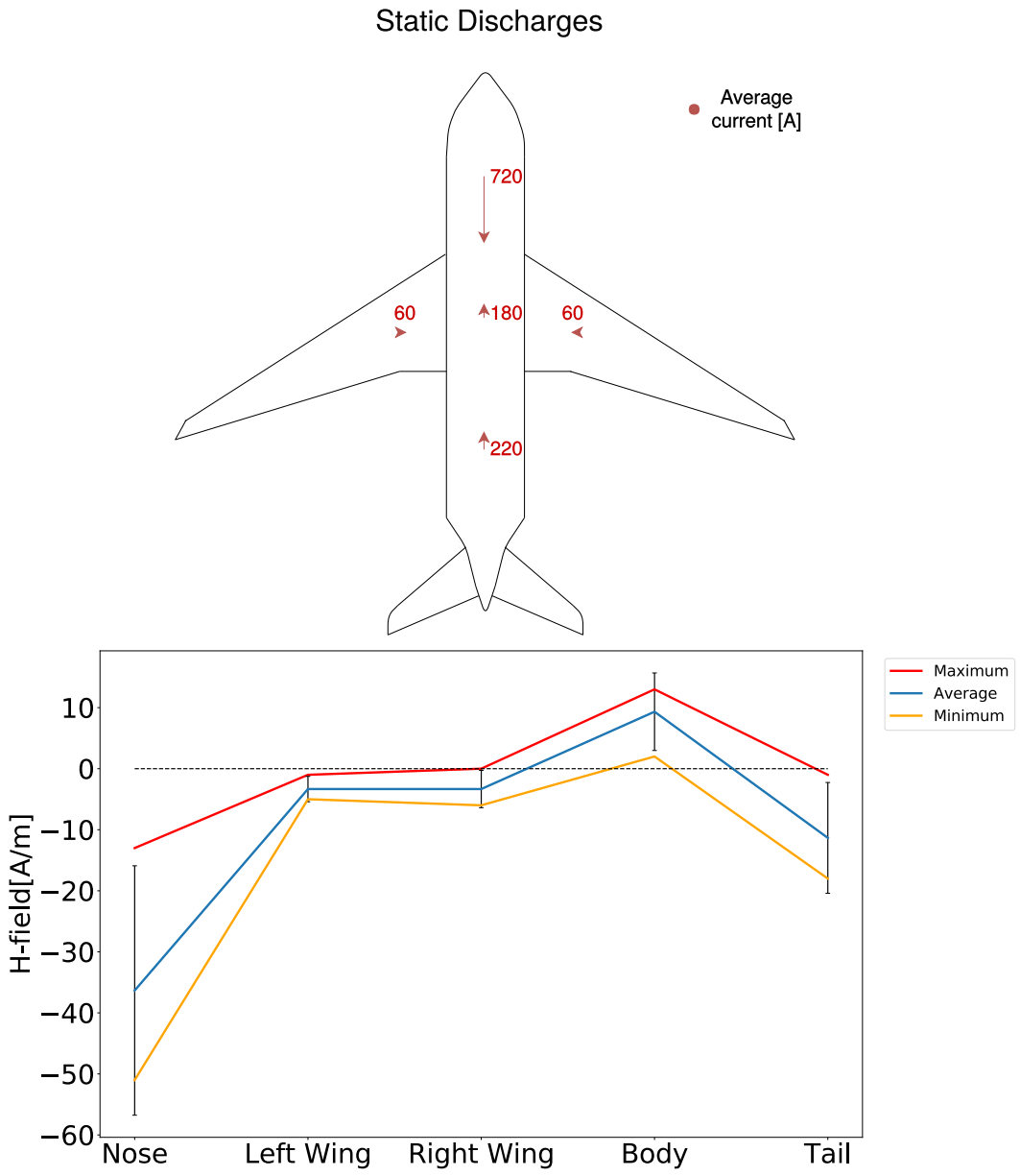

FIGURE 5.12: Static discharges: the maximum, minimum and average values measured for the class with error bars added to the average.

Table 5.2 shows the distribution of the initiations preceded by negative corona.

Class	Initiations	%
Tail	8	72.7
Static Discharges	3	27.3
	11	

TABLE 5.2: Initiations per class. The first location is the main current entry point.

12.8 % of flashes belong to this initiation type. The reason there are few initiations of this type is that the electric field needed for negative streamer propagation is approximately two times larger than the electric field needed for positive streamer propagation. The aircraft also needs to be pre-charged to initiate a negative corona.

5.2.3 Summary of the two observed initiation groups

Table 5.3 shows the total flash distribution by campaign year for all defined current classes. As seen, there is a clear difference in current classes between the 2014-2015 campaigns and the 2016 campaign. The reason for this might be the different aircraft used during these two periods, or the change in flight altitude.

Class	2014	2015	2016
Nose	13	5	0
Nose + Tail	14	3	1
Tail + Nose	15	4	0
Tail + Left Wing	0	0	8
Tail + Left Wing + Nose	5	3	0
Tail + Right Wing	0	0	4
Tail	6	2	0
Static discharges	0	0	3
	53	17	16

TABLE 5.3: Yearly campaign contribution to each current class.

The only observed category for bidirectional leader initiations, preceded by negative corona, that evolve to a lightning flash, is the Tail class. The Tail class was only observed in the campaigns over Europe. The static discharges were only observed in the Australian campaign. As the aircraft-initiated flashes observed over Australia only constitute ~ 19.8 % of the observations, not observing certain initiation patterns does not necessarily indicate the absence of said patterns. The difference between the two aircraft types and geographical areas indicates a correlation between the current pattern and aircraft type and/or flight altitudes.

The majority of all measured flashes have currents entering from the tail of the aircraft. A possible explanation why none of the observed events have currents entering mainly at the wings might be because of the static discharges mounted at the tips of the wings. These dischargers will dump charge out of the aircraft at certain intervals, making it harder to accumulate charge at the wings.

The initiation classes were then studied, to see if there were any connection between the current classes, initiation types and production of x-rays. Analysis of the lightning initiations showed no x-ray production during the initiation of positive leaders. The first observed x-ray producing event were found just after the negative leader initiated and started to step.

5.3 Observations of X-rays

As mentioned at the beginning of this chapter, this section will provide the results for the observed events with correlating x-rays.

Section 5.3.1 will present the findings of nanosecond long x-ray pulses associated with stepping of negative leaders. Microsecond bursts of x-rays were also found during recoil processes in the aircraft-initiated lightning flashes. The observed x-ray bursts from recoils will be presented in section 5.3.2.

During the ILDAS campaign, multiple seconds to minute long x-ray producing gamma-ray glows were detected. These gamma-ray glows will be presented in section 5.3.3. Events showing positron annihilation signatures were also detected, these will be presented in section 5.3.4.

5.3.1 X-rays observed during negative leader steps

X-rays associated with the stepping process of negative leaders were observed in the ILDAS data. Stepping of the negative leader is observed as fast changes in the measured local electric fields, usually with time correlating current pulses. Some of these steps correlate with measurements of nanosecond long x-ray pulses. A typical nanosecond X-ray pulse with local electric field and current measurements from the ILDAS data can be seen in figure 5.13. X-ray photons were detected at the same moment as a current pulse went through the aircraft, and the measured local electric field pointed towards the detector.

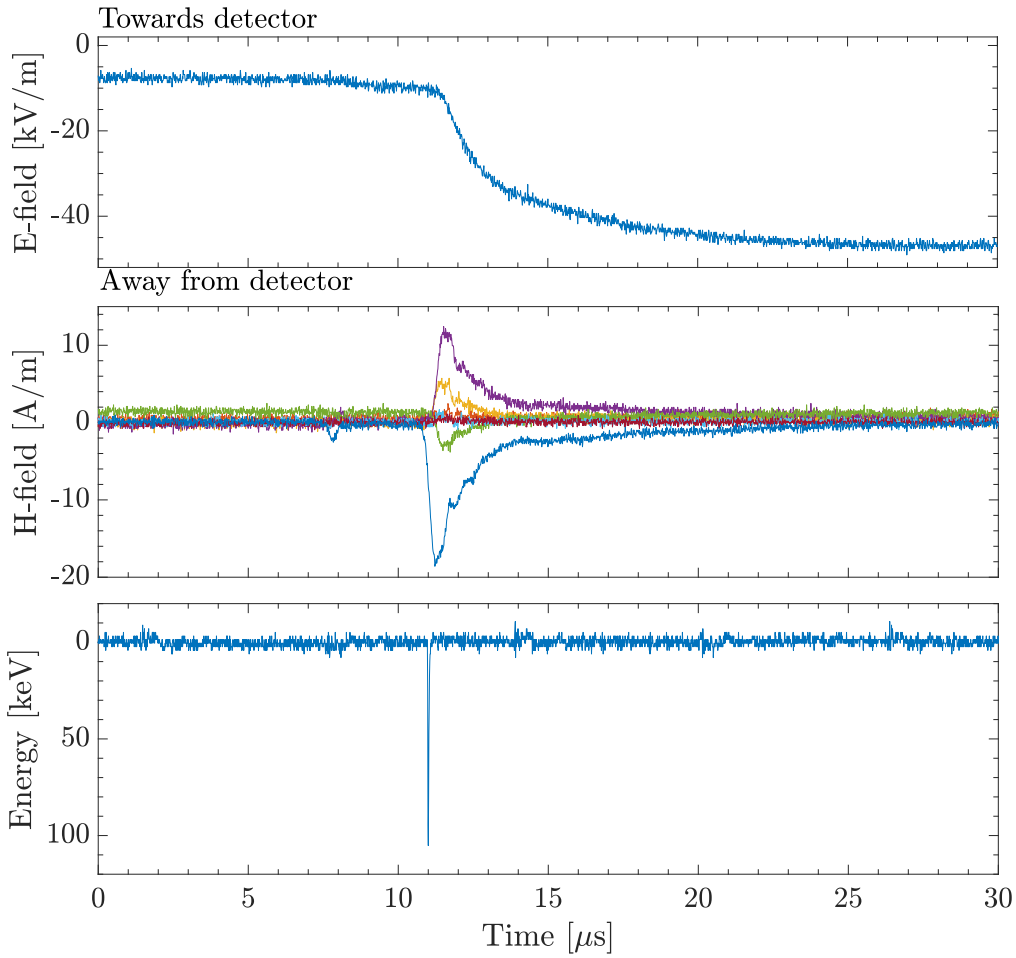

FIGURE 5.13: Local electric field, currents and measured X-ray energy for a photon pulse from flash 0022A9BF at 10.04.2014

The local electric field changes are relatively small, with an average change of 30 kV/m. The changes to the local electric field happen fast, with an average duration of 7.9 μs. In total, 14 such events were found, where the local electric field, current and x-ray pulses correlate temporally, within a few micro seconds. Further 4 events were found where the X-ray pulse preceded the change in local electric field and current by 10 to 100 microseconds. The chance for the x-ray pulse to be accidental cosmic background measured in this time period is shown in table 4.2 in chapter 4.1.4. For 2014 and 2015 the chance of accidentally measuring cosmic background in a 100 microsecond window is below 0.5 %. Figure 5.14 shows the energy distribution of the measured x-ray pulses, with an average pulse energy (red line) of $\approx$ 108 keV.

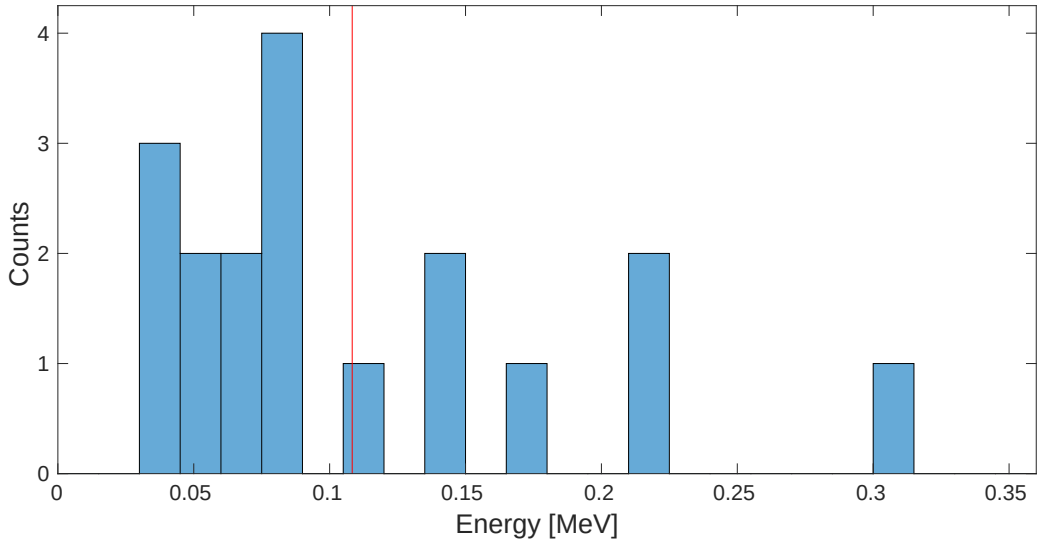

FIGURE 5.14: Measured energies for the x-ray pulses associated with the stepping process of the negative leader. The red line is the average energy. The counts are binned in 15 keV bins.

A few events were found where x-ray bursts seemed to coincide with the stepping of the negative leader. In these events the detectors measured several pulses over a very short time (< 1 μs). One such event of a four pulse burst is presented in figure 5.15. The probability of four background counts being detected in such a short time frame is less than 0.002 %.

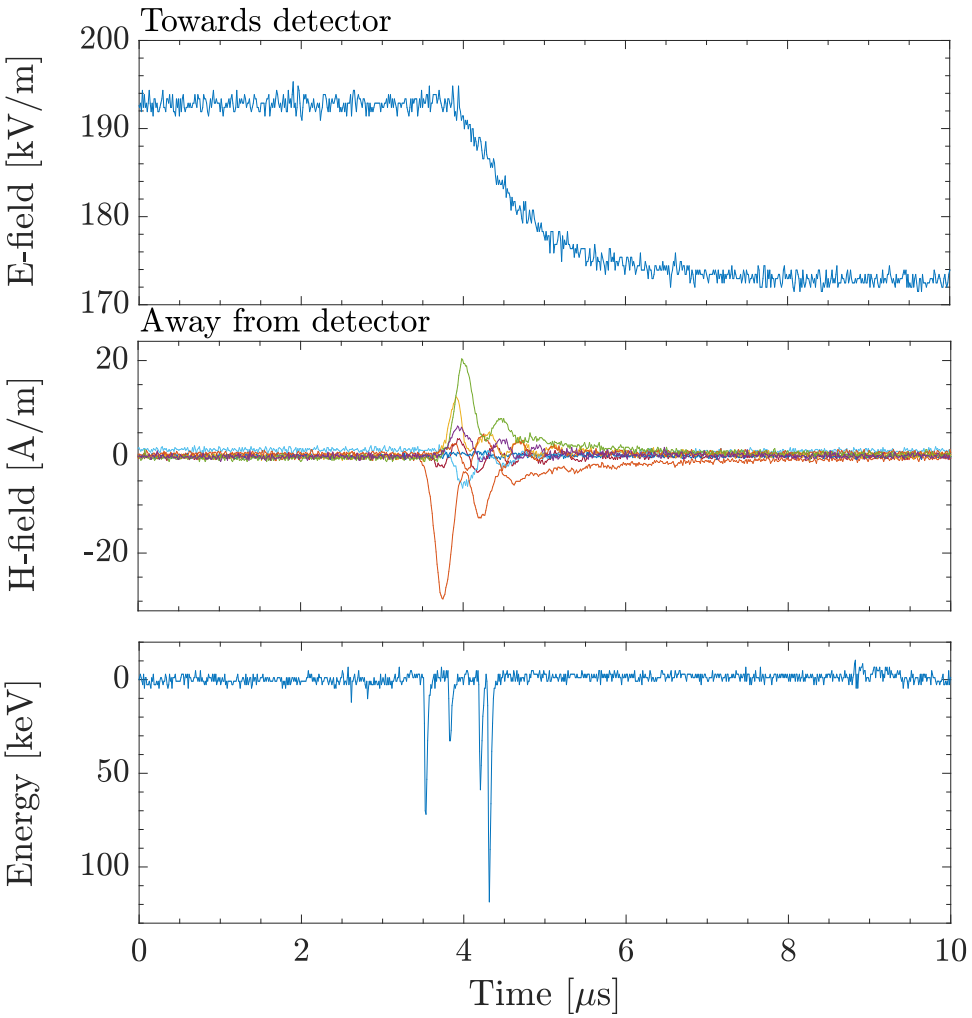

FIGURE 5.15: local electric field, current and x-ray measurements of an x-ray burst during a negative leader step. Measured by ILDAS during flash 504DF164 on 24.04.2014

The event shown in figure 5.15 is very similar to that of the single pulse seen in figure 5.14. The currents from both events are similar, but the time interval for the drop in the local electric field is much smaller for the burst than for the single photon event. Kochkin et al. [2015b] found that the measured energies produced by the stepping of negative leaders did not depend on the amplitude of the current.
The measured x-ray energies during negative leader steps are comparable to the x-ray energies reported by [Dwyer et al., 2005a]. However, Dwyer et al. [2005a] found that the measured pulses consisted of bursts of x-ray photons with energies below 150 keV, rather than high energy gamma rays. The observations by ILDAS is mostly of nanosecond x-ray pulses. The negative leaders generating these x-rays are propagating away from the aircraft, so only the backscattered x-rays can be measured. The x-rays could also be more attenuated, than previously measured x-ray bursts.
All of the measured events were found in the data of the 2014-2015 campaigns, and show no correlation with the defined current classes. The reason for the relatively few measurements of nanosecond long x-ray pulses could be that as mentioned the negative leader is always propagating away from the aircraft, so only the backscattered X-rays can be measured. Other factors could be the detector size, the source intensity, and distance from the aircraft.

5.3.2 X-ray bursts observed during recoils

The second type of radiation producing event is found during recoils. Recoils are fast changes in the local electric field, and are found to be associated with microsecond long x-ray bursts. The local electric field changes are often large, with values of tens to hundreds kV/m, with an average change of ∼188 kV/m. The changes in the local electric field are fast, with a duration of a few micro seconds. Figure 5.16 shows a burst of at least five x-ray photons, with an associated fast and large change in the local electric field of ∼ 200 kV/m and very large and long lasting current fluctuations.

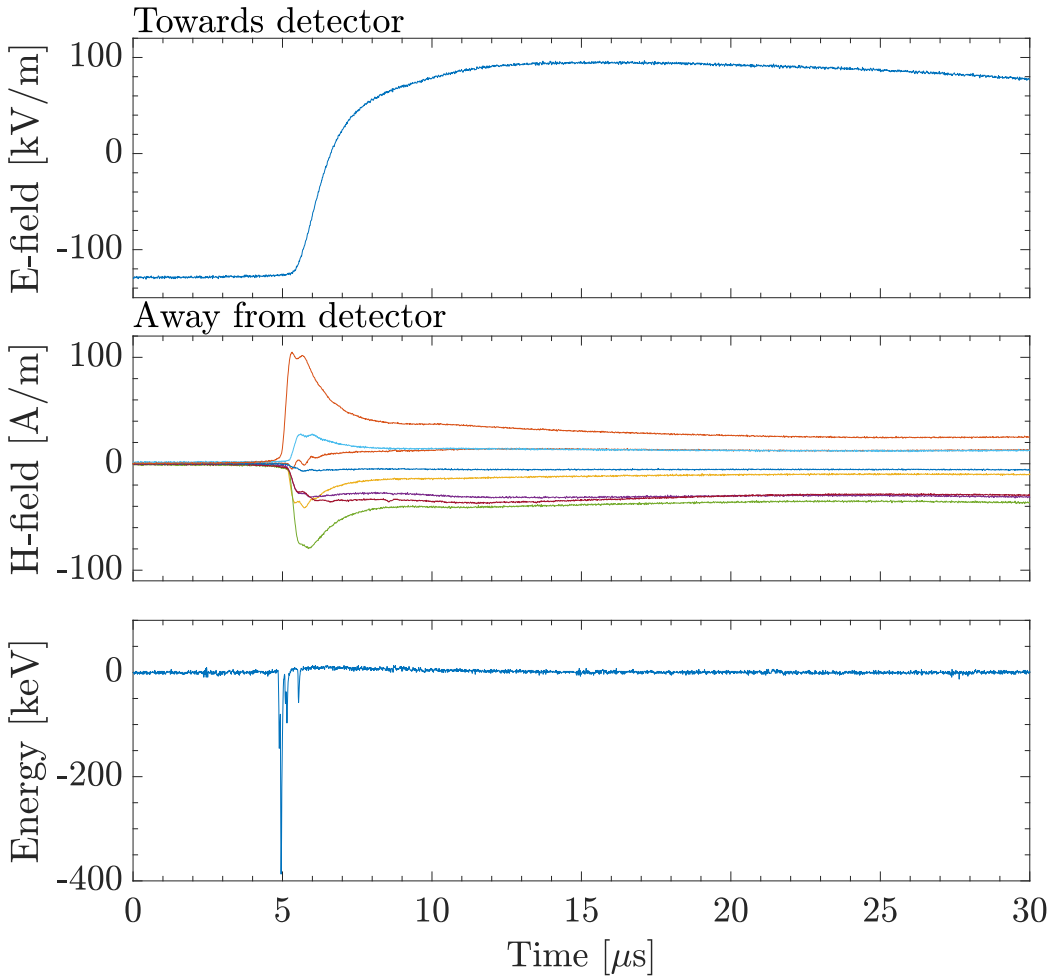

FIGURE 5.16: Local electric field, current and energy measurements of a burst of at least five photons registered by ILDAS during flash 203C8647 on 24.04.2014.

62 x-ray producing recoil events were found, however not all of them had a clear photon count due to the limited time resolution of the detector. Figure 5.17 shows the distribution of photons in 51 of the measured bursts, and figure 5.18 shows the photon energies. One event was removed from the energy spectrum, as it was the only one with extreme values ∼ 5.5 MeV.

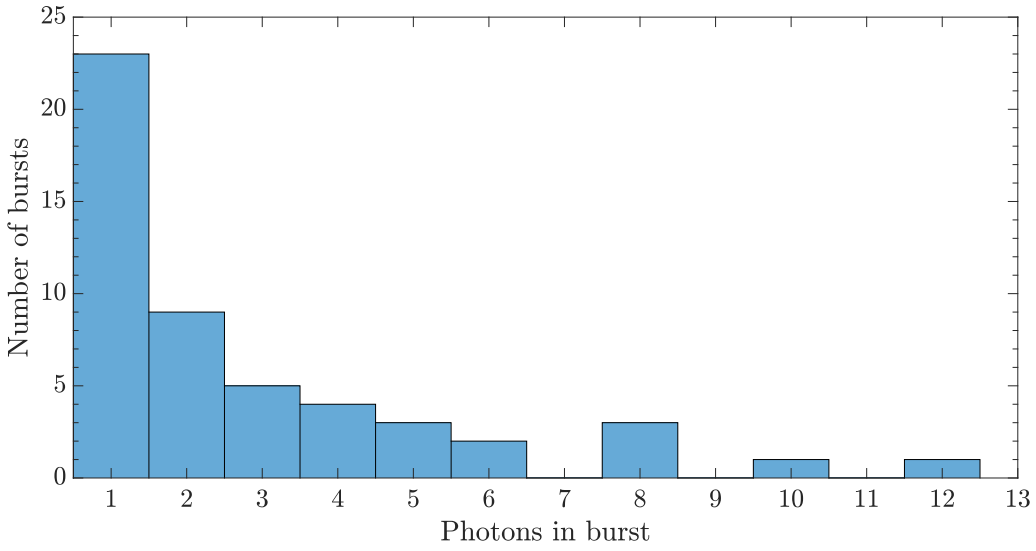

FIGURE 5.17: Distribution of photons in bursts of 51 measured X-ray events.

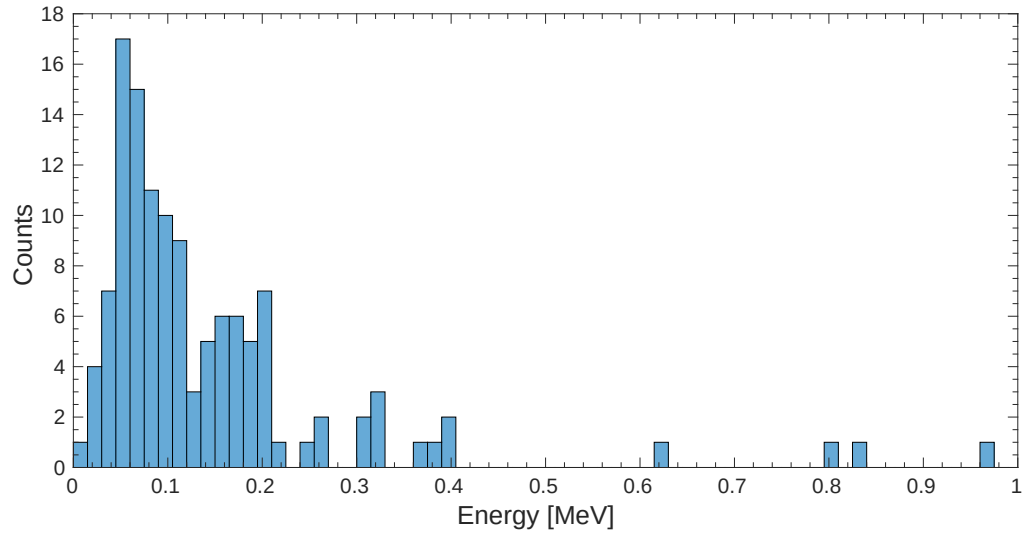

FIGURE 5.18: Photon energy spectrum of 51, microsecond long bursts. Bin size is 15 keV.

The number of photons per burst seems to follow an exponential decline, with the majority of the microsecond long x-ray bursts consisting of single photons. The measured energies are clustered around $\sim$ 100 keV, which is comparable to the energies measured for nanosecond long bursts in section 5.3.1.

The recoil times and changes to the local electric field were compared to the energy and number of photons produced during the recoil. Table 5.4 shows the average burst duration, average recoil duration and average local electric field change during the recoil, for the different photon burst counts.

Photons in burst	Average burst duration [μs]	Average recoil duration [μs]	Average E-field change [kV/m]
1	0.18	5.05	150
2	0.56	3.61	147
3	0.72	4.85	215
4	0.56	3.26	194
5	0.89	7.25	271
6	1.69	3.69	178
8	0.94	4.50	120
10	1.32	2.81	82
12	2.72	4.99	413

TABLE 5.4: Average burst durations, average recoil durations and average local electric field changes during the observed recoils.

As seen in table 5.4, there is no correlation between the burst durations and measured durations and magnitudes of the local electric fields. Table 5.5 shows the average single photon energy and average total burst energies measured during the recoils.

Photons in burst	Number of bursts	Average single pulse energy [MeV]	Average total energy in burst [MeV]
1	23	0.092	0.092
2	9	0.102	0.205
3	5	0.110	0.462
4	4	0.513	1.701
5	3	0.346	1.729
6	2	0.205	1.231
8	3	0.164	1.312
10	1	0.366	3.656
12	1	0.127	1.523

TABLE 5.5: Average pulse energy, and average total burst energies for the x-ray observations during recoil.

As seen in table 5.5, there seems to be a correlation for the average total burst energies measured for bursts consisting of one to three photons, and the average burst durations measured. For bursts with large photon counts the total burst energies and burst durations seems to be random. This could be attributed to the few measurements of bursts with large photon counts.
The twelve events not seen in the burst distribution (figure 5.17) all have an unknown amount of photons, due to the photons arriving too close to each other in time to be differentiated. This results in a wide energy pulse. These twelve events commonly have higher energies than the regular bursts. Figure 5.19 shows the most energetic event observed. The width of the energy curve is much wider compared to that of single photon events such as in figure 5.16, suggesting that the observation is of a cluster of photons with lower energies instead of one high energy photon.

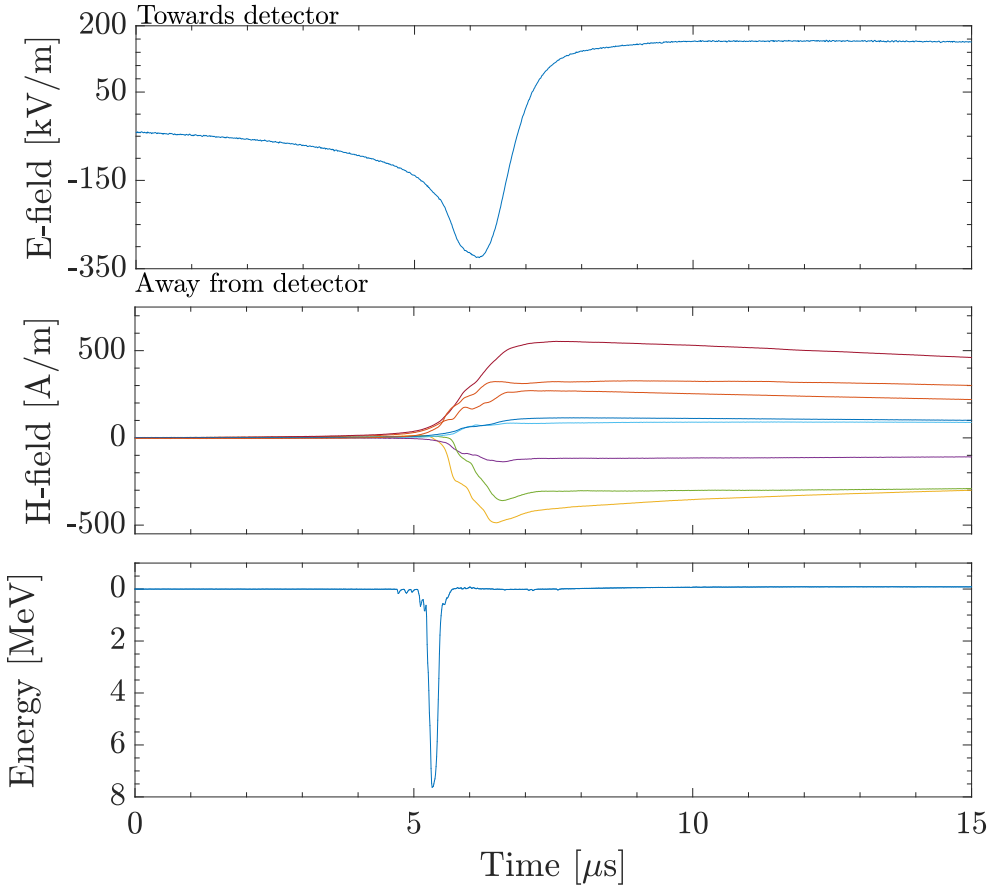

FIGURE 5.19: Local electric field, currents and energy measured during the most energetic recoil event observed by ILDAS. Flash 203C2BF0 on 24.04.2014

The energies and durations of the measured bursts are comparable to those observed by Dwyer et al. [2004] during the dart leader phase. The observed microsecond long x-ray bursts are produced in all current classes defined earlier. The only correlation found between the variables, were a temporal one. The bursts observed during recoils are very similar to the ones observed during the stepping of negative leaders. The local electric fields in both situations are changing rapidly (< 10 μs) and the energy of the photons have similar energies. This could imply that the two types of events share a similar production mechanism.

The observed energy spectrum for nanosecond pulses and microsecond bursts suggests that the x-rays were generated by cold runaway electrons, as the measured energies are relatively low, with very few measurements of energies over 350 keV. This would imply that the x-rays were created from bremsstrahlung by electrons accelerated in the strong electric fields of overlapping streamer regions in front of the leader heads.

5.3.3 Observations of gamma-ray glows

During the 2016 campaign over Australia, multiple gamma-ray glows were observed by ILDAS. Using the updated CDF algorithm, a total of 12 glows and glow candidates were identified. Four of these glows were previously reported by Kochkin et al. [2017] and Kochkin et al. [Under review].

Figure 5.20 shows the measured local electric field minima, maxima and associated x-ray counts for the whole day on 26.01.2016. Two pulses in the count rate can be seen after 04:30:00, which were further investigated. The variations in background are due to the flight trajectory and altitude.

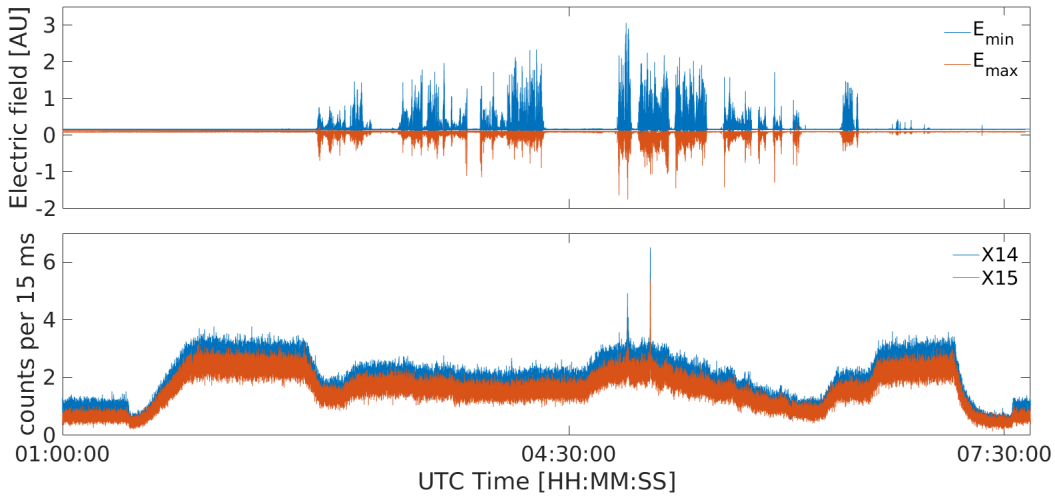

FIGURE 5.20: Electric field and x-ray counts measured on 26.01.2016. The top graph shows the maximum and minimum values for the measured local electric field, plotted in 18 ms bins. The bottom graph shows the x-ray counts from detectors X14 and X15, plotted in 15 ms bins.

Figure 5.21 shows a closer view of the two pulses seen in figure 5.20. A small count rate increase can be seen for the two events, lasting 43 and 24 seconds.

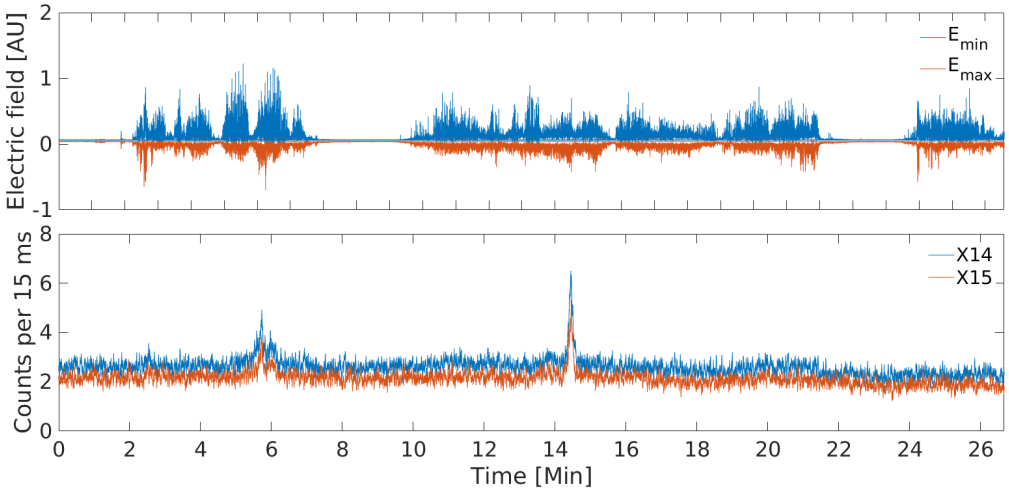

FIGURE 5.21: Zoom in of the two tops in figure 5.20 The top graph shows the maximum and minimum values for the measured local electric field, plotted in 18 ms bins. The bottom graph shows the x-ray counts from detectors X14 and X15, plotted in 15 ms bins.

Figure 5.22 show the second count rate increase, from figures 5.20 and 5.21.

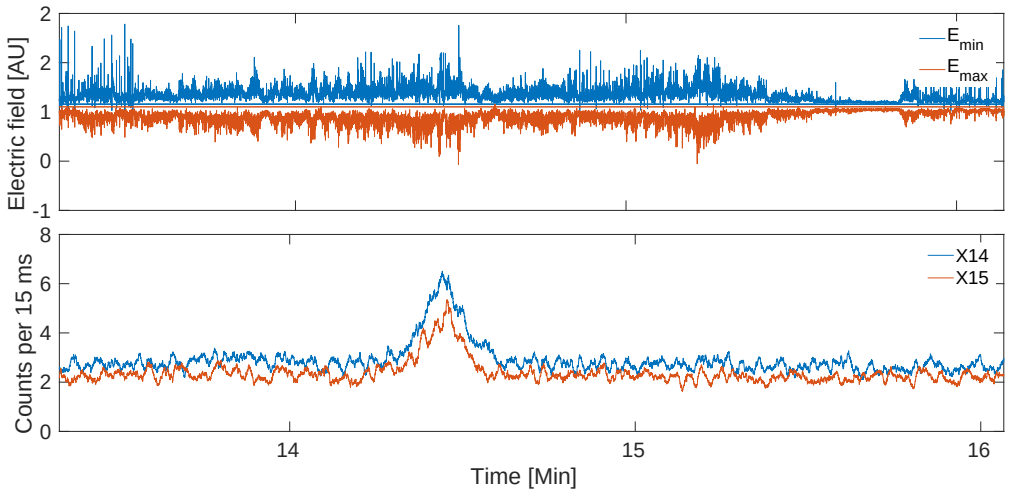

FIGURE 5.22: Zoom in of the second top seen in figures 5.20 and 5.21. The top graph shows the maximum and minimum values for the measured local electric field, plotted in 18 ms bins. The bottom graph shows the x-ray counts from detectors X14 and X15, plotted in 15 ms bins.

Both detectors show a clear count rate increase for a 26 second duration. Twelve more events like this were found in the ILDAS data, four of which are confirmed glows from previous observations. Table 5.6 shows the measured duration and count rates for the two x-ray detectors for all glows and glow candidates found in the ILDAS dataset. The bold lines indicate data from the previously confirmed

glows of Kochkin et al. [2017] and Kochkin et al. [Under review]. The count rate differences between detector X14 and X15 is due to the difference in energy channels used by each detector, and the distance to the source.

Date	Duration [s]	Background counts (X14) [s^{-1}]	Glow counts (X14) [s^{-1}]	Background counts (X15) [s^{-1}]	Glow counts (X15) [s^{-1}]
14.01.2016	51	125.3 ± 11.2	144.8 ± 12.0	104.8 ± 10.2	122.2 ± 11.1
14.01.2016	**19**	$\mathbf{158.7 \pm 12.6}$	$\mathbf{254.2 \pm 15.9}$	$\mathbf{143.6 \pm 12.0}$	$\mathbf{208.4 \pm 14.4}$
14.01.2016	**55**	$\mathbf{172.5 \pm 13.1}$	$\mathbf{220.7 \pm 14.9}$	$\mathbf{147.0 \pm 12.1}$	$\mathbf{179.9 \pm 13.4}$
14.01.2016	27	177.8 ± 13.3	215.0 ± 14.7	149.4 ± 12.2	167.3 ± 12.9
15.01.2016	**21**	$\mathbf{255.4 \pm 16.0}$	$\mathbf{2160.2 \pm 46.5}$	$\mathbf{202.8 \pm 14.2}$	$\mathbf{1251.9 \pm 35.4}$
15.01.2016	**45**	$\mathbf{181.9 \pm 13.5}$	$\mathbf{416.6 \pm 20.4}$	$\mathbf{152.6 \pm 12.4}$	$\mathbf{297.5 \pm 17.2}$
22.01.2016	30	136.9 ± 11.7	176.7 ± 13.3	113.8 ± 10.7	142.3 ± 11.9
22.01.2016	41	176.6 ± 13.3	203.6 ± 14.3	146.5 ± 12.1	157.6 ± 12.6
24.01.2016	81	161.1 ± 12.7	188.5 ± 13.7	129.5 ± 11.4	153.2 ± 12.4
24.01.2016	48	164.9 ± 12.8	186.8 ± 13.7	129.4 ± 11.4	145.6 ± 12.1
26.01.2016	43	177.2 ± 13.3	227.6 ± 15.1	144.4 ± 12.0	178.7 ± 13.4
26.01.2016	24	178.8 ± 13.4	266.3 ± 16.3	149.4 ± 12.2	213.2 ± 14.6

TABLE 5.6: Duration, background counts and glow counts of potential glows, with uncertainties. The bold lines indicate data from confirmed glows. The measurements from the same date are sorted in time.

As seen in table 5.6, most of the newly found glow candidates have low count rates compared to some of the previously confirmed glows. Table 5.7 show the measured sigma values over background for the events in table 5.6.

Date	X14 σ	X15 σ
14.01.2016	1.7	1.7
14.01.2016	**7.6**	**5.4**
14.01.2016	**3.7**	**2.7**
14.01.2016	2.8	1.5
15.01.2016	**119.2**	**73.7**
15.01.2016	**17.4**	**11.7**
22.01.2016	3.4	2.7
22.01.2016	2.0	0.9
24.01.2016	2.2	2.1
24.01.2016	1.7	1.4
26.01.2016	3.8	2.9
26.01.2016	6.5	5.2

TABLE 5.7: Sigma over background counts for peak count values of the observed glows and glow candidates.

As seen from table 5.7, the intensity of the newly found glow candidates are weak compared to the two confirmed glows seen on 15.01.2016. Only the observations from 26.01.2016 shows significant x-ray count rate increases, comparable to the ones observed by Kochkin et al. [Under review]. The observations might still be of distant glow, which would result in lower observed count rate increases, due to the attenuation of photons.

Glow Terminating event

Kelly [2014] showed that lightning activity is suppressed after a gamma ray glow. Figure 5.23 shows the amount of lightning flashes observed during 500 second period in a 30 km radius around the glow terminating flash. The lighting counts are binned to 20 seconds.

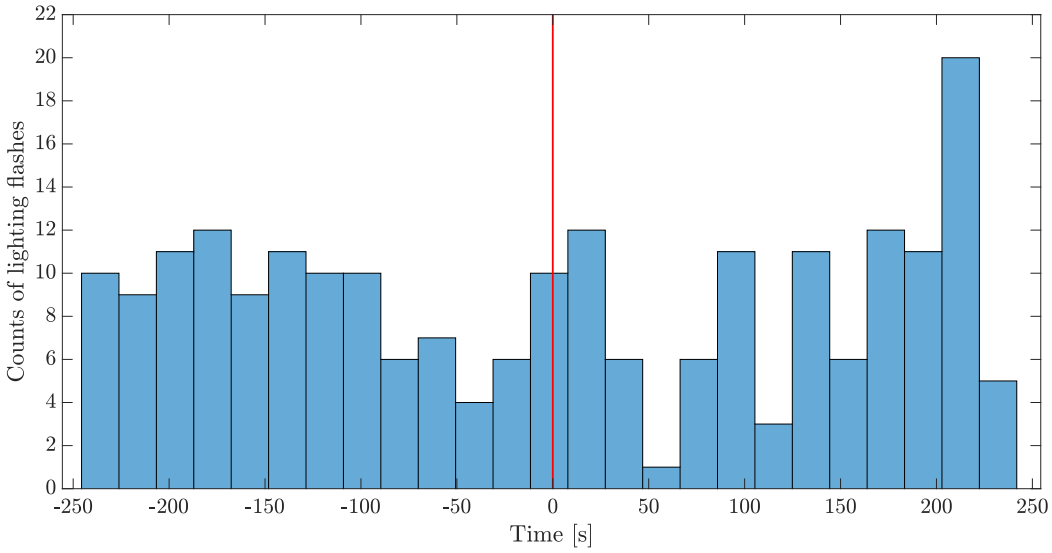

FIGURE 5.23: Lightning flashes observed in an area around the glow terminating flash, observed by Kochkin et. al. on 15.01.2016. The bin size is 20 seconds.

No such correlation was found for any combination of time period and area. This is the only glow that was terminated by lightning observed by ILDAS (seen in figure 1.2 in chapter 1), so no more data is available. One single observation is not enough to conclude that this is statistically significant.

5.3.4 Observations of positron annihilation signatures

During a flight over northern Australia on 14.01.2016, several x-ray enhancements were detected by ILDAS. At the time the aircraft was flying at 12 km altitude in presence of gamma-ray glows. In a paper by Kochkin et al. [Under review] (with myself as a co-author) we report observing positron annihilation signatures in two of the observed aircraft-triggered flashes during this period. The two events reported by Kochkin et al. [Under review] will be reported here, with two additional events which shows similar annihilation signatures.

Figure 5.24 shows the total observed x-ray counts of 9 of the 10 triggers recorded from the flight. Data for one event are missing due to the buffers being full. The colours represent a time difference in the events recorded. The green counts are from flashes observed between 05:20 - 05:22, the blue counts from 07:19 - 07:23, and the purple counts from 07:53 - 07:56. The zero time in figure 5.24 correspond to the initiation time of the aircraft-initiated lighting flash.

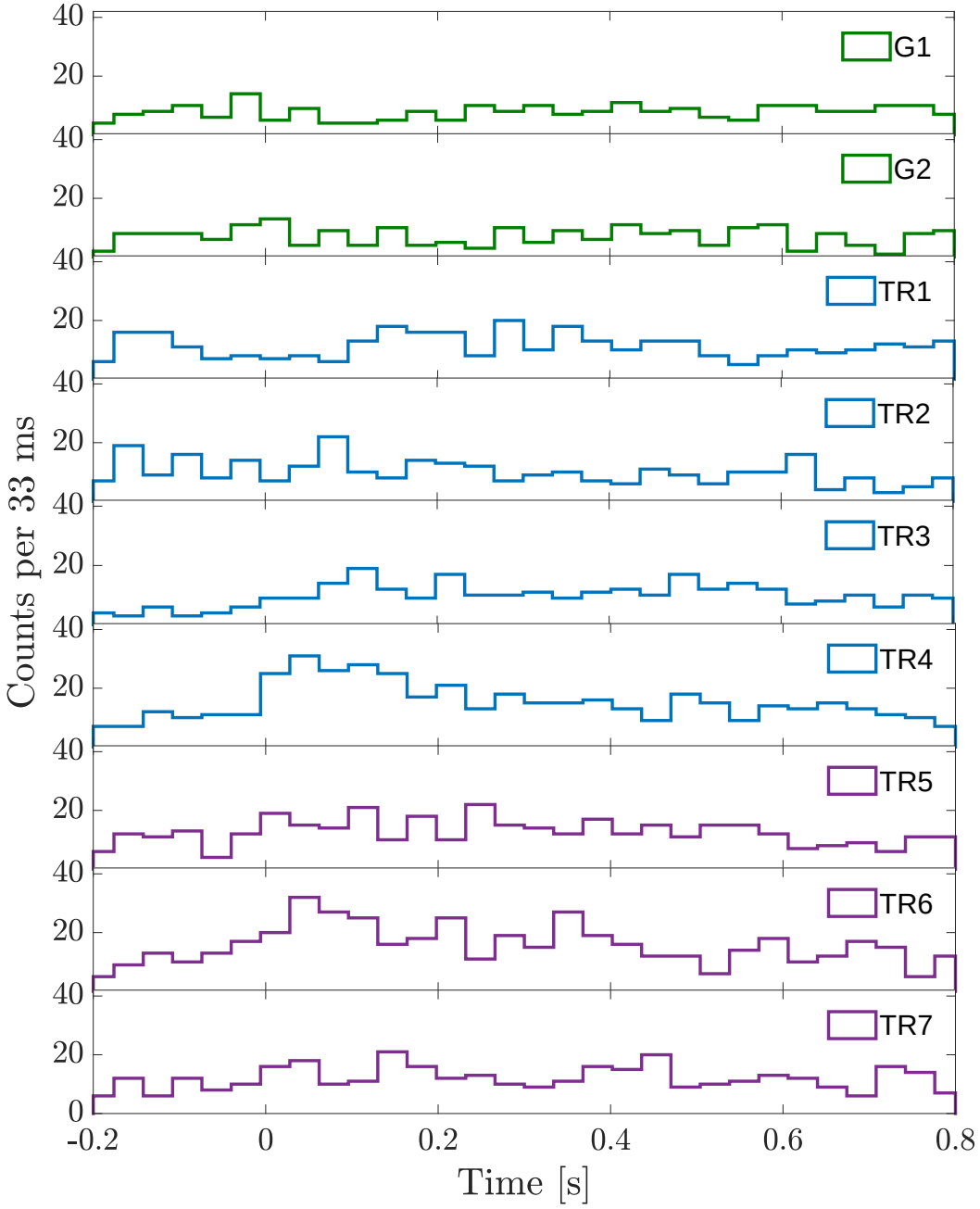

FIGURE 5.24: X-ray counts for all aircraft triggers on 14.01.2016, with 33 ms bin sizes. The different colours represent different time groups of the day.

As seen in figure 5.24, trigger 4 and trigger 6 show a clear increase in counts compared to the other events from the flight. Kochkin et al. [Under review] reported finding positron annihilation signatures during triggers 3 and 4.

Figure 5.25 shows the x-ray counts, flightpath, and altitude of the aircraft, associated with parts of the flight. The top panel shows the aircraft path, with locations of the measured x-ray pulse peaks. The grey dots represent lightning flashes observed by LIAS. The middle panel shows the altitude of the aircraft during the flight. The aircraft increases the altitude several times, which affects the measured background

counts. This can be seen in the background rates before and after location A. The bottom panel shows the measured x-ray count rate, binned to 15 ms.

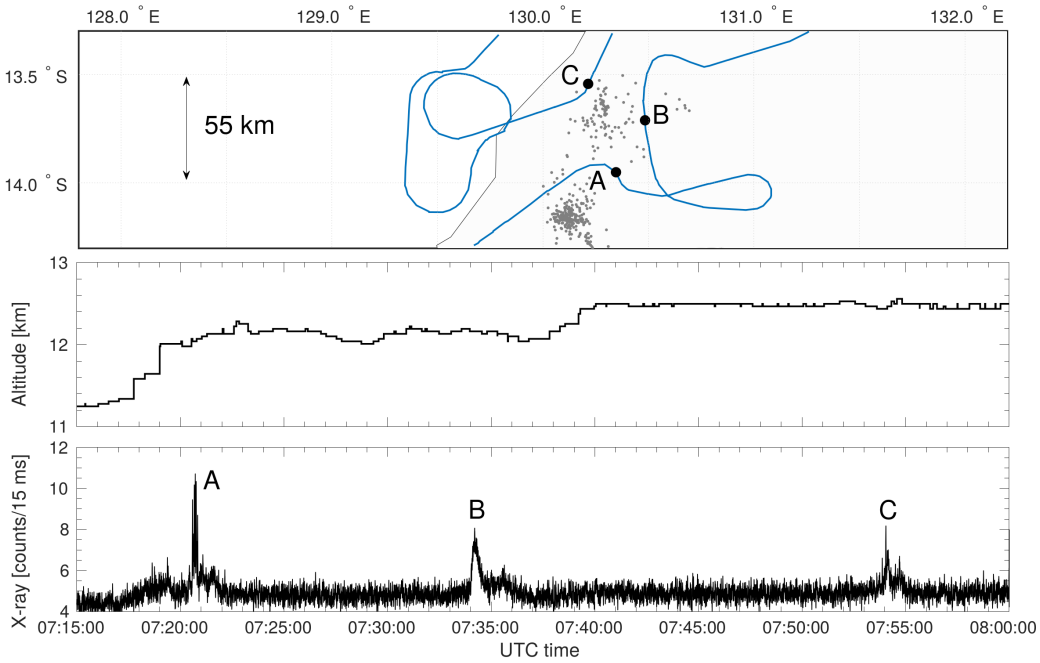

FIGURE 5.25: Flight path, altitude profile and x-ray counts measured by ILDAS on 14.01.2016 from 07:15 to 08:00. Top panel shows a cut out of the aircraft flight path. The grey dots represents lightning flashes registered by LIAS, between 07:15 and 08:00. The middle panel shows the altitude profile of the aircraft. The bottom panel shows the x-ray counts per 15 ms. Image from [Kochkin et al., Under review].

As seen in figure 5.25, there are 3 major increases in the x-ray count rate during this period. These count rate increases have been identified as gamma-ray glows. Location A corresponds to the blue counts, while location C correspond to the purple counts in figure 5.25. ILDAS did not trigger while at location B, so there are no trigger data for this period. Kochkin et al. [Under review] reports their findings while flying close to location A in figure 5.25. The two new findings are found while flying close to location C, about 30 minutes after the aircraft was at location A.

Positron annihilation signatures around location A

The findings presented in this section are mainly from Kochkin et al. [Under review]. The background subtracted count rates and energy spectrum have been replotted with the methods used in this thesis, for comparison reasons.

Figure 5.26 shows the measured local electric field and x-ray counts for four minutes of flight time near location A. The local electric field is plotted using the maximum and minimum measured values over 18 ms. During the plotted time period, ILDAS triggered 4 times, as shown in figure 5.26. As seen, the first group of local electric field pulses (trigger 1 and 2) are not associated with increased x-ray counts, while the local electric field pulses seen at location A correlate with pulses in the x-ray counts.

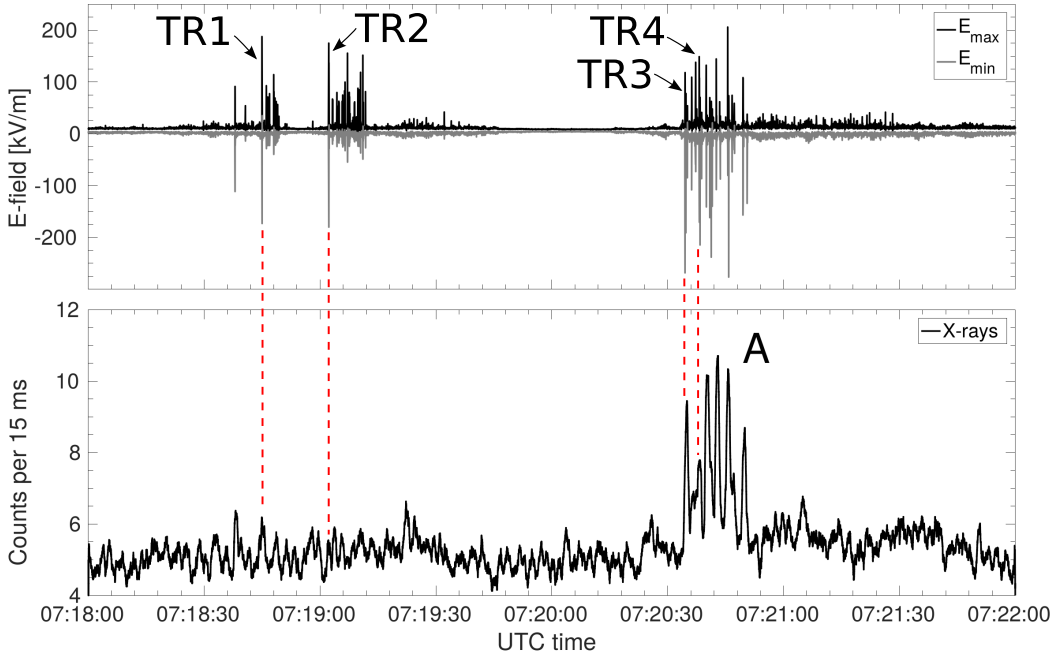

FIGURE 5.26: The local electric field minimum, maximum and x-ray count rate for 4 minutes of flight close to location A. The local electric field is plotted as maximum and minimum values in 18 ms bins, and the x-ray counts are binned to 15 ms intervals. The red dotted lines represents four ILDAS triggers observed during this period. Figure from [Kochkin et al., Under review].

The background subtracted x-ray counts with error bars for the four triggers are shown in figure 5.27. As seen, all triggers show significant count rate increases over the measured background. Trigger 3 and 4 shows an increase in counts right after the initiation time (at 0 seconds).

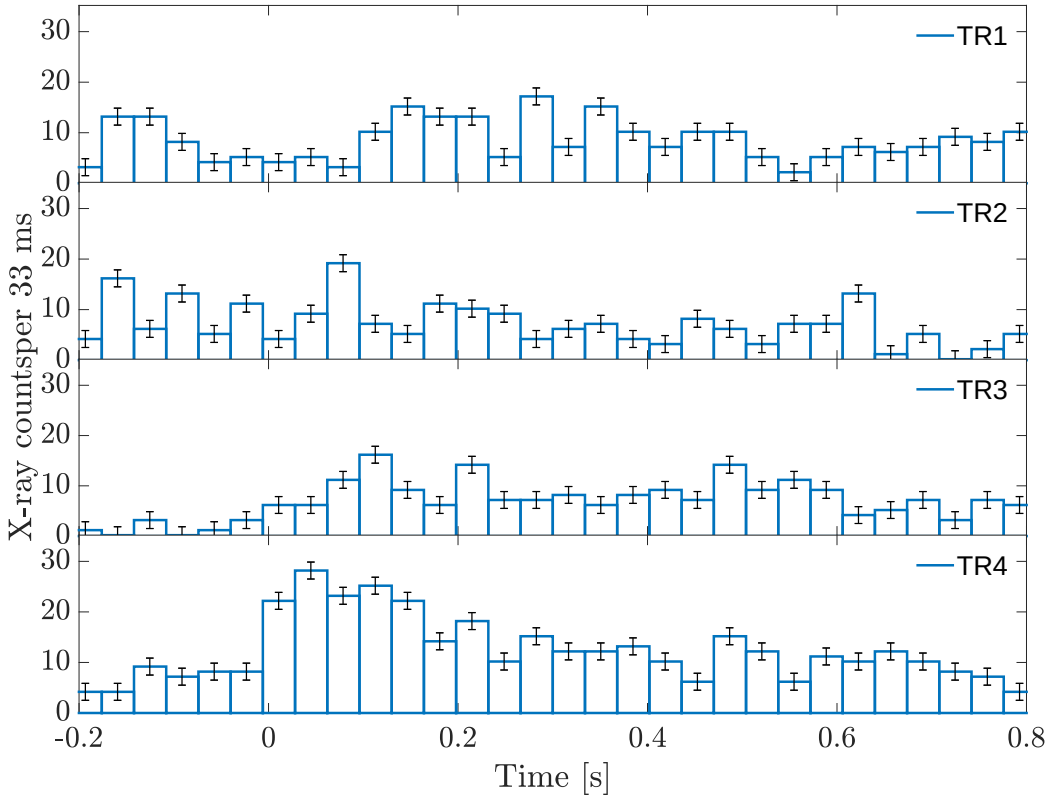

FIGURE 5.27: Background subtracted x-ray counts in 33 ms bins, for the four triggers observed close to location A.

The energy spectra for the four triggers close to point A are shown in figure 5.28. The measured x-ray energies are from both X14 and X15 detectors, and binned to 35 keV. Only x-rays with energies over 80 keV are included. Trigger 1 and 2 correspond to the two triggers observed without increased x-ray count rates in figure 5.26. Trigger 3 and 4 correspond to the triggers observed during the pulses of increased x-ray count rates. A clear x-ray count rate increase around 511 keV can be seen for trigger 3, and to some lesser extent for trigger 4.

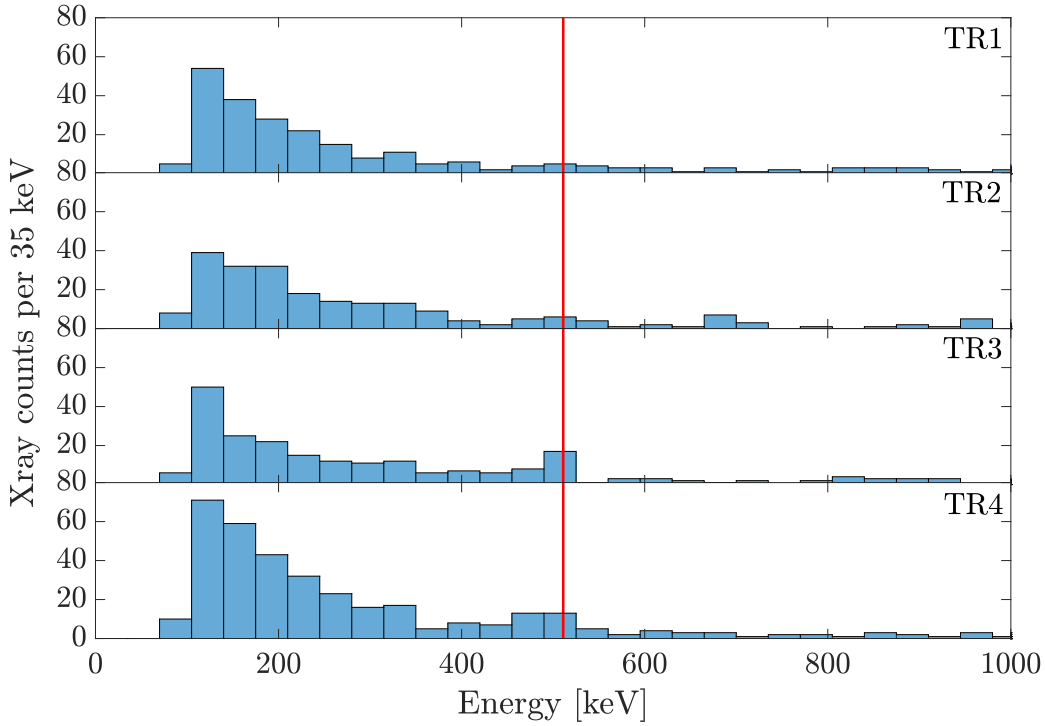

FIGURE 5.28: X-ray counts for the four triggers at location A, binned to 35 keV. The red line show the location of the 511 keV value.

The local electric fields and x-ray counts measured during trigger 3 and 4 are shown in figure 5.29. The top panel shows the local electric field on the aircraft during the triggered lightning flash. The two local electric fields are very similar, and show a clear periodicity in the observed pulses (marked with red lines). The time between the pulses are $\sim$ 200 ms, with TR4 missing a pulse at 0.4 seconds. The middle panel shows the energy and time of each measured x-ray photon during the two lighting flashes. The bottom panel shows the x-ray counts for photons over 100 keV, binned to 15 ms.

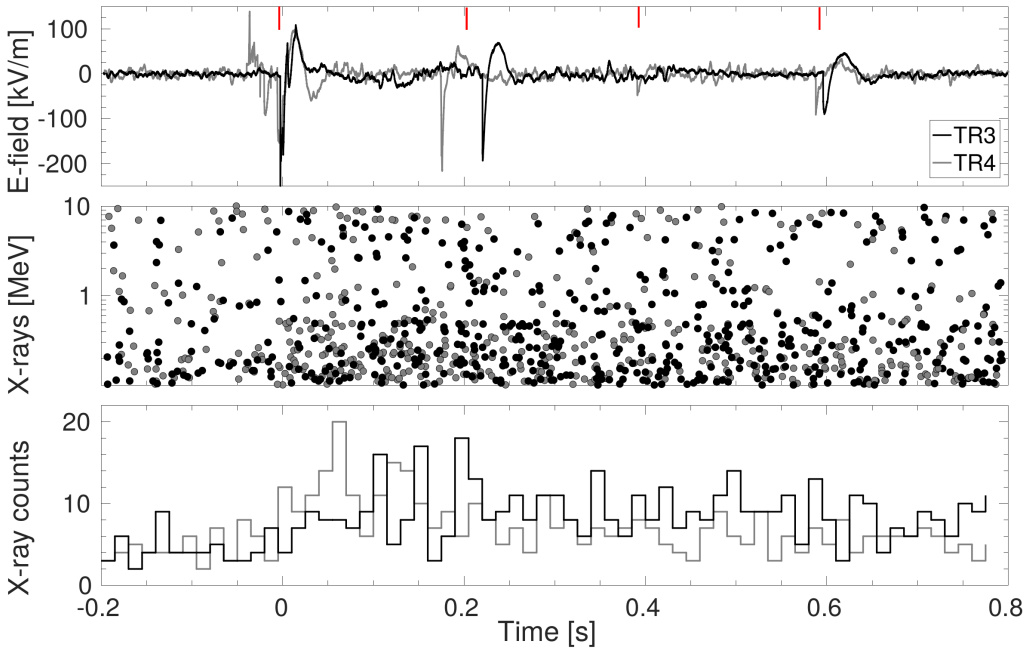

FIGURE 5.29: The measured electric field, energies and counts for x-rays above 100 keV during trigger 3 (black) and 4 (grey). Image from [Kochkin et al., Under review].

As seen in figure 5.29, the pulses in the local electric fields and x-ray count rate increases do not correlate in time. The x-ray count rate maxima of both triggers are observed after the initial local electric field pulses. The increased observed x-ray count rates are also lasting much longer than the observed pulses.

Figures 5.30 and 5.31 shows the local electric fields and currents during the initiation phase for trigger 3 and 4. As seen, they are not comparable to any of the two previously measured local electric field patterns observed during leader initiation. One would also expect the initiations to contain large current pulses, correlated to the stepping of negative leaders. Trigger 3 only show a single current pulse, at the first pulse in the local electric field. This pulse shows the current entering the aircraft at all extremities like the current class shown in section 5.2.2, meaning electrons are leaving the aircraft at all extremities. The current pulses observed during trigger 4 show the same pattern. This is a strong indicator that the observed trigger is not an aircraft-triggered lighting strike but static discharge.

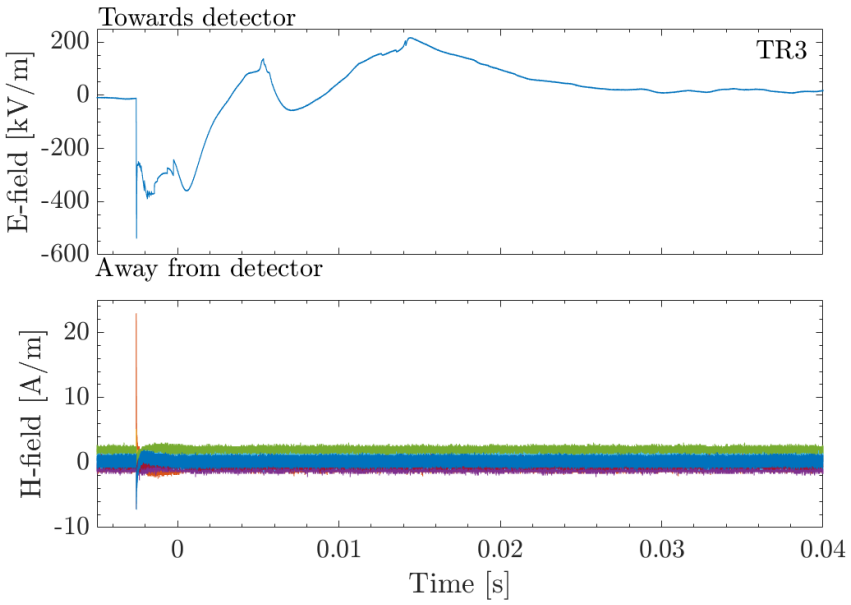

FIGURE 5.30: The measured local electric field and currents during the initiation phase of trigger 3.

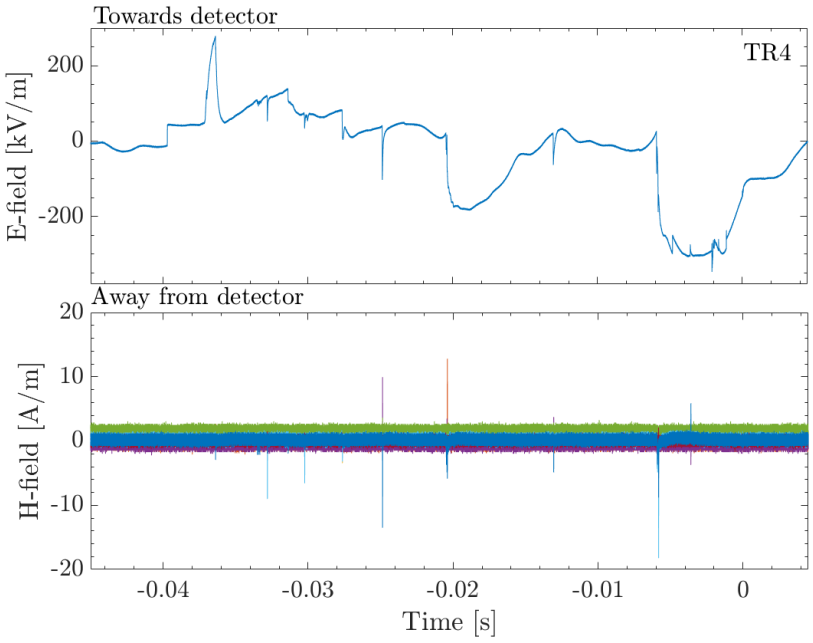

FIGURE 5.31: The measured local electric field and currents during the initiation phase of trigger 4.

From analysis of the electric fields and x-ray data we concluded that the observed x-ray count rate increase and local electric field pulses were associated with negative

static discharges from static wicks on board the aircraft.

Positron annihilation signatures around location C

This section will present the two new triggers, showing positron annihilation signatures. These triggers were found approximately 30 minutes later than the triggers we previously reported, while the aircraft was at location C in figure 5.25.

Figure 5.32 shows the local electric field and x-ray counts during a time period close to location C in figure 5.25. During the plotted time ILDAS triggered 3 times, as indicated in the figure. The observed count rate is much smaller than that observed for the period at location A in figure 5.26. The local electric field pulses of trigger 5 and 6 show correlating pulses in x-ray counts.

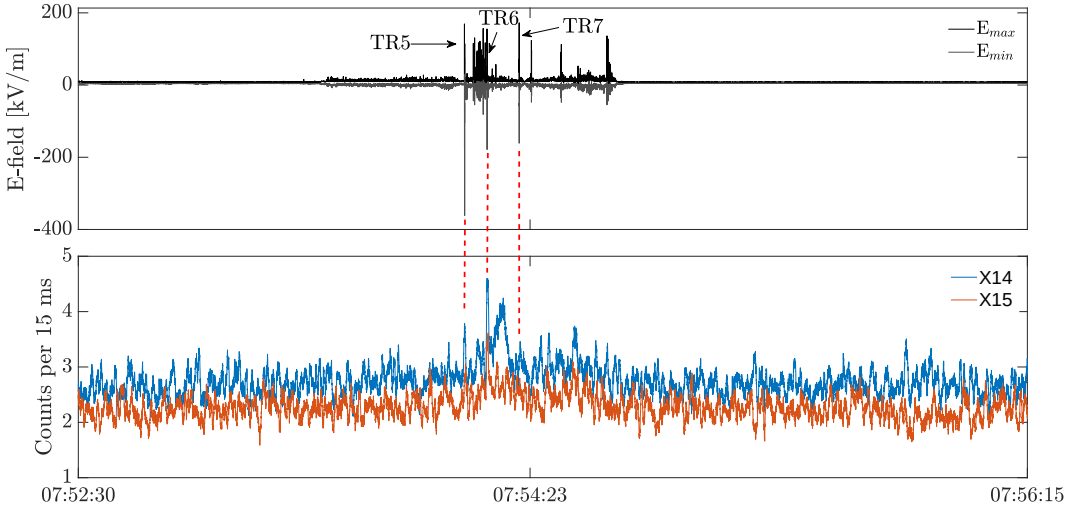

FIGURE 5.32: Maximum and minimum measured local electric field and x-ray count rates during 3 minutes and 45 seconds of flight close to location C. The local electric field is plotted as maximum and minimum values in 18 ms intervals, and the x-ray counts are binned to 15 ms intervals.

Figure 5.33 show the background subtracted x-ray counts with error bars for the three triggers observed at location C. Trigger 6 show an especially large count rate increase, comparable to that of trigger 4 in figure 5.27.

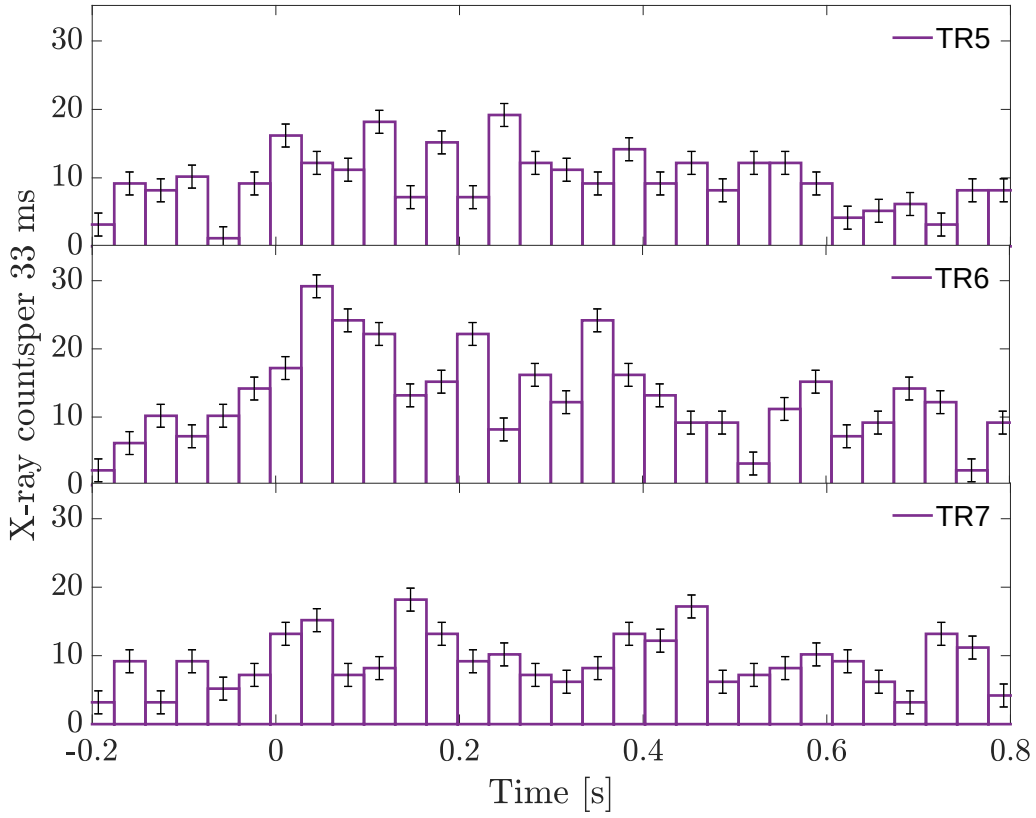

FIGURE 5.33: Background subtracted x-ray counts in 33 ms bins, for the three triggers observed close to location C.

The energy spectra of the three triggers close to location C can be seen in figure 5.34. The measured x-ray energies are from both X14 and X15 detectors, binned to 35 keV and only include energies over 80 keV. Triggers 6 and 7 show a clear x-ray count rate increase of the 511 keV bin.

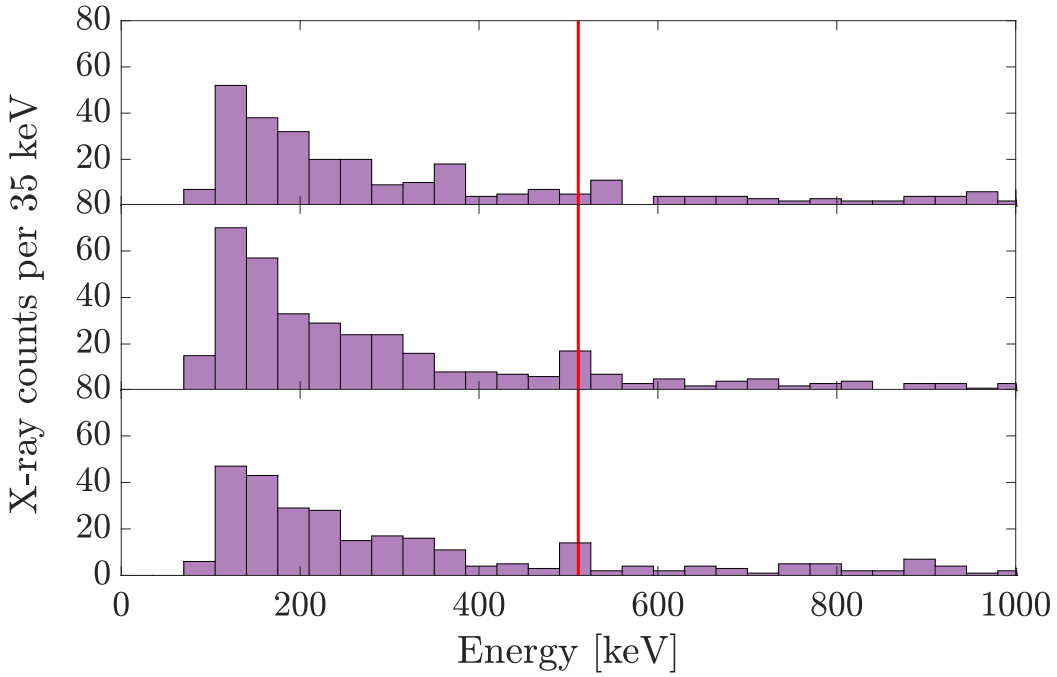

FIGURE 5.34: X-ray counts in 35 keV bins, for the three events between at location C, binned to 35 keV. The red line show the location of the 511 keV value.

The local electric fields and x-ray counts for triggers 6 and 7 are shown in figure 5.35. There are similarities in the local electric fields and x-ray counts of triggers 6 and 7 to those observed for triggers 3 and 4 in figure 5.29. Again both x-ray count rate maxima are observed a period after the initial local electric field pulse. The local electric field of trigger 6 correlate with the observed start of the x-ray count rate increase, less so for trigger 7. A single local electric field pulse can be seen for trigger 6 at around 0.4 s, marked by a red line.

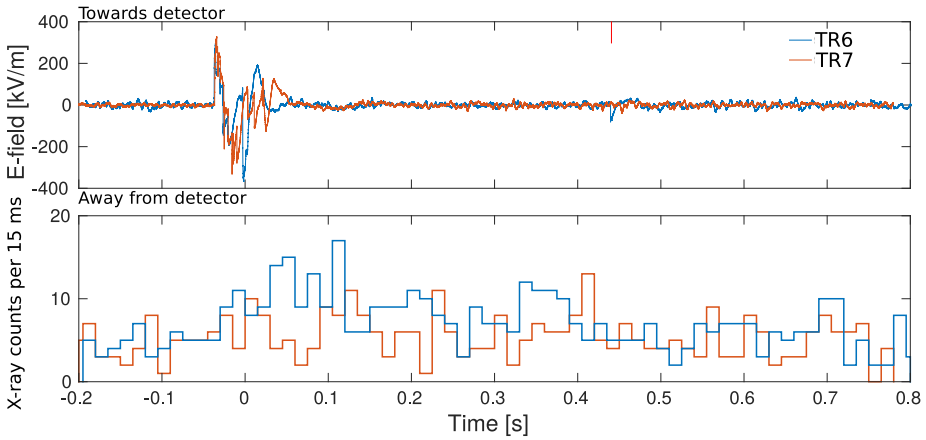

FIGURE 5.35: Local electric fields and x-ray counts for the two triggers observed at location C. The x-ray counts are binned to 15 ms.

Figure 5.36 and 5.37 shows the local electric fields measured during the initiation

phase for triggers 6 and 7. Figure 5.36 also show current measurements for the initiation phase. The buffer were full during trigger 7, so there are no current measurements during this trigger.

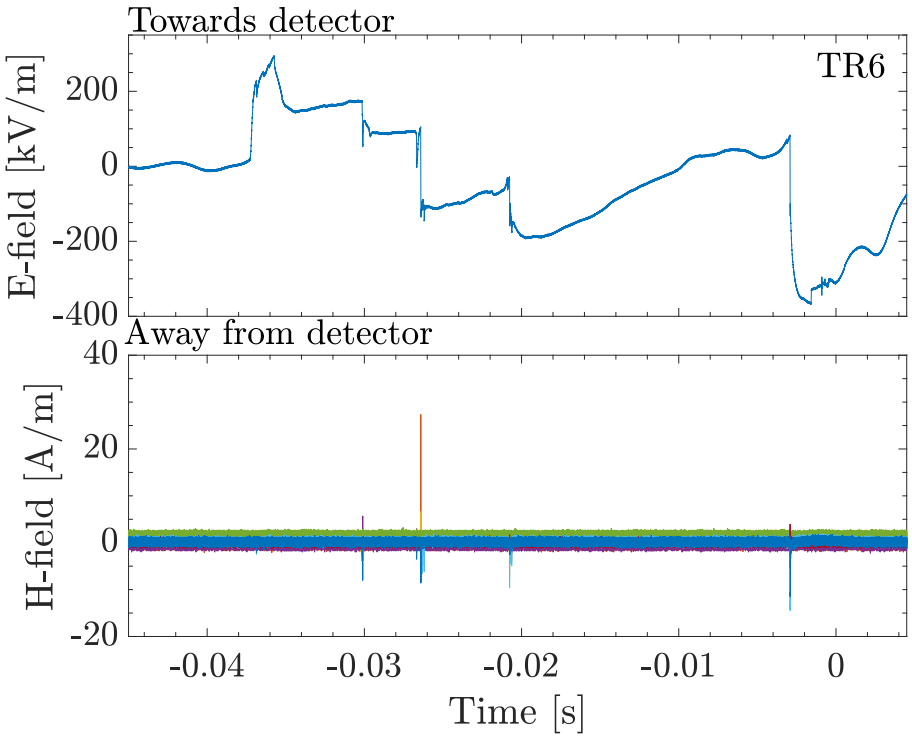

FIGURE 5.36: The measured local electric field and currents during the initiation phase of trigger 6.

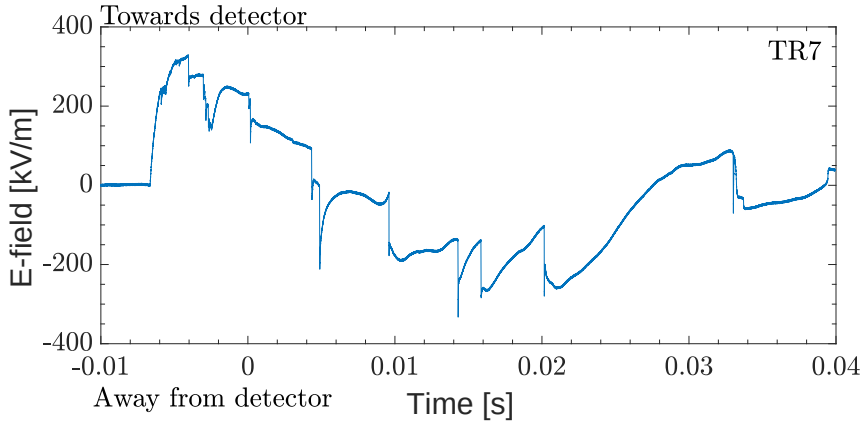

FIGURE 5.37: The measured local electric field during the initiation phase of trigger 7.

The local electric fields measured during trigger 6 and 7 both show a rapid rise in the measured electric field strength at initiation. This will make the local electric

fields point towards the detector. Several rapid pulses in the local electric field are observed for both triggers. The current pulses measured in trigger 6 show the current entering the aircraft at all extremities, similar to the observations from triggers 3 and 4. This again suggests that these are not aircraft-triggered lightning flashes, but static discharges at the extremities of the aircraft.

Figure 5.38 shows a camera observation of a static discharge from the left wing of the aircraft used in the 2016 campaign.

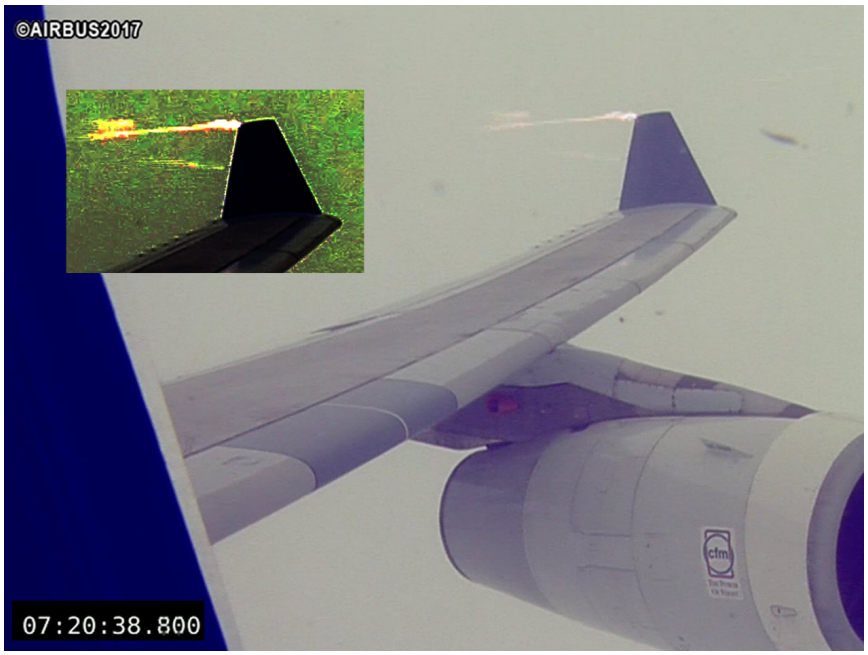

FIGURE 5.38: Camera observations of static discharge on the left wing during trigger 4.

The observed local electric fields, current patterns, and camera observation all suggest that the observed events are static discharges and not aircraft-initiated lightning discharges. How positrons are generated in these discharges is still a mystery.

Chapter 6

Summary

The main questions of this thesis is: When during a lighting flash do we observe x-rays, and is the production of x-rays related to changes in the current or local electric fields measured on the aircraft? Are x-rays observed without associated aircraft-initiated lightning flashes?

This thesis has shown a preference in leader initiation location on the aircraft. All negative leaders initiations are found to include the nose or tail of the aircraft. A dependence on aircraft type and/or flight altitude has also been observed, with distinct current patterns for different campaigns. We have also observed static discharges where electrons leave the aircraft at all extremities.

This thesis has also shown a temporal correlation between nanosecond pulses and microsecond bursts of x-rays, observed during the stepping of negative leaders, and during recoil events of aircraft-triggered lighting flashes. No correlation could be found between the measured energies and the changes to the local electric fields or current magnitudes measured during the x-ray events. The energy spectra of the nanosecond pulses and microsecond bursts are quite similar, with few event with energies over 350 keV. Both type of events show a majority of single pulses with energies typically around 100 keV. This suggests that the two events share a similar production mechanism, and that the x-ray production is attributed to the high electric fields in the streamer or leader heads.

Multiple observations of second to minute long count rate enhancements were analysed, showing similarities to previously observed gamma-ray glows. Only one of the measured glow candidates show statistical significance in count rate increases. The less intense glow candidates could still be distant glows. The attenuation of photons over a large distance could explain the relatively weak measurements.

Observations of x-ray enhancements with increased counts of 511 keV photons have been reported, suggesting observations of positron annihilations. The events were found to be related to static discharges at the extremities of the aircraft. No conclusion of production mechanism or origin of the observed phenomena can be made.

Chapter 7

Future work

This chapter will highlight some open questions and suggest some future work.

1. All observations of aircraft-triggered lighting show clear preferences for leader initiation locations. Can these initiation locations be predetermined?
2. Can the asymmetry between the electric fields needed to launch positive and negative leaders be used to mitigate the chance for aircraft-triggered lighting?
3. During the campaigns, only 18 events were found in correlation to stepping of negative leaders, more data is needed to get a better understanding of the energy spectra of these events. Further study of the observed energy spectra during leader steps and recoils are necessary to determine the underlying production mechanisms. A model of the observed events with comparisons to the two main electron runaway models could provide insights into these production mechanisms.
4. Positron annihilation signatures are still largely unexplained. No current atmospheric phenomena can explain the observations of positron annihilation signatures. The signatures are found to be related to static discharges at the extremities of the aircraft. A controlled laboratory experiment where similar static discharges are reproduced in high electric field environments, might provide insights to the relation between the observations of positron annihilation and static dischargers.

Appendix A

Noise graphs

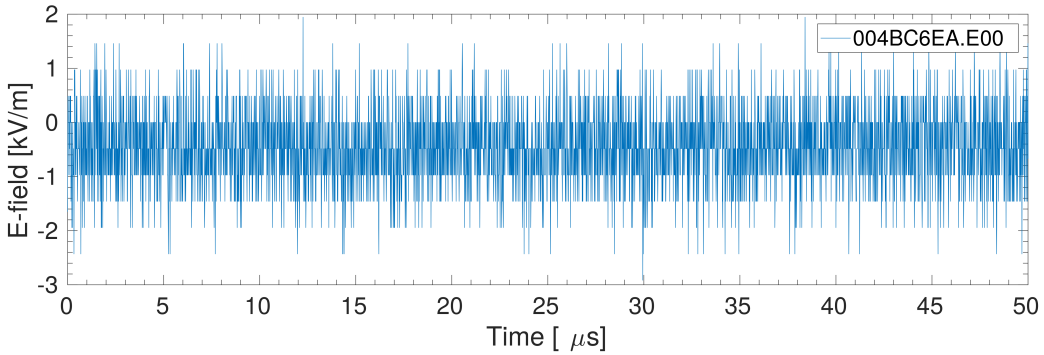

FIGURE A.1: Noise in the local electric field measurements.

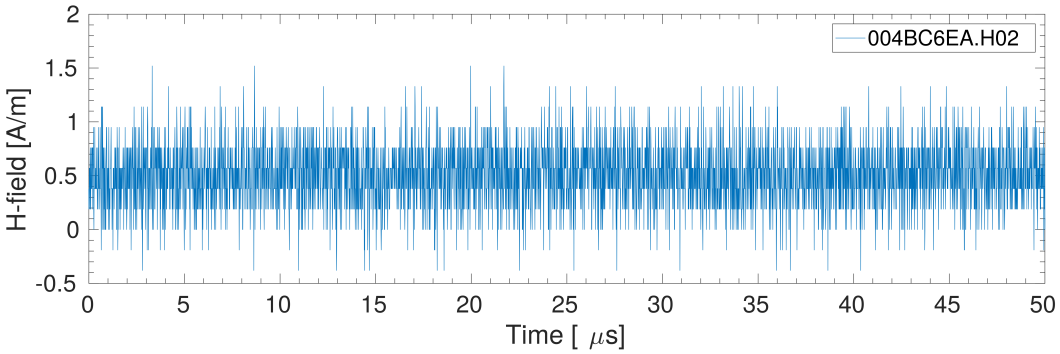

FIGURE A.2: Noise in the H-field measurements.

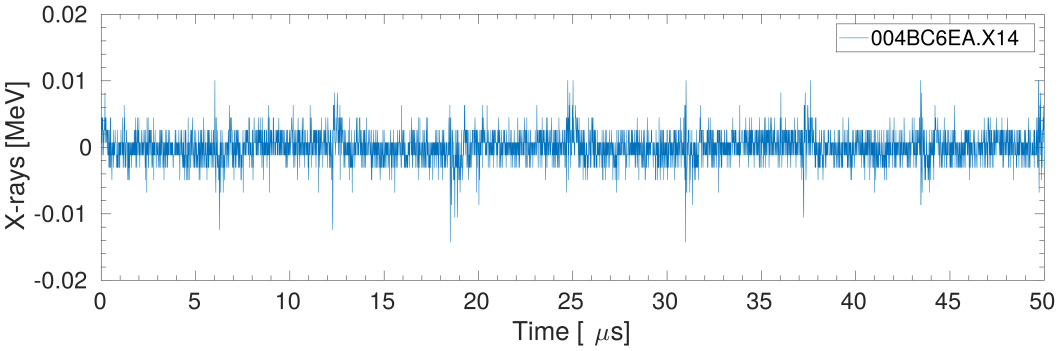

FIGURE A.3: Noise in the X14 X-ray energy measurements.

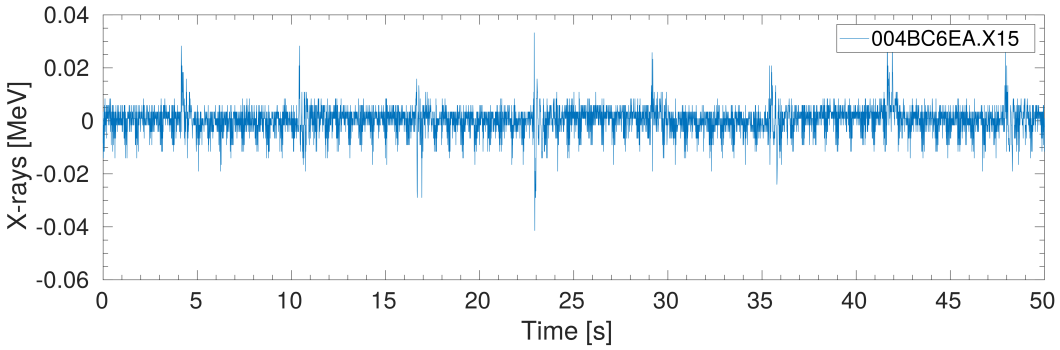

FIGURE A.4: Noise in the X14 X-ray energy measurements.

Appendix B

Categorized flashes by initiation phases

B.1 Bidirectional leaders starting with positive leaders

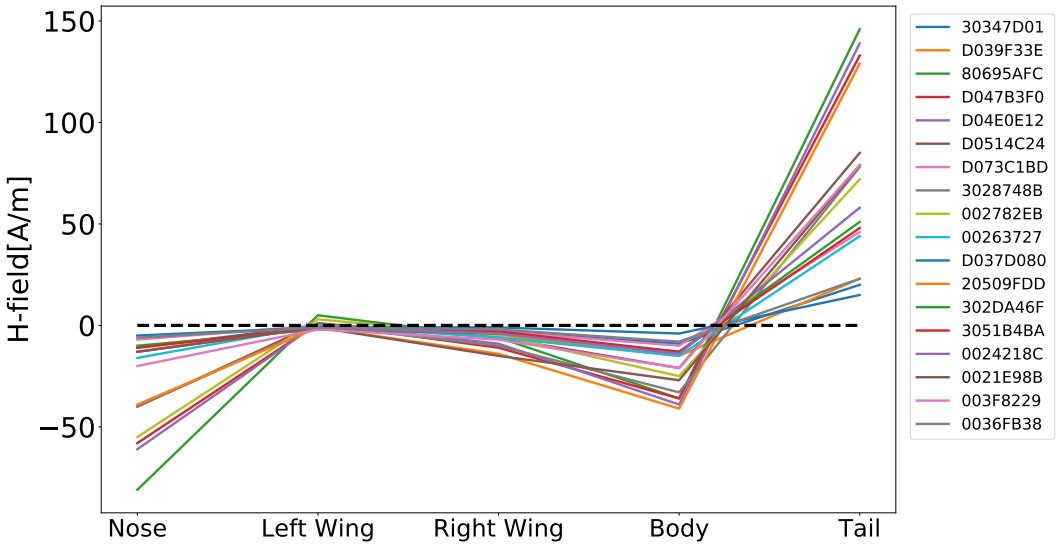

FIGURE B.1: Nose: Magnetic field measurements of the individual lightning flashes belonging to the Nose class.

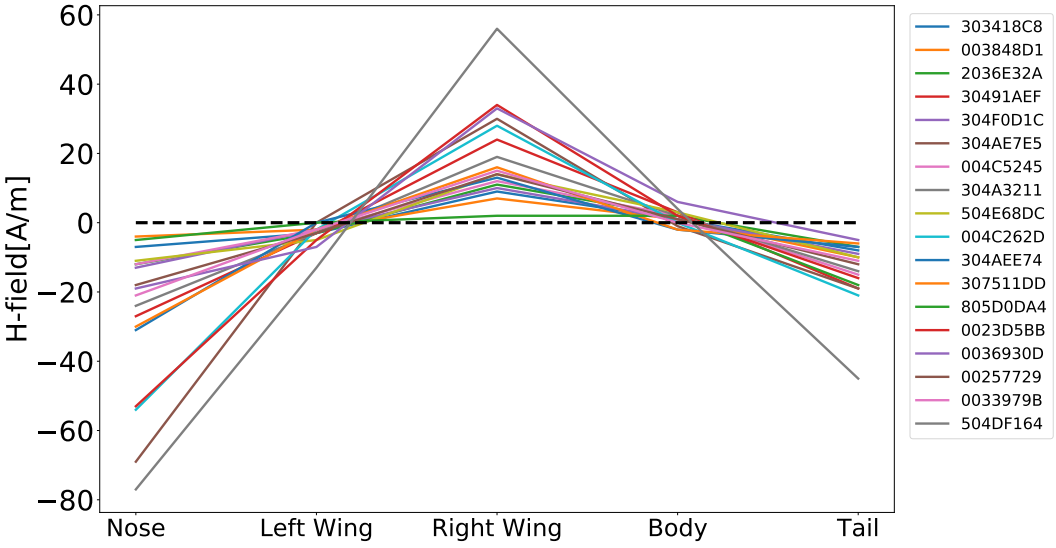

FIGURE B.2: Nose + Tail: Magnetic field measurements of the individual lightning flashes belonging to the Nose + Tail class.

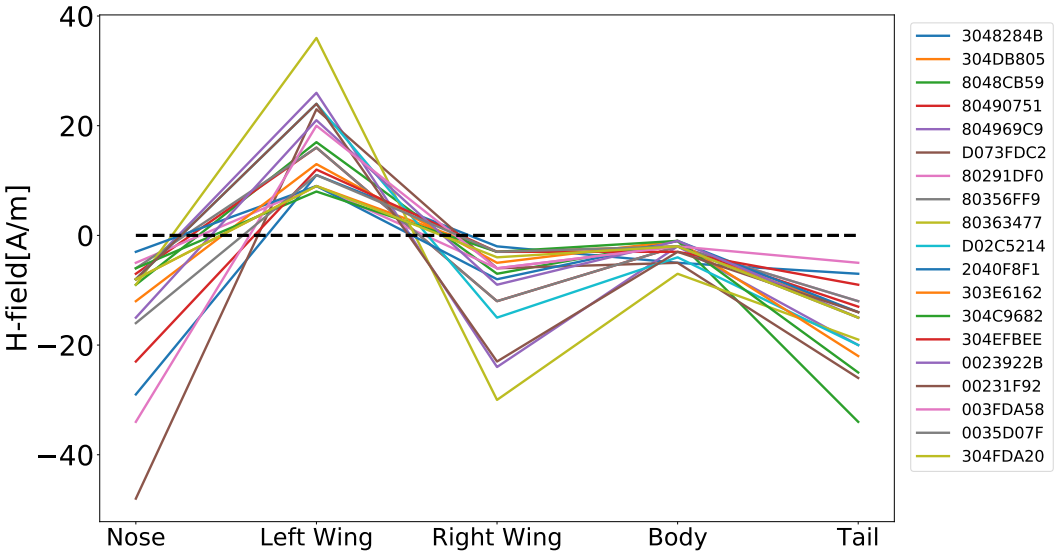

FIGURE B.3: Tail + Nose: Magnetic field measurements of the individual lightning flashes belonging to the Tail + Nose class.

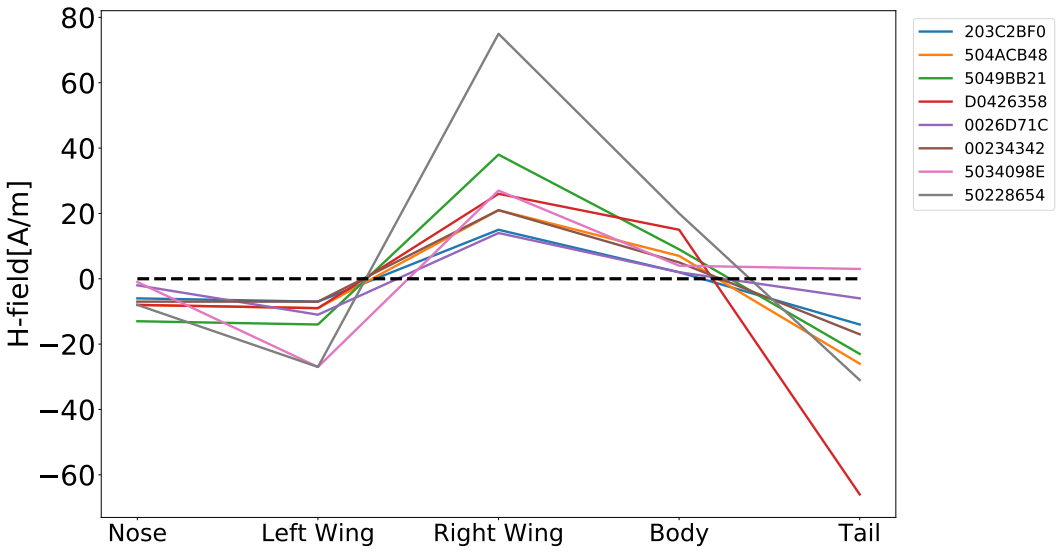

FIGURE B.4: Tail + Left Wing + Nose: Magnetic field measurements of the individual lightning flashes belonging to the Tail + Left Wing + Nose class.

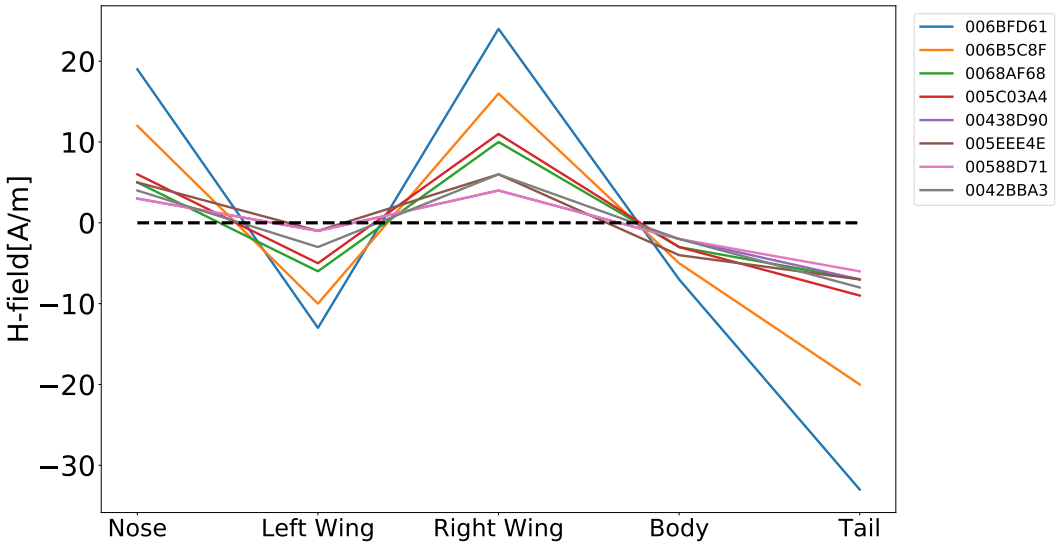

FIGURE B.5: Tail + Left Wing: Magnetic field measurements of the individual lightning flashes belonging to the Tail + Left Wing class.

FIGURE B.6: Tail + Right Wing: Magnetic field measurements of the individual lightning flashes belonging to the Tail + Right Wing class.

B.2 Bidirectiona leader initiations preceded by negative corona.

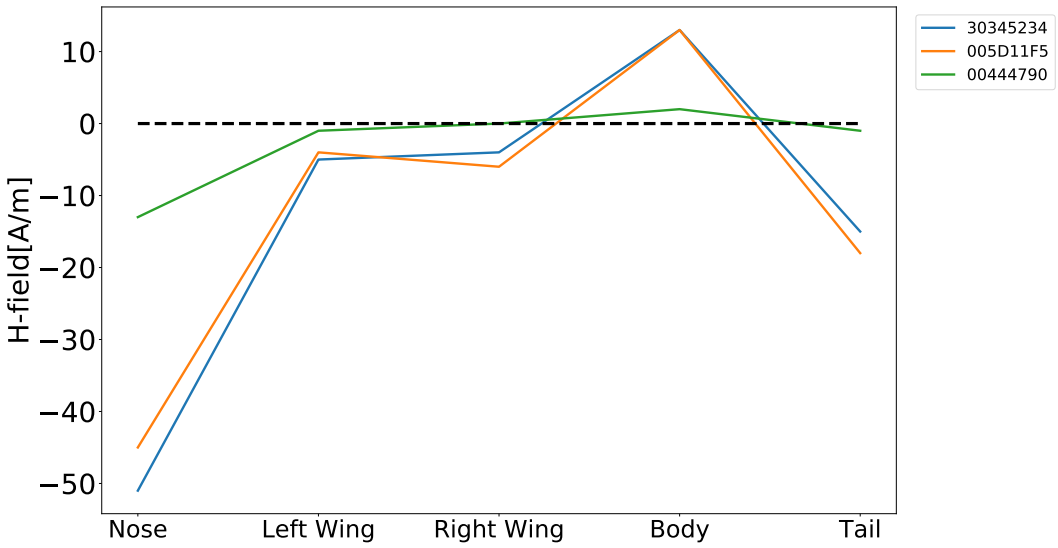

FIGURE B.7: Nose (II): Magnetic field measurements of the individual lightning flashes belonging to the Tail + Right Wing class.

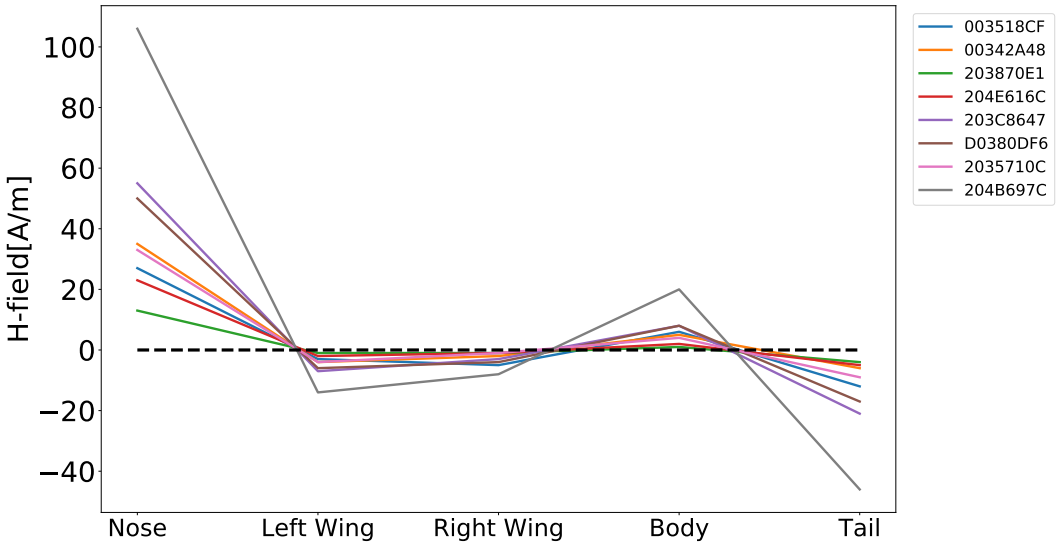

FIGURE B.8: Tail: Magnetic field measurements of the individual lightning flashes belonging to the Tail + Right Wing class.

Bibliography

BARC, Beltsville Agricultural Reaserch Center (2016). *Rime and Graupel*. URL: https://sgil.ba.ars.usda.gov/snowsite/rimegraupel/rg.html (visited on 02/23/2018).

Bazelyan, E.M. and Y.P. Raizer (2000). *Lightning Physics and Lightning Protection*. IOP Publishing. ISBN: 978-0750304771.

Beiser, A. (2004). *Concepts of Modern Physics*. McGraw Hill Higher Education. ISBN: 007115096X.

Berger, M.J. et al. (2017). *Stopping-Power and Range Tables for Electrons, Protons, and Helium Ions*. URL: https://physics.nist.gov/PhysRefData/Star/Text/ESTAR.html (visited on 05/10/2018).

Celestin, S. and V.P. Pasko (2011). "Energy and fluxes of thermal runaway electrons produced by exponential growth of streamers during the stepping of lightning leaders and in transient luminous events". In: *Journal of Geophysical Research* 116.A03315. DOI: 10.1029/2010JA016260.

Cember, H. and T.E. Johnson (2009). *Introduction to Health Physics*. McGraw-Hill. ISBN: 978-0-07-164323-8.

Cooray, V. (2014). *The Lightning Flash*. The Institution of Engineering and Technology. ISBN: 978-1-84919-691-8.

Deursen, A.P.J van et al. (2012). "In-Flight Lightning Damage Assessment System ILDAS, Tests On-ground and In-flight." In: *Proceedings of the 2012 ESA Workshop on Aerospace EMC 2012* 1, pp. 2–5.

Dwyer, J.R. (2004). "Implications of x-ray emission from lightning". In: *Geophysical Research Letters* 31.12, p. L12102. DOI: 10.1029/2004GL019795.

Dwyer, J.R. and M.A. Uman (2014). "The physics of lightning". In: *Physics Reports* 534.4, pp. 147–241. DOI: 10.1016/j.physrep.2013.09.004.

Dwyer, J.R. et al. (2004). "Measurements of x-ray emission from rocket-triggered lightning". In: *Geophysical Research Letters* 31.5, p. L05118. DOI: 10.1029/2003GL018770.

Dwyer, J.R. et al. (2005a). "X-ray bursts associated with leader steps in cloud-to-ground lightning". In: *Geophysical Research Letters* 32.1, pp. 1–4. DOI: 10.1029/2004GL021782.

Dwyer, J.R. et al. (2005b). "X-ray bursts produced by laboratory sparks in air". In: *Geophysical Research Letters* 32.20, pp. 1–4. DOI: 10.1029/2005GL024027.

Dwyer, J.R. et al. (2015). "Positron clouds within thunderstorms". In: *Journal of Plasma Physics* 81.4. DOI: 10.1017/S0022377815000549.

Fisher, F.A. et al. (1977). "Lightning protection of aircraft". In: *NASA Reference Publication* 1008.

FlightRadar24 (2015). *Flight Radar 24*. URL: https://www.flightradar24.com/.

Howard, J. et al. (2010). "RF and X-ray source locations during the lightning attachment process". In: *Journal of Geophysical Research Atmospheres* 115.6, pp. 1–25. DOI: 10.1029/2009JD012055.

Hubell, J.H. and S.M. Seltzer (2004). *X-Ray Mass Attenuation Coefficients (Database)*. URL: https://www.nist.gov/pml/x-ray-mass-attenuation-coefficients (visited on 05/09/2018).

IUPAC (1997). *Compendium of Chemical Terminology, 2nd ed.* ISBN: 0-86542-684-8.

Jayaratne, E.R. (1998). "Possible laboratory evidence for multipole electric charge structures in thunderstorms". In: *Journal of Geophysical Research* 103.D2, pp. 1871–1878. DOI: 10.1029/97JD02553.

Jayaratne, E.R. and C.P.R. Saunders (1983). "Charge on ice crystals in laboratory clouds". In: *Journal of Geophysical Research* 88.C9, pp. 5494–5496. DOI: 10.1029/JC088iC09p05494.

Kasemir, H. W (1983). *Heinz-Wolfram Kasemir: His Collected Works*. American Geophysical Union. ISBN: 9780875907376. DOI: 10.1002/9781118704813.ch29.

Kasemir, H.W. (1960). "A Contribution to the Electrostatic Theory of a Lightning Discharge". In: *Journal of Geophysical Research* 65.7, pp. 1873–1878.

Kelly, N.A. (2014). "Long Duration Gamma-Ray Emission From Thunderclouds". In: *PhD thesis*.

Kelly, N.A. et al. (2015). "Relativistic electron avalanches as a thunderstorm discharge competing with lightning." In: *Nature Communications* 6.7845, pp. 1–7. DOI: 10.1038/ncomms8845.

Kochkin, P. et al. (2016). "Pilot system development in metre-scale laboratory discharge". In: *Journal of Physics D: Applied Physics* 49.42. DOI: 10.1088/0022-3727/49/42/425203.

Kochkin, P. et al. (2017). "In-flight Observation of Gamma Ray Glows by ILDAS". In: *Journal of Geophysical Research: Atmospheres* 122.23, pp. 12801–12811. DOI: 10.1002/2017JD027405.

Kochkin, P. et al. (Under review). "In-fligh observation of positron annihilation by ILDAS". In:

Kochkin, Pavlo et al. (2015a). "In-flight measurements of energetic radiation from lightning and thunderclouds". In: *Journal of Physics D: Applied Physics* 48.42. DOI: 10.1088/0022-3727/48/42/425202.

Kochkin, P.O. et al. (2012). "Experimental study of hard X-rays emitted from metre-scale positive discharges in air". In: *Journal of Physics D: Applied Physics* 45.45. DOI: 10.1088/0022-3727/45/42/425202.

Kochkin, P.O. et al. (2015b). "Experimental study on hard X-rays emitted from metre-scale negative discharges in air". In: *Journal of Physics D: Applied Physics* 48.2. DOI: 10.1088/0022-3727/48/2/025205.

Loeb, L.B. and J.M. Meek (1940). *The mechanism of the electric spark*. Stanford University Press.

Loeb, Leonard B. (1966). "The Mechanisms of Stepped and Dart Leaders in Cloud-to-Ground Lightning Strokes". In: *Journal of Geophysical Research* 71.20.

MacGorman, D.R. and W.D. Rust (1998). *The electrical nature of storms Donald R. MacGorman, W. David Rust*. Oxford University Press. ISBN: 0195073371.

Mazur, V. (1989). "A physical model of lightning initiation on aircraft in thunderstorms". In: *Journal of Geophysical Research* 94.D3, pp. 33261–3340. DOI: 10.1029/JD094iD03p03326.

McCarthry, M. and G.K. Parks (1985). "Further observations of x-rays inside thunderstorms". In: *Geophysical Reasearch Letters* 12.6, pp. 393–396.

Meek, J.M. (1940). "A Theory of Spark Discharge". In: *Physical Review* 57.8, pp. 722–728. DOI: 10.1103/PhysRev.57.722.

Montanyà, J. et al. (2014). "Observation and properties of a sub-cloud bidirectional leader". In: *International Conference on Atmospheric Electricity*.

Moore, C.B. et al. (2001). "Energetic radiation associated with lightning stepped-leaders". In: *Geophysical Research Letters* 28.11, pp. 2141–2144. DOI: 10.1029/2001GL013140.

Morgan, D. et al. (2012). "The Interaction of Lightning with Aircraft and the Challenges of Lightning Testing". In: *Journal Aerospace Lab* 5, pp. 1–10.

Moss, G.D. et al. (2006). "Monte Carlo model for analysis of thermal runaway electrons in streamer tips in transient luminous events and streamer zones of lightning leaders". In: *Journal of Geophysical Research* 111.2, pp. 1–37. DOI: 10.1029/2005JA011350.

NLR, The National Aerospace Laboratory (2009). *Lightning in the hangar*. URL: http://www.nlr.org/news/lightning-in-the-hangar/ (visited on 04/30/2018).

NPTEL (2009). *Development of Electron Avalanche*. URL: http://nptel.ac.in/courses/108104048/lecture5/slide1.htm (visited on 04/23/2018).

Parks, G.K. et al. (1981). "X-ray enhancements detected during thunderstorm and lightnin activites". In: *Geophysical Reasearch Letters* 8.11, pp. 1176–1179.

Rakov, V.A. and M.A. Uman (2003). *Lightning: Physics and Effects*. Cambridge University Press. ISBN: 9781107266834.

Thorsteinsen, T.F. (1995). *Strålingsfysikk*.

UCL-Lecture-Notes (2009). *Topic 8 - Cosmic Ray Experiments, the Cerenkov Effect*. URL: http://zuserver2.star.ucl.ac.uk/~idh/PHAS2112/Lectures/2009/Nuclear/topic8.html (visited on 04/24/2018).

Uman, M. A. and V. A. Rakov (2003). "The interaction of lightning with airborne vehicles". In: *Progress in Aerospace Sciences* 1, pp. 61–81. DOI: 10.1016/S0376-0421(02)00051-9.

Wilson, C.T.R. (1924). "The electric field of a thundercloud and some of its effects". In: *Proc. Phys. Soc. London.* 32D.37.

Zwemmer, R. et al. (2009). "In-Flight Lightning Damage Assessment System (ILDAS) Results of the Concept Prototype tests". In: *ICOLSE 2009* September, pp. 15–17.

Østgaard, N. et al. (2016). "Relativistic electrons fromsparks in the laboratory N." In: *Journal of Geophysical Research* 121.6, pp. 2939–2954. DOI: 10.1002/2015JD024394.